

# ANALYSIS OF CATALYTIC GROWTH OF CARBON NANOTUBES

THÈSE N° 2787 (2003)

PRÉSENTÉE À LA FACULTÉ SCIENCES DE BASE

Institut de physique des nanostructures

SECTION DE PHYSIQUE

ÉCOLE POLYTECHNIQUE FÉDÉRALE DE LAUSANNE

POUR L'OBTENTION DU GRADE DE DOCTEUR ÈS SCIENCES

PAR

**Christian KLINKE**

Diplom-Physiker, Universität Fridericana, Karlsruhe, Allemagne  
et de nationalité allemande

acceptée sur proposition du jury:

Prof. K. Kern, directeur de thèse

Dr J.-M. Bonard, rapporteur

Prof. J. Chevrier, rapporteur

Prof. L. Forro, rapporteur

Lausanne, EPFL  
2003



# Abstract

This thesis covers the analysis of the catalytic growth of carbon nanotubes under well-defined conditions, the optimization of the field emission properties of those structures and introduces a model for the growth mechanism based on the experimental results. Experimental investigations are presented which allow to get a comprehensive picture of the catalytic growth of carbon nanotube films. These films were generated by patterning silicon surfaces with transition metal catalysts using microcontact printing and subsequent generation of nanotubes by means of chemical vapor deposition (CVD). The development of the used catalyst was characterized as function of growth time and applied temperature. The subsequent studies of the morphology of the carbon structures grown by CVD revealed a significant influence of the deposition temperature and the catalyst material on the quality of the carbon structures. Electron microscopy and Raman spectroscopy were used to investigate the character of these structures in more detail. It was found that the increase in temperature above 800°C resulted in the formation of a polycrystalline outer shell over a nanotube core.

Based on those experimental results a mechanism for the growth of carbon nanotubes is suggested. Acetylene is dissociated catalytically on the catalyst nanoparticles spread on the substrate surface. In a first stage the acetylene reduces the metal oxide grains to pure metal. The further catalytic dissociation of acetylene takes presumably place at facets of well-defined crystallographic orientation and the carbon diffuses into the particle. The resulting density gradient of carbon dissolved in the particle drives the diffusion of carbon through the particle. In order to avoid dangling bonds, the carbon atoms assemble at a less reactive facet of the particle, which leads to the formation of a nanotube. Thicker nanotubes at higher temperatures are generated due to the dissociation of acetylene in the gas phase, which leads to the formation of carbon flakes that condense on the catalytically grown structures. In order to support the growth model, simple classic calculations and simulations were performed, which yielded formulas that allow to estimate nanotube growth properties, like the growth velocity. The theoretical results correspond well with the experimental. Furthermore a mechanism for the cessation of the nanotube growth was proposed.

Complementary, the field emission properties of different carbon structures were determined. It turned out that the thinnest nanotubes emit at lowest fields. Furthermore, in regard to applications nanotubes have been grown on glass substrates and the field emission properties of such samples have been characterized. Finally, a scanning probe microscope is presented which exploits the field emission of carbon nanotubes. It would offer new possibilities to characterize samples on a nanometer scale.



# Zusammenfassung

Diese Doktorarbeit beschäftigt sich mit dem katalytischen Wachstum von Kohlenstoff-Nanotubes unter wohl-definierten Bedingungen, der Optimierung der Feldemissionseigenschaften dieser Strukturen und sie stellt ein Modell für den Wachstumsmechanismus vor, das auf den experimentellen Resultaten aufbaut. Es werden experimentelle Untersuchungen vorgestellt, die einen umfassenden Eindruck des katalytischen Wachstums von Kohlenstoff-Nanotube-Filmen vermitteln. Diese Filme wurden erzeugt, indem Siliziumoberflächen durch Microcontact Printing mit Übergangsmetallkatalysatoren bestempelt und anschließend mittels Chemical Vapor Deposition (CVD) Nanotubes erzeugt wurden. Die Entwicklung der benutzten Katalysator wurde als Funktion der Wachstumszeit und der Temperatur untersucht. In folgenden Untersuchungen der Morphologie der Strukturen, die mittels CVD gewachsen wurden, wurde ein erheblicher Einfluss der Abscheidungstemperatur und des Katalysatormaterials auf der Qualität der Kohlenstoffstrukturen gefunden. Elektronenmikroskopie und Ramanspektroskopie wurden verwendet um den Charakter dieser Strukturen ausführlicher zu erforschen. Dabei stellte sich heraus, dass die Zunahme der Temperatur über 800°C die Erzeugung einer polykristallinen Schale über einem Nanotube-Kern zur Folge hat.

Aufbauend auf diesen experimentellen Resultaten konnte ein Model für das Wachstum der Nanotubes vorgeschlagen werden. Azetylen wird katalytisch auf den Katalysator-Nanopartikeln, die sich auf der Substratoberfläche verteilen, zersetzt. In einem ersten Schritt reduziert das Azetylen die Metalloxid-Teilchen zu reinem Metall. Die weitere katalytische Zersetzung des Azetylens findet vermutlich an den kristallographischen Facetten statt und der Kohlenstoff diffundiert in das Partikel. Der resultierende Konzentrationsgradient des im Partikel gelösten Kohlenstoffs treibt die Diffusion des Kohlenstoffs durch das Partikel an. Um "dangling bonds" zu vermeiden, konstruieren die Kohlenstoff-Atome an einer weniger reaktiven Facette des Partikels das Nanotube. Die dickeren Strukturen, die sich bei höheren Temperaturen bilden, kommen durch die thermische Zersetzung des Azetylens in der Gasphase zustande. Der gasförmige Kohlenstoff bildet Flocken, die sich anschließend auf den katalytisch gewachsenen Strukturen niederschlagen. Um das Model zu unterstützen wurden einfache, klassische Berechnungen und Simulationen durchgeführt. Dadurch konnten einige Formeln gewonnen werden, die z. B. die Nanotube-Wachstumsgeschwindigkeit abschätzen lassen. Außerdem wurde eine Mechanismus für das Stoppen des Nanotube-Wachstums vorgeschlagen.

Ergänzend wurden die Feldemissionseigenschaften der verschiedenen Kohlenstoff-Strukturen untersucht. Die dünnsten Nanotubes emittierten dabei bei den geringsten Feldstärken. Im Hinblick auf Anwendungen wurden außerdem Nanotubes auf Glassubstraten

gewachsen und deren Feldemissioneigenschaften vermessen. Schließlich wird ein Raster-Mikroskop vorgestellt, das die Feldemission von Kohlenstoff-Nanotubes ausnutzt. Dieses Mikroskop würde neue Möglichkeiten zur Charakterisierung von Proben auf Nanometer-Skala bieten.

# Contents

<b>Title page</b>	<b>i</b>
<b>Abstract</b>	<b>iii</b>
<b>Zusammenfassung</b>	<b>v</b>
<b>Table of contents</b>	<b>viii</b>
<b>1 Introduction</b>	<b>1</b>
<b>2 Basics</b>	<b>5</b>
2.1 Carbon nanotubes . . . . .	5
2.2 Microcontact printing . . . . .	8
2.3 Chemical vapor deposition . . . . .	10
2.4 Field emission . . . . .	11
2.5 Raman spectroscopy . . . . .	13
2.6 Spectrophotometry . . . . .	14
2.7 Electron microscopy . . . . .	16
2.7.1 Transmission Electron Microscope . . . . .	16
2.7.2 Scanning Electron Microscope . . . . .	18
<b>3 Catalytic growth of carbon nanotubes films</b>	<b>19</b>
3.1 Synthesis of nano-structured material . . . . .	20
3.2 Characterization of the ink . . . . .	20
3.2.1 Evolution of the catalyst in solution . . . . .	20
3.2.2 Evolution of the catalyst particles during annealing . . . . .	22
3.3 Morphology . . . . .	26
3.3.1 Printing homogeneity . . . . .	26
3.3.2 Influence of the used catalyst . . . . .	26
3.3.3 Deposition temperature . . . . .	27
3.3.4 Catalyst concentration . . . . .	28
3.3.5 Structure of the nanotubes . . . . .	29
3.3.6 Deposition time . . . . .	31
3.3.7 Effect of the pattern . . . . .	31
3.4 Raman spectroscopy . . . . .	33

3.5	Nanotube growth on glass . . . . .	35
3.6	Ferritin as catalyst for the nanotube growth . . . . .	37
<b>4</b>	<b>Growth mechanism</b>	<b>41</b>
4.1	Supposed growth mechanism . . . . .	41
4.2	Calculations and simulations for the growth mechanism . . . . .	43
4.2.1	Calculations . . . . .	44
4.2.2	Simulations . . . . .	53
4.3	Discussion . . . . .	57
<b>5</b>	<b>Field emission of carbon nanotube films</b>	<b>61</b>
5.1	Field emission of nanotube films obtained at different deposition temperatures	61
5.2	Field emission of nanotubes on glass substrate . . . . .	63
5.3	Simulations for the field emission of carbon nanotubes . . . . .	63
5.3.1	Effect of the geometry on the field emission . . . . .	64
5.3.2	Heating of nanotubes during field emission . . . . .	69
5.3.3	Nanotubes as field emitter tips in a scanning probe microscope . . . . .	72
5.4	Discussion . . . . .	75
<b>6</b>	<b>Conclusions and perspectives</b>	<b>77</b>
	<b>Bibliography</b>	<b>81</b>
	<b>List of Publications</b>	<b>89</b>
	<b>Curriculum Vitae</b>	<b>91</b>
	<b>Acknowledgements</b>	<b>93</b>



Wie nur dem Kopf nicht alle Hoffnung schwindet,  
Der immerfort an schalem Zeuge klebt,  
Mit gier'ger Hand nach Schätzen gräbt,  
Und froh ist wenn er Regenwürmer findet!

*J. W. von Goethe, Faust I.*

# Chapter 1

## Introduction

Carbon nanostructures like fullerenes [1], nanotubes [2], nano-onions [3] and nano-horns [4] have attracted much interest recently. In particular the mechanical and electronic properties of carbon nanotubes are the subject of intensive studies [5,6]. Beside the fundamental interest in their physical and chemical properties, there are already some applications based on nanotubes. For example, they are capable to work as efficient field emitters [7] and can form a basis for very robust fibers [8]. Nanotubes can be produced by arc discharge [2], by laser-ablation [9] or by chemical vapor deposition techniques (CVD) [10]. CVD is currently the most promising and flexible method with regard to applications, but our understanding of the influence of the catalyst and the deposition parameters on the nanotube growth is still fragmentary.

### What are carbon nanotubes?

Very small diameter (less than 10 nm) carbon filaments were prepared in the 1970's and the 1980's through the synthesis of vapor grown carbon fibers by the decomposition of hydrocarbons at high temperatures in the presence of transition metal catalyst particles of <10 nm diameter [11]. However, no detailed systematic studies of such very thin filaments were reported in these early years, and it was not until the observation of carbon nanotubes in 1991 by Iijima of the NEC Laboratory in Japan using High-Resolution Transmission Electron Microscopy (HRTEM) that the carbon nanotube field was seriously launched [2]. The structures found by Iijima were *multi-wall nanotubes* (MWNT). These tubular structures consist of several concentric graphitic layers. Two years later Iijima et al. (NEC Laboratory) [12]

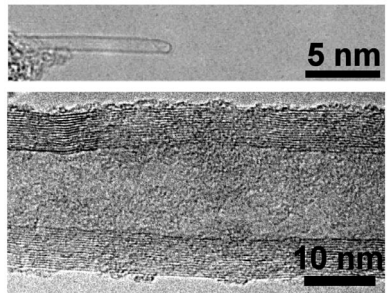


Figure 1.1: TEM image of a single-wall and a multi-wall carbon nanotube.

and Bethune et al. (IBM Almaden Laboratory) [13] discovered also the *single-wall nano-*

tubes (SWNT) which consist just of one single graphitic layer (Fig. 1.1).

Carbon nanotubes possess extraordinary electric and mechanical properties. Single-wall nanotube can be metallic or semi-conducting depending on the chirality of the tubular arranged graphitic layer and the diameter of the nanotube [14]. Multi-wall carbon nanotubes are more complex objects than single-wall nanotubes. Each of the carbon shells of the MWNTs can have different electronic character and chirality. However, in studies on MWNTs with a metallic outer shell that are side-bonded to metal electrodes, it was concluded that electrical transport at low energies is dominated by outer-shell conduction. These systems show 1D or 2D characteristics, depending on their diameter and the nature of the property examined [15]. One example may demonstrate the interesting mechanical properties: The Young's modulus of multi-wall nanotubes is about 1 TPa and lies thus between the one of ceramics and the one for diamond [5]. Carbon nanotubes are about 100 times stronger than steel per unit weight. This makes them good candidates for new kinds of ropes and other new, strong and very light materials. Furthermore they possess a high chemical stability due to their graphitic layers with its' saturated bondings. But the stability decreases with larger curvatures due to the bending stress and, correspondingly, the chemical reactivity increases with thinner nanotubes.

### **What can we do with carbon nanotubes?**

Due to their extraordinary properties they provide a wide spectrum of applications in the technical field as well as in basic research. Examples are field emission flat panel displays [16], field emission lamps [17], new carbon fibers [8], conventional field-effect transistors [18], one-electron transistors [19], gas detectors [20], field emission guns for electron microscopes [21], x-ray sources [22, 23]. Thus carbon nanotubes will soon be found in commercial devices.

### **How to create them?**

There are several ways to synthesize nanotubes: e.g. by arc-discharge [24], laser ablation [25], or catalytic CVD [26]. The catalytic growth in combination with the chemical vapor deposition is the most simple way to generate a relatively large amount of nanotubes. By the CVD method aligned and ordered nanotube structures can be grown in a controlled process on surfaces [27, 28]. This is not possible with the two other methods. But laser ablation and arc-discharge can deliver nanotubes of better quality.

### **What is the aim of this work?**

This work should contribute to the elucidation of the growth mechanism of carbon nanotubes and propose optimized growth conditions in regard to applications using the catalytic method. To this end experimental results should be gained, interpreted and compared with theoretical approaches. The attained insights should support basic research and help to develop new and better devices and applications.

**What are the results?**

In Chapter 2 the general basics of nanotubes are described: Their geometry, electronic and mechanical properties and their synthesis by CVD and microcontact printing. Furthermore the basics of the used characterization methods are presented, as there are the measurement of the field emission, Raman spectroscopy, spectrophotometry and electron microscopy.

In Chapter 3 are studied the aging of the used catalyst solution, the development of the catalyst during annealing, the growth conditions and their effect on the nanotube morphology. The crystallinity of the nanotubes was studied by transmission electron microscopy and Raman spectroscopy.

The results lead to a growth model which is described in Chapter 4. The model is supported by calculations and simulations with the finite element method. This leads again to some formulas which can predict several aspects of the growth such as the growth velocity. Those results are then compared with experimental data.

In regard to applications in industry the field emission of the obtained structures and other nanotube films was measured, characterized and simulated in Chapter 5.

Finally in Chapter 6 the results and discussions are summarized and perspectives for the future are pointed out.



# Chapter 2

## Basics

There are two types of carbon nanotubes: They can consist of one (single-wall) or more (multi-wall) graphitic layers. The single-wall nanotubes are available in different geometric configurations (chirality and diameter) which determine their electronic character. The multi-wall nanotubes considered in this work show usually metallic character. They are produced in a catalytic process. The catalyst has been delivered to silicon samples by microcontact printing, an easy-to-apply lithography method. Subsequently the samples have been transferred to an oven for chemical vapor deposition (CVD) to grow the nanotubes. After the deposition the obtained structures have been characterized by their Raman spectrum and their field emission properties. In this chapter the basic properties of carbon nanotubes and fundamentals of the used methods are presented.

### 2.1 Carbon nanotubes

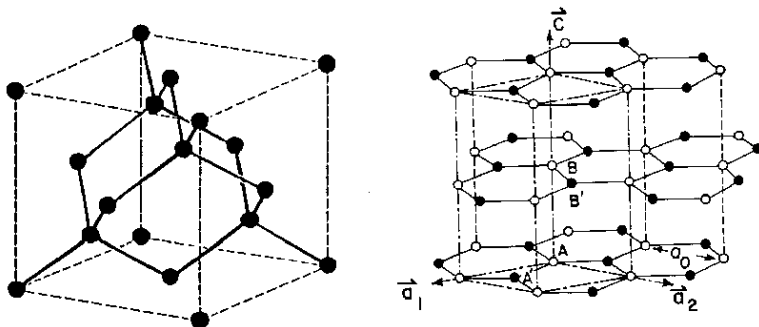
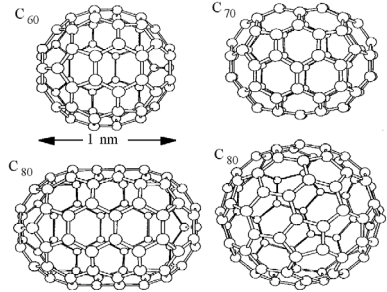


Figure 2.1: *Structure of the two main modifications of carbon: Diamond and graphite.*

Carbon exists in the solid form mainly in two different modifications (Fig. 2.1). First, as

transparent *diamond* if the orbitals of the carbon atoms are in a state of  $sp^3$  hybridisation. The lattice is formed by carbon atoms with four bonds. This configuration is very rigid, stable and hard. The solid has a band gap of 5.5 eV and is thus an insulator. The second modification is the black *graphite* with  $sp^2$  hybridized orbitals. They form the plane hexagonal structure of the graphite layers. The bonding strength in the plane is very strong whereas between the layers the bonding is just mediated by relatively weak van-der-Waals forces. In the plane graphite is a good electric conductor.

In 1985 Kroto et al. discovered a new kind of carbon, the so called *fullerenes* [1]. These are ball-like molecules which consist of e.g. 60 carbon atoms. Later, similar configurations with a different number of atoms were discovered (Fig. 2.2). For the discovery of the fullerenes Kroto, Smalley and Curl obtained the Nobel Prize for Chemistry in 1996.



In figure 2.3 one can see a graphene plane with the lattice vectors  $O$  and  $b$ . A single-wall nanotube is in principle a rolled-up graphene plane. If the plane is rolled-up perpendicular to the tube axis the line revolving the tube has a *armchair*-like shape. Under an angle of  $30^\circ$  the shape is *zig-zag*-like. The tubes with an angle in between are called *chiral* (Fig. 2.4).

Figure 2.2: A new type of carbon: Spherical fullerene molecules.

Any single-wall nanotube configuration can be generated by superimposing the hexagon at the original point  $O$  to a hexagon indicated by  $(a, b)$  defined by a chiral vector  $\vec{R} = a\vec{x} + b\vec{y}$ , where  $\vec{x}$  and  $\vec{y}$  are the primitive vectors whose length are both equal to  $\sqrt{3}d_{C-C}$  with  $d_{C-C}$  indicating the C-C bond length [14]. One can derive by geometrical considerations that the diameter  $D$  of the tube  $(a, b)$  and the conformation angle  $\theta$  with equal  $d_{C-C}$  are given by

$$D = \frac{\sqrt{3}d_{C-C}}{\pi} \sqrt{a^2 + ab + b^2} \quad (2.1)$$

$$\theta = \arccos\left(\frac{2a + b}{2\sqrt{a^2 + ab + b^2}}\right) \quad (0 \leq \theta \leq \frac{\pi}{6}) \quad (2.2)$$

Using simple tight-binding methods, one shows that single-wall carbon nanotubes with  $2a + b = 3N$  are metallic (whereas  $N$  is a positive integer) and with  $2a + b \neq 3N$  they are semiconductive.

Actually, it is a little bit more complicated. Without going into the details which can be looked up in [14] one can say that the armchair tubes  $(a, a)$  are metallic, zigzag tubes  $(3a, 0)$  are narrow-gap semiconductors, helical tubes  $(a, b)$  with  $2a + b = 3N$  are also narrow-gap semiconductors and all other tubes are wide-gap semiconductors. This behavior is due to periodic boundary conditions for the component of momentum along the circumference of the tube which results in quantization.

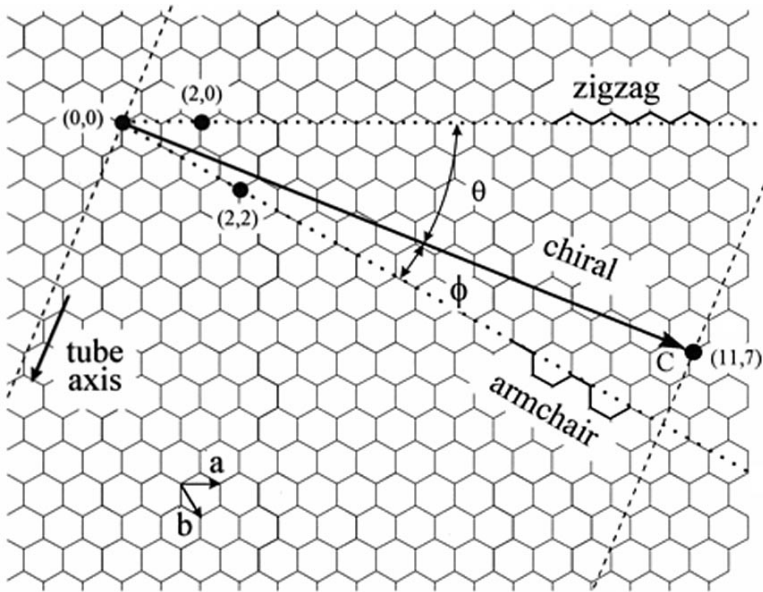


Figure 2.3: Grid of a graphene sheet with the lattice vector  $a$  and  $b$  and the angles  $\theta$  and  $\phi$  which determine the type of the nanotube: armchair, zig-zag, chiral.

For armchair  $(n,n)$  tubes, the lowest one-dimensional sub-band results in only one pair of one-dimensional gap-less modes of propagation parallel to the tube axis. As a result, armchair nanotubes are predicted to be prototype one-dimensional quantum wires that will exhibit metallic conduction. Armchair CNTs possess a good electrical conductivity like metals (independent of diameter).

Multi-wall nanotubes consist of several concentric graphite layers (Fig. 2.4). The distance between two layers in MWNTs is 0.347 nm. The outer diameter of MWNTs can range from 5 to 50 nm whereas SWNTs have typically a diameter between 1 and 2 nm. The good electrical conductivity, the chemical stability, the high stiffness, the huge length-diameter ratio, lengths up to 100  $\mu\text{m}$  and the very small curvature radius at the tip make MWNTs suitable for field emitters.

The interesting electronic properties of carbon nanotubes are used e.g. for nanotube field-effect transistors [18] or together with their extreme length-diameter ratio in field emission devices [29]. The tiny curvature radius makes them good candidates for new tips in scanning probe microscopes, since e.g. with thinner tips one can obtain a better resolution in AFM measurements [30].

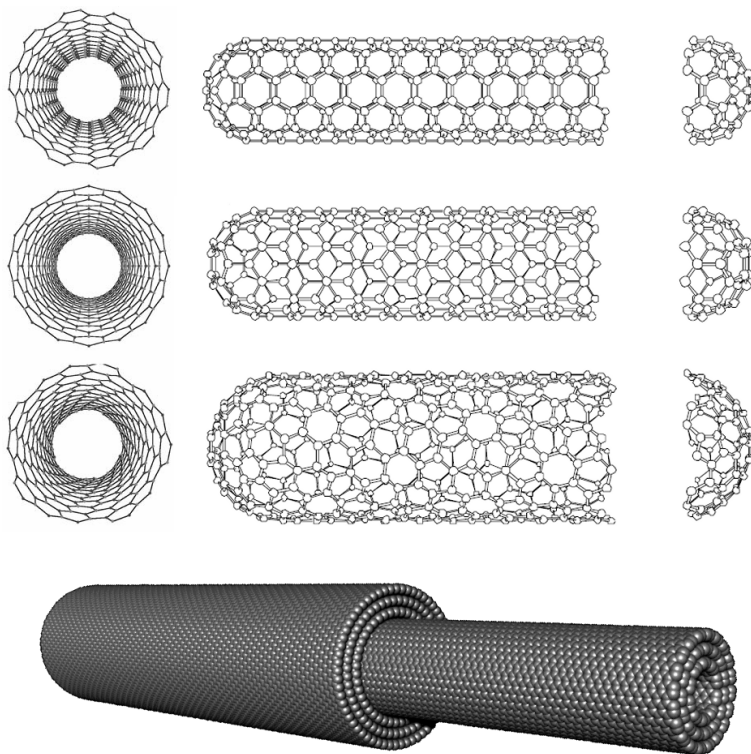


Figure 2.4: *Models of carbon nanotubes: single-wall nanotubes with armchair, zig-zag and chiral configuration and a multi-wall nanotube.*

## 2.2 Microcontact printing

Microcontact printing ( $\mu\text{CP}$ ) is one of the soft lithography techniques which have in common that they all use a patterned elastomer as the mask, stamp, or mold [31]. Further members of this family of techniques are replica molding (REM), microtransfer molding ( $\mu\text{TM}$ ), micromolding in capillarities (MIMIC), and solvent-assisted micromolding (SAMIM). The strength in soft lithography is in replicating rather than fabricating the master, but rapid prototyping and the ability to deform the elastomeric stamp or mold give it a unique capability even in fabricating master patterns. Soft lithography techniques require remarkably little capital investment and are procedurally simple: They can often be carried out in ambient laboratory environment. Additionally, they can offer



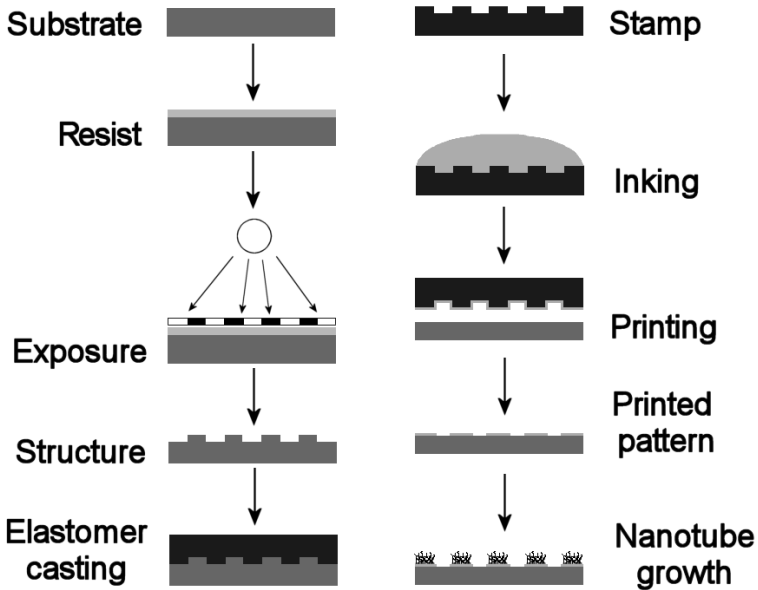


Figure 2.5: *The lithography method microcontact printing: Manufacturing of the template waver (master), casting of the polymer stamp, inking, printing and CVD procedure.*

access to new types of surfaces, optical structures, sensors, prototype devices, and systems that could be difficult to fabricate by photolithography. I.e. they possess the ability to form patterns and structures of a wide variety of materials with features that ranges from nanometers to micrometers in size.

Microcontact printing is a flexible and efficient method for pattern transfer which is remarkably simple. The conformal contact between a stamp (which consists of an elastomer) and the surface of the substrate is the key to its success. Printing has the advantage of simplicity and convenience: Once the stamp is available, multiple copies of the pattern can be produced. Printing also has the potential to be used for patterning large areas ( $>1 \text{ cm}^2$ ) with a wide range of feature size (from  $<100 \text{ nm}$  to  $>1 \text{ }\mu\text{m}$ ).

In the frame of this work a patterned silicon waver which is manufactured by contact photolithography acts as template for microcontact printing (Fig. 2.5). In order to reproduce a polymer-copy of this pattern (the stamp) the wafer is covered by a liquid polymer-catalyst mixture (here: poly(dimethyl)siloxane, PDMS) which is cured at about  $70^\circ\text{C}$  in an oven for some hours until the polymer solidifies. After that the two phases, polymer and master, can be separated. As result the polymer is then patterned with the inverse

structure of the master. In the following this polymer stamp is exposed to an oxygen plasma (1 min, 0.8 Torr, 75 W) to render the stamp hydrophilic. The stamps can then be stored in water or used immediately. In order to perform the microcontact printing a drop of e.g. a metal salt solution (ink) is deposited on the stamp and afterwards dried in a nitrogen stream. The dry stamp is then covered by a thin layer of the dried ink solution. This layer can be transferred to a flat surface just by bringing the stamp in close, conformal contact with the substrate. After subsequent lifting of the stamp a part of the dried ink remains patterned on the surface of the substrate.

Microcontact printing is a widely used technique. Due to its simplicity this parallel process is used in biology, chemistry and physics [32, 33, 34].

## 2.3 Chemical vapor deposition

In the chemical vapor deposition process (CVD) chemical reactions take place which transform gaseous molecules, called precursor, into a solid material on the surface of the substrate. CVD is a very versatile process used in the production of coatings, powders, fibers and monolithic parts. With CVD, it is possible to produce almost any metallic or non-metallic element, including carbon and silicon, as well as compounds such as carbides, nitrides, borides, oxides, intermetallics and many others.

Various configurations have been employed for chemical vapor deposition: Horizontal or vertical tube reactors, showerhead reactors or reactors with plasma enhancement. Horizontal and vertical tube furnaces are widely used in semiconductor processing due to their simplicity and productivity. They consist in principle of a heated tube with a gas in- and outlet. The gas pressure in the tube can thereby vary between some fractions of a millibar and some bar. Showerhead reactors employ a perforated or porous planar surface to dispense reactant gases more-or-less uniformly over a second parallel planar surface on which the samples are installed. The samples can be heated separately from the gas dispense and chamber wall, so showerhead reactors are generally cold-wall: only the surface holding the substrate need be at the process temperature. Inside the reactor with plasma enhancement (PECVD), a radio-frequency (RF) source excites electrons in an electromagnetic field set up between the top electrode and grounded substrate. The excited electrons collide with gas molecules to form ions, reactive neutrals or plasma. The used frequencies usually lies between some kHz and some MHz. An advantage of PECVD is the ability to deposit at much lower temperatures and pressures than would be required for thermal CVD. But a disadvantage is usually an higher disorder in the created structures and a lack of uniformity over larger surface areas. Each of the designs employs different methods for performing the fundamental operations common to all CVD reactors: dispensing gases, controlling temperature, introducing a plasma if desired, and removing byproducts. Using different catalysts, gases, temperatures or gas pressure CVD processes can generate a vast variety of structures.

In the frame of this work a catalytic growth of carbon structures was performed by CVD of hydrocarbons (acetylene). Transition metals (Fe, Ni, Co) patterned on a flat substrate (Si/SiO<sub>2</sub>, glass) were used as catalyst. The decomposition of the gas and the nanotube

growth are activated by the catalyst. During the CVD procedure the used gas acetylene  $C_2H_2$  is decomposed catalytically to  $2C + H_2$  and acts as carbon source for the assembly of the nanostructures.

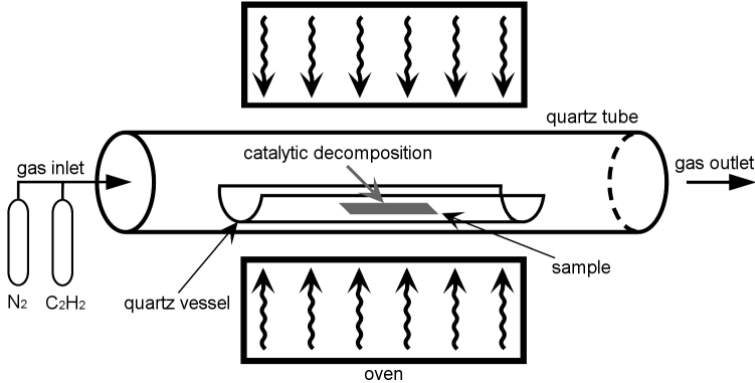


Figure 2.6: *Sketch of the flow reactor for chemical vapor deposition.*

The used horizontal CVD flow reactor is a heated quartz tube (Fig. 2.6). Some experiments work under ambient pressure and some under a pressure of some mbar. A quartz vessel is used to transfer the samples into the middle of the oven. On one end of the tube the gases are introduced and at the other end they either leave the tube into a gas trap or are pumped out by a primary pump. The oven works typically at temperatures between 600 and 1000°C.

## 2.4 Field emission

Field emission is the extraction of electrons from a solid by tunneling through the surface potential barrier [29]. As shown schematically in Fig. 2.7, the slope of the potential barrier is horizontal when no electric field is present. Its shape becomes triangular with a decreasing slope when a negative potential is applied to the solid, with a slope that depends on the amplitude of the local electric field  $F$  just above the surface. The local electric field is not simply  $V/d_0$ , which is the macroscopic field obtained with an applied voltage  $V$  between two planar and parallel electrodes separated by a distance  $d_0$ . The local field, in most cases, will be higher by a factor  $\gamma$ , which gives the aptitude of the emitter to amplify the field and is accordingly termed the field amplification factor.  $\gamma$  is determined solely by the geometrical shape of the emitter, and the field at the emitter surface is often written as  $F = \gamma E = \gamma V/d_0$ , where  $E$  is the macroscopic field. Tunneling through the surface barrier becomes significant when the thickness of the barrier is comparable to the electron wavelength in the solid. Field emission will most likely peak at the Fermi level

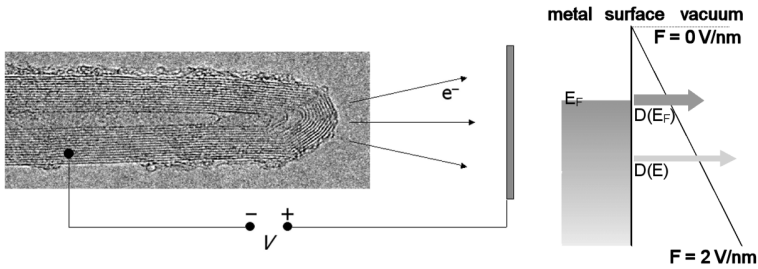


Figure 2.7: *Left: Sketch of a field emission experiment: a potential is applied between a nanotube and a counterelectrode. Right: Field emission model from a metallic emitter following the Fowler-Nordheim approach.*

and is influenced therefore by the work function  $\phi$ , as shown in Fig. 2.7. In fact, a simple model (the Fowler-Nordheim model [35]) shows that the dependence of the emitted current on the local electric field and the work function is exponential-like, with dependence

$$I \propto (F^2/\phi) \exp(B\phi^{3/2}/F)$$

with  $B = 6.83 \times 10^9 \text{ (V eV}^{-3/2} \text{ m}^{-1})$ . As a consequence, small variations of the shape or surrounding of the emitter (which determine the geometric field enhancement  $\gamma$ ) and/or the chemical state of the solid or of its surface (which influence the work function) have a strong impact on the emitted current. One can also estimate either  $\phi$  or  $\gamma$  from measurements, provided that they follow the Fowler-Nordheim model. This can be done with a Fowler-Nordheim plot, i.e. by plotting  $\ln(I/V^2)$  versus  $1/V$ . One should obtain a slope that depends on  $\phi$ ,  $\gamma$  and  $d_0$ . For carbon film emitters,  $\phi$  is usually taken as 5 eV. Note that the Fowler-Nordheim model is valid only for flat surfaces at 0 K, and is in many cases not satisfactory. The model is, however, simple and widely used.

Field emitters have several advantages over thermoelectronic emitters. First, the emitter does not have to be heated, which eliminates the need for a heat source or a heating loop. The energy spread of the emitted electrons is also far narrower. Such emitters are easy to realize in microscopic dimensions and to incorporate in emitter arrays, and, finally, the emitted current can be controlled with the applied voltage. It is therefore not surprising that researchers are aiming at replacing thermoelectronic with field emitters in various applications. Displays (with one or several electron sources for each pixel) and microwave tubes are two examples.

Carbon nanotubes are one of the most intriguing field emitters. They possess the following properties favorable for field emitters: (1) high aspect ratio, (2) small radius of curvature at their tips, (3) high chemical stability and (4) high mechanical strength.

The field emission measurements were performed using the examined samples as cathodes. The emitted electrons were collected on a highly polished stainless steel spherical counterelectrode of 1 cm diameter, which corresponds to an emission area of  $\sim 0.007 \text{ cm}^2$ . The

distance between the electrodes was adjusted to  $125\ \mu\text{m}$ . A Keithley 237 source-measure unit was used to supply the voltage (up to 1000 V) and to measure the current with pA sensitivity, allowing the characterization of current-voltage ( $I - V$ ) behavior.

## 2.5 Raman spectroscopy

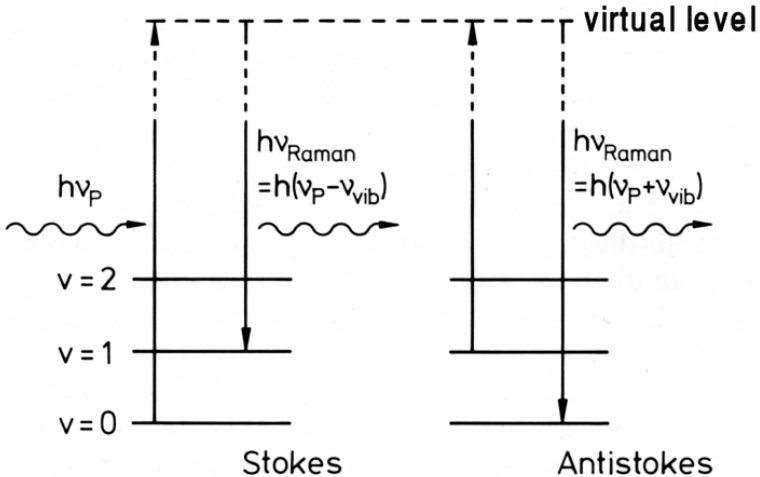


Figure 2.8: Sketch of the vibrational Raman scattering for the explication of the Stokes and the Anti-Stokes lines. The primary light combines a real starting level of the solid with a virtual level.

Raman scattering is an optical process involving the simultaneous emission or absorption of a phonon associated with the scattering of a photon. This shifts the frequency of the scattered photon. Raman scattering was initially developed as a spectroscopic tool and has proven to be a very useful technique for studying the thermal, structural, and chemical properties of materials [36].

Hitting a solid a photon can be re-emitted with a lower (Stokes) oder higher (Anti-Stokes) frequency [37]. This is due to a scattering with phonons of the solid. In contrast to Rayleigh scattered light, the Raman scattered light is not coherent with the light of the primary beam. The frequency shifts are independent of the frequency of the primary light. It is just a function of the scattering solid. Using classical considerations the Stokes and Anti-Stokes lines should possess the same intensity but quantum-theoretical considerations show that the Raman effect is based on an inelastic photon scattering which starts at the Stokes lines on a level with a small vibration quantum number and

ends on a vibration level with higher quantum number, whereas with the Anti-Stokes effect the scattering process shows the inverse behavior. The resulting frequencies are  $\nu = \nu_p - \nu_{vib}$  for the Stokes lines and  $\nu = \nu_p + \nu_{vib}$  for the Anti-Stokes lines with the primary light frequency  $\nu_p$  (Fig. 2.8). The difference  $\nu_p - \nu$  is called Raman shift. During the Stokes scattering the solid absorbs energy from the photon whereas during the Anti-Stokes scattering the solid delivers energy to the photon. The intensity ratio between Stokes and Anti-Stokes lines are given by the occupation probability  $n$  of the initial states which are calculated with the Boltzmann equation. With decreasing temperature the Anti-Stokes lines become weaker. For the intensity holds the equation

$$\frac{I_{Anti-Stokes}}{I_{Stokes}} = \frac{n(v=1)}{n(v=0)} = \exp(-h\nu_{vib}/kT)$$

In this work information about the vibrational properties of the nanostructures was obtained by micro-Raman spectroscopy, i.e. the laser was focused on a spot of the sample in the order of some  $\mu\text{m}$  using an optical microscope. The scattered light is collected by the microscope objective lens and deflected to a spectrometer. The Raman spectra were recorded in backscattering configuration using the 514.5 nm line of an  $\text{Ar}^+$  ion laser and a DILOR XY 800 spectrometer. An incident maximum laser power of 20 mW was applied in order to avoid peak shifts due to thermal heating or structure transformations during data acquisition. A spot size of approximately 2  $\mu\text{m}$  was achieved with a 250 $\times$  Olympus microscope objective. The spectra were calibrated using a natural diamond single crystal. The instrument was provided by Heiko Seehofer from the Département des Matériaux of the EPFL.

Raman scattering offers a unique tool to characterize carbon materials such as graphite, diamond and carbon nanotubes, since the amount of ordering and degree of  $sp^2$  and  $sp^3$  bonding leaves a unique Raman "fingerprint". Raman scattering depends also on the size of the graphite crystals [38]. Therefore, Raman spectroscopy is used here to identify carbon nanotubes and to characterize the obtained carbon structures by their degree of crystallinity.

## 2.6 Spectrophotometry

Spectrophotometry is the quantitative measurement of the reflection or transmission properties of a material as a function of wavelength.

The amount of electro-magnetic radiation absorbed by a species in a solution  $A$  depends on its concentration  $c$ , the path length of the electro-magnetic radiation  $l$ , and the specific molar absorptivity  $\epsilon$  of the species. This is defined as Beer-Lambert's Law  $A = \epsilon lc$ . The absorption of energy also depends upon the intensity of the incident light  $I_o$ , and the intensity of the exiting electro-magnetic energy  $I$ , where the absorption is defined as  $A = \log(I_o/I)$ . Thus the light transmittance (which is the relative percentage of light transmitted through the sample) is  $T = \exp(-A)$  this leads to  $T = I/I_o = \exp(-\epsilon lc)$ . Some light intensity is lost to light scattering and reflection at the cuvette interfaces, but this is considered to be negligible in most spectrophotometers today.

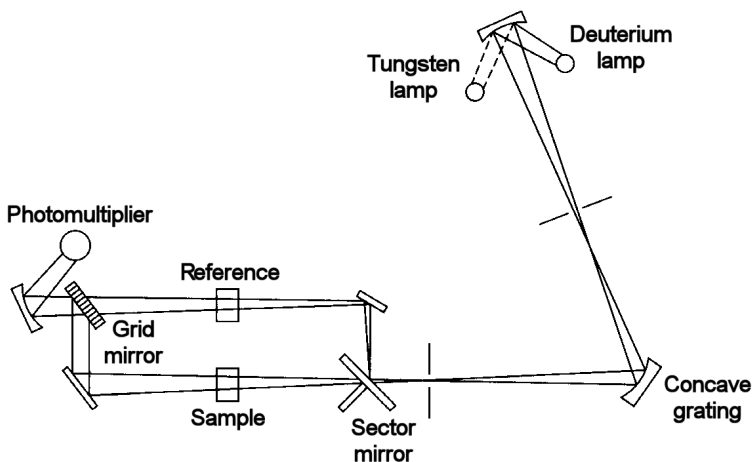


Figure 2.9: Schematic of a typical double-beam spectrophotometer for the ultraviolet/visible light range [39].

There are five major components to a UV-Vis spectrophotometer (detecting ultra-violet and visible light): a radiation source, a wavelength selector, a sample cell or sampling device, a detector, and a readout device. The radiation source for ultraviolet measurements is usually a hydrogen or deuterium lamp and a tungsten lamp for visible measurements. The radiation source must provide sufficient radiant energy over the wavelength region where absorption is to be measured and should maintain a constant intensity over the time interval during which measurements are made. UV-Vis spectrophotometers have to be able to distinguish between discrete bands of radiation effectively. This is done by a wavelength selector. The two major wavelength selectors are filters and monochromators. Cuvettes, or cells that contain the sample to be analyzed, should have parallel sides that are perfectly perpendicular to the radiation source. The cuvette used in UV-Vis spectrophotometry usually has a path length of 1 cm. The cuvette can be manufactured from several materials including fused silica, quartz, and plastic. Quartz cuvettes are transparent to UV and visible radiation and therefore are more commonly used for UV-Vis spectrophotometry.

The detector changes the radiation transmitted from the UV-Vis Spectrophotometer into a current or voltage for the readout device to use. Solid-state photodiodes, photoemissive tubes and photomultiplier tubes are commonly used as single element detectors while solid-state array detectors are used as multi-element detectors.

Readout devices use the current or voltage produced by the detector and amplifies it. The readout device then converts the current or voltage into a form that the analyst can read

as a printout.

Many modern spectrophotometers are based upon a double-beam design. Fig. 2.9 illustrates such an instrument which offers the advantage that it compensates for all but the most short-term fluctuations in the radiant output of the source as well as for drift in the transducer and amplifier. It also compensates for wide variations in source intensity with wavelength. Furthermore, the double-beam design lends itself well to the continuous recording of transmittance or absorbance spectra [39].

In the frame of this thesis the development of a used catalyst ink (iron salt solution) with time was recorded with a Shimadzu UV-260 Recording Spectrophotometer in the wavelength range between 300 and 900 nm in transmission mode.

## 2.7 Electron microscopy

### 2.7.1 Transmission Electron Microscope

The transmission electron microscope (TEM) is a derivative of the light microscope, making use of the shorter wavelength electron illumination [40]. In its simplest form it has exactly the same lens arrangement as its light counterpart, unless that it uses electron lenses (Fig. 2.10). It has been developed further to make fuller use of the special properties of electron illumination: principally the higher resolution, but also the ability to carry out various forms of elemental and crystallographic microanalysis.

The simplest electron microscope has two image-forming lenses and is an exact analogy of the compound light microscope. The illumination coming from an electron gun is concentrated on the specimen by a condenser lens. After passing through the specimen the electrons are focused by the objective lens into a magnified intermediate image. This image is further enlarged by a projector lens and the final image is formed on a fluorescent screen, a photographic film or a CCD (charge-coupled device) camera. Nowadays, TEMs can reach atomic resolution using voltages of 200 kV and higher.

The inner morphology of the tubular carbon structures discussed in this thesis and their crystallinity were imaged by such a high-resolution TEM. A Philips EM 430 transmission electron microscope equipped with a Gatan image plate operating at 300 kV (point resolution 0.3 nm) was used. The electron microscopy was performed at the Centre Interdépartmental de Microscopie Electronique (CIME) of the EPFL. For the examination of the development of the used catalyst ink with temperature a resistively heatable sample holder was used. By applying a current of about 600 mA temperatures up to 1000°C could be reached in situ.

The crystal planes of solids act as selective reflectors of incident radiations such as x-rays or electrons. It was shown by Bragg that there is a reinforcement of reflections from successive parallel planes when the angles of incidence and reflection  $\theta$  satisfy the relationship  $2d \sin \theta = n\lambda$ , where  $d$  is the lattice spacing between atomic planes,  $\lambda$  is the wavelength of the radiation, and  $n$  is an integer. At other angles of incidence the reflected waves from successive planes cancel each other out.

When a parallel beam of electrons falling on a crystal at the correct angle of incidence for diffraction to occur from a set of lattice planes, the diffracted beam is deviated through



an angle of  $2\theta$  from the undeviated beam. If a fluorescent screen is placed at a distance  $L$  from the crystal, the diffraction spot will be displaced from the undeviated beam by a distance  $R$  such that  $R = L \tan 2\theta \simeq 2\theta L$ . Combining this relationship with Bragg's Law we see that  $R/L = n\lambda/d$ , or  $d = \lambda L/R$  for first order ( $n = 1$ ) diffraction. So if  $\lambda$ ,  $L$  and  $R$  are known,  $d$  may be calculated.

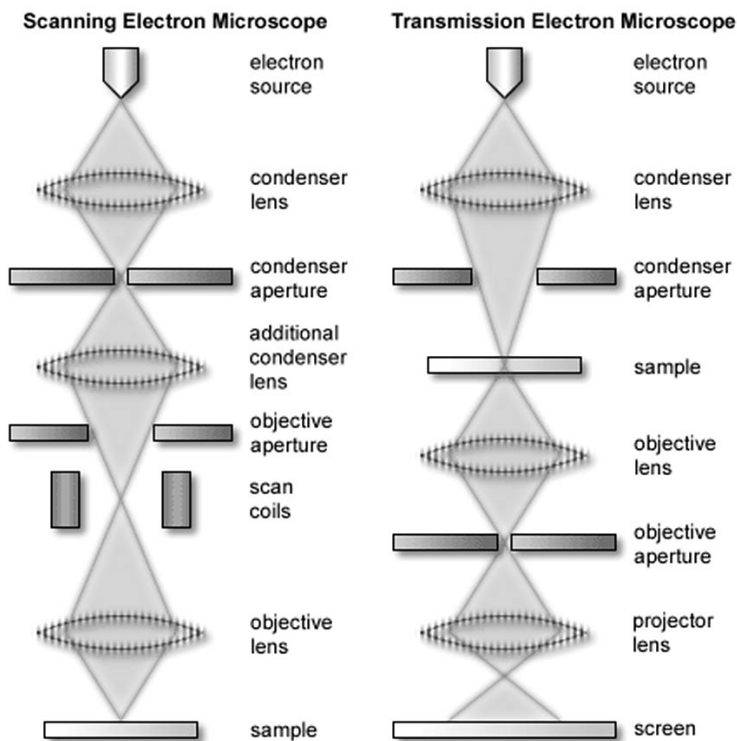


Figure 2.10: *Electron path in a scanning and a transmission electron microscope [41].*

If the single crystal is now replaced by a cluster of randomly oriented crystals, diffraction of electrons will occur from those crystals satisfying the Bragg relationship with the incident electron beam, and a hollow cone of diffracted rays will be formed which intersects the screen as a ring of radius  $R$ . The breadth of the ring is determined by the size of the diffraction crystals. At its narrowest it is the width of the electron beam falling on the crystal, and it becomes broader and more diffuse as the crystals become smaller.

This diffraction technique in a TEM relies upon the fact that the electron beam after diffraction in the specimen forms a miniature diffraction pattern (rings or spots) in the back focal plane of the objective lens (see Fig. 2.10). If the first projector lens is now weakened so that it is focused in this plane instead of the image plane of the objective lens, the pattern is projected - enlarged - onto the screen of the microscope. If the lens currents for this mode of imaging are preset the electron microscope can be switched alternately between projecting an enlarged image of the specimen and its diffraction pattern. Later in this thesis the formation and the crystallinity of iron clusters out of the used catalyst solution will be studied by TEM diffraction as function of temperature.

## 2.7.2 Scanning Electron Microscope

The scanning electron microscope (SEM) is used to study the surface of materials rather than their internal arrangement. Its ability to resolve fine detail lies intermediate between the light microscope and the high resolution TEM. This instrument differs from all other conventional microscopes, using light or electrons, in forming its image progressively and not all at once.

Electro-optically, the SEM has little in common with the TEM apart from the use of an electron gun and a condenser lens system to produce a focused electron beam. These two or three lenses are the only ones in the column - there are no lenses after the specimen but an electron collector. As illustrated in Fig. 2.10 a very fine beam of electrons with energies up to 30 keV is focused at the surface of the specimen in the microscope and scanned across it in a pattern of parallel lines. A number of phenomena occur at the surface under electron impact: most important for scanning microscopy are the emission of secondary electrons (originated from specimen atoms by collision with high energy electrons, be it primary electrons entering the specimen or backscattered electrons on their way out of it) with energies of a few tens of eV, and re-emission or reflection of high-energy backscattered electrons from the primary beam. The intensity of emission of both secondary and backscattered electrons is very sensitive to the angle at which the electron beam strikes the surface, i.e. to topographical features on the specimen. The emitted electron current is collected and amplified. Variations in the resulting signal strength as the electron probe is scanned across the specimen are used to vary the intensity of a corresponding spot of a raster image synchronous with the probe. A standard instrument can usually reach a resolution of less than 10 nm.

Scanning electron microscopy was performed to analyze the microstructures in plan view. A Philips XL 30 microscope equipped with a field emission gun (FEG) operating at an acceleration voltage between 3 and 5 kV, a working distance of typically 10 mm, and in secondary electron (SE) image mode was used.

## Chapter 3

# Catalytic growth of carbon nanotubes films

Carbon nanotubes [2] have been studied already for more than ten years and are now considered for applications in miscellaneous devices such as tubular lamps [42], flat panel displays [16], lighting elements [43] and nanometric electronic devices [44, 45]. Such devices make precise demands on the properties of the tubes, as the length, diameter and electronic properties have a strong influence on the final performance of the device. This implies that the nanotube growth has to be controlled and understood. However, the growth mechanism is at present poorly understood, be it for arc discharge, laser ablation, or catalytic growth [46].

In this work the CVD method is used in combination with heterogeneous catalysis and microcontact printing to grow patterned films of multi-wall carbon nanotubes [27]. The catalytic deposition is the most practical method to create nanotubes on extended surfaces. Microcontact printing ( $\mu$ CP) has become an often applied method in the last few years because it is a simple way to define chemical patterns on a variety of substrates [32, 34, 47]. This method is used here to selectively deliver a catalyst to the substrate surface, which in turn activates the CVD growth of nanotubes [27]. The advantage of the patterning is that one can compare the regions with and without catalyst, and thus exactly determine the role of the catalyst. In order to better understand the catalytic growth, the parameters deposition temperature, catalyst composition, catalyst concentration and deposition time are examined systematically.

It is found that the catalyst has an influence on the morphology of the grown structures, and that iron is better suited for the low temperature growth of nanotubes than nickel or cobalt. The diameter of the nanotubes increases with the deposition temperature. Raman spectroscopy and Transmission Electron Microscopy (TEM) were performed to elucidate the crystalline structure of those objects.

It is demonstrated that combining Scanning Electron Microscopy (SEM), Transmission Electron Microscopy (TEM) and Raman spectroscopy allows an optimization of crystallinity and morphology of carbon nanotubes while gaining new information about the development of the used ink and the structure of the considered objects.

### 3.1 Synthesis of nano-structured material

<100>-oriented boron doped silicon with the native SiO<sub>2</sub> layer was used as substrate. The stamps for  $\mu$ CP were prepared by curing poly(dimethyl)siloxane (PDMS) for at least 12 h at 70°C on a structured master that was prepared by contact photo-lithography [26]. The width of the square patterns on the wafer is 5  $\mu$ m. The stamps were subsequently hydrophilized by an oxygen plasma treatment (O<sub>2</sub> pressure  $\sim$ 0.8 Torr, load coil power  $\sim$ 75 W, 60 s). The stamp was loaded with 0.2 ml of catalyst solution for 30 s and then dried in a nitrogen stream for 10 s.

The solutions were Fe(NO<sub>3</sub>)<sub>3</sub>·9H<sub>2</sub>O, Ni(NO<sub>3</sub>)<sub>2</sub>·6H<sub>2</sub>O or Co(NO<sub>3</sub>)<sub>2</sub>·6H<sub>2</sub>O dissolved in ethyl alcohol at concentrations between 50 and 200 mM (in the following the used inks will shortly be referred as iron/nickel/cobalt ink). The solutions were used 12 h after preparation because they undergo a certain "aging" process. A period of 12 h for this aging of the solution was found to be ideal for the catalytic growth of nanotubes [27]. The printing was performed by placing the stamp on the surface of the Si/SiO<sub>2</sub> wafer for 3 s (see Chapter 2.2).

The samples were placed in a horizontal flow reactor (quartz tube of 14 mm diameter in a horizontal oven) directly after the printing (see Chapter 2.3). The treatment in the CVD oven proceeded in three steps (if not explicitly mentioned different). In the first step, the catalyst was annealed for 20 min under a flow of 80 ml/min of nitrogen to transform the catalyst to crystal grains with a size in the order of nanometers and to clean the reactor atmosphere. The actual deposition was performed with 80 ml/min of nitrogen plus 20 ml/min of acetylene (carbon source for the catalytic growth) at atmospheric pressure for 30 min. The third step was a final annealing of 10 min under 80 ml/min of nitrogen. The same temperature was used throughout the entire procedure, which implies that a change of the temperature affected all the steps.

## 3.2 Characterization of the ink

### 3.2.1 Evolution of the catalyst in solution

In order to follow the evolution of the catalyst in the ethanolic solution (also designated as "aging") spectrophotometric measurements have been performed. By means of adding an acid to the solution (H<sub>2</sub>SO<sub>4</sub>) the development could be influenced and prevented. In Fig. 3.1 four transmission light spectra of a 100 mM iron ink with different amounts of H<sub>2</sub>SO<sub>4</sub> are shown. The spectra were recorded with a spectrophotometer in the wavelength range between 300 and 900 nm. In each frame the development of the ink is shown in dependence of time. One can see that the transmission is lowering with time (time difference between two measurements: 1.5 h). For a simple iron ink the intensity is lowered for all wavelengths in the considered range and the strong rise at about 550 nm is shifted to higher wavelengths. Between 550 nm and 900 nm (max. of the instrument) the transmission remains on a high level (>75%) which yields the typical reddish-brown color of the iron ink. After some days of aging a segregation of a gel-like part in the solution was observed.

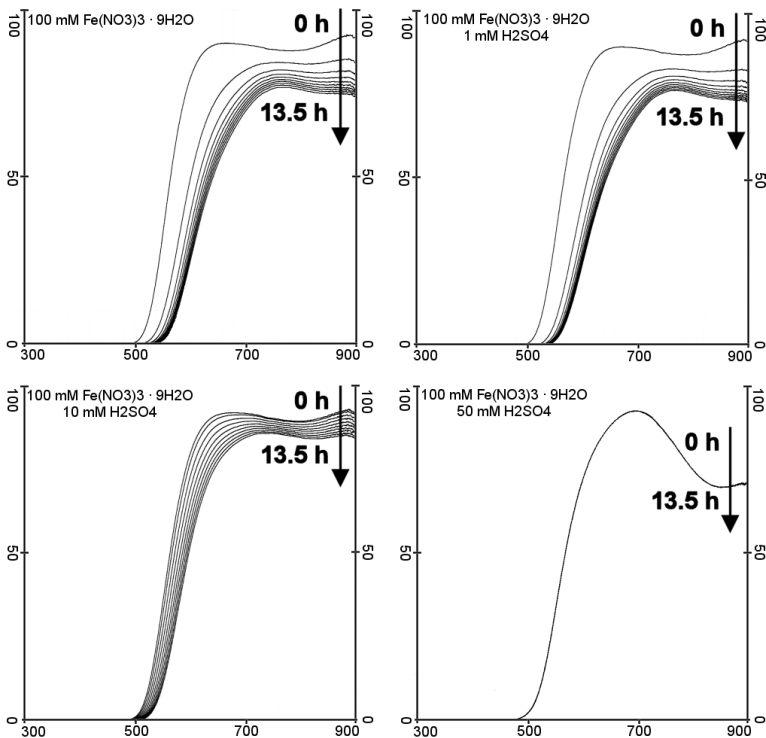


Figure 3.1: Transmission light spectra with addition of 0 mM, 1 mM, 10 mM and 50 mM of  $\text{H}_2\text{SO}_4$  to a 100 mM iron ink demonstrating the aging effect of the ink and its prevention. Each set of measurements lasted 13.5 h, whereas between two recording 1.5 h elapsed. With 50 mM  $\text{H}_2\text{SO}_4$  in the solution all curves coincide on one line.

These effects are interpreted as the slow formation of complexes (e.g. like iron(III) hydroxide  $\text{Fe}(\text{OH})_3$ ) which readily undergo polycondensation reactions and a gel-like polymer is formed [48]. This is supported by the fact, that the observed "aging" can be inhibited by adding an acid, which stabilizes the solution. 1 mM of  $\text{H}_2\text{SO}_4$  does not show much effect. 10 mM of  $\text{H}_2\text{SO}_4$  pushes the spectrum together and back to lower wavelengths. An amount of 50 mM of acid suppresses this aging effect, i.e. the spectrum stays the same during the whole period of 13.5 h of observation. The prevention of the polycondensation might be caused by the elimination of solvated  $\text{OH}^-$  by  $\text{H}^+$  ions ( $\text{H}^+ + \text{OH}^- \rightarrow \text{H}_2\text{O}$ ). But an oversupply with acid (like 50 mM  $\text{H}_2\text{SO}_4$ ) results also in a change of the spectrum.

Higher wavelengths, above about 700 nm, are slightly attenuated.

### 3.2.2 Evolution of the catalyst particles during annealing

A dried up iron nitrate solution was heated in situ in a TEM in order to follow the evolution of the catalyst ink (dried iron nitrate solution) and the formation of catalyst grains during the heat treatment step of the CVD process. At increasing temperatures the samples have been imaged and diffraction measurements have been performed to prove the crystallinity of the grains.

For those in situ diffraction measurements of the used ink in a TEM a 100 mM iron nitrate solution was dried on a silicon oxide film on a TEM copper grid. The dried solution forms a soft film of  $\text{Fe}_2\text{O}_3$  and  $\text{Fe}(\text{NO}_3)_3$  on the sample. This is due to the re-formation of the solved salt  $\text{Fe}(\text{NO}_3)_3$  (out of  $\text{Fe}^{3+}$  and  $3\text{NO}_3^-$ ) and an oxidation of the complexes in air.

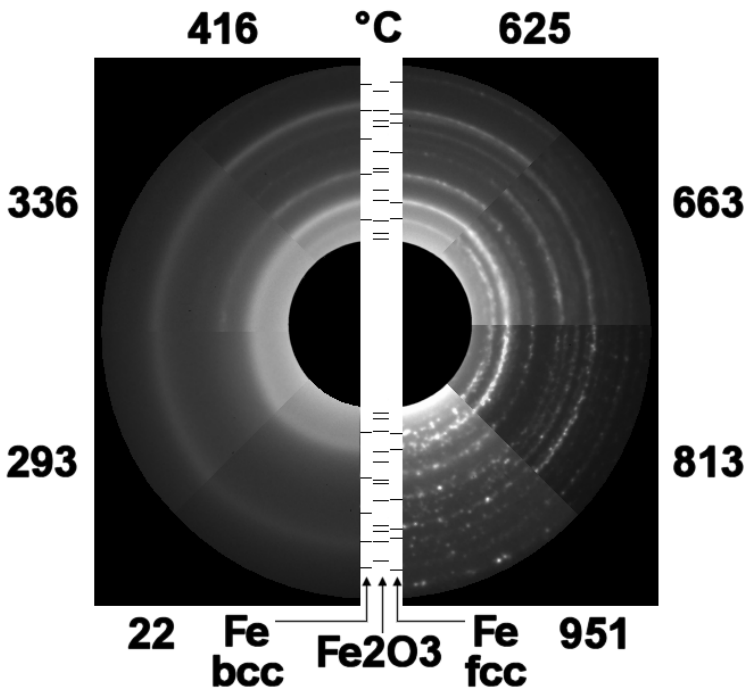


Figure 3.2: TEM diffraction patterns of a 100 mM iron nitrate solution heated in situ up to 951°C. In the center: calculated patterns for bcc iron,  $\text{Fe}_2\text{O}_3$  and fcc iron.

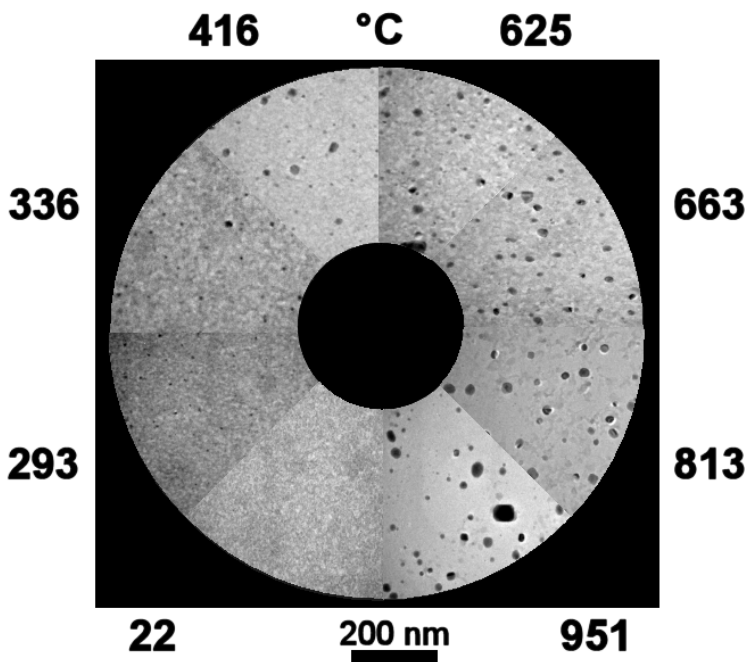


Figure 3.3: TEM real-space images of the development of iron clusters while heating the used iron ink (100 mM iron nitrate solution) in situ up to 951°C.

At initial ambient temperature the diffraction of the ink shows amorphous character (Fig. 3.2). Employing in situ heating of the ink the film starts to transform at about 336°C. It shows diffraction rings which are typical for randomly oriented crystal structures. With higher temperatures more and more diffraction rings appear. The diffraction rings are sharpest at 663°C. At higher temperatures they "decay" to more and more individual spots which indicates less and larger individual crystals. These results suggest an increasing crystallinity of the catalyst with increasing temperature and a coalescence of smaller particles to larger ones. Counter-balancing the drift in the individual diffraction images the compilation in Fig. 3.2 was shifted in such a way that the second ring always stays on the same level.

The observed patterns can fully be explained by the electron diffraction of lattice planes of bcc and fcc iron. But the rings can also be explained by the diffraction of  $\text{Fe}_2\text{O}_3$  crystals. Maybe  $\text{Fe}_2\text{O}_3$  is available as well as pure iron. This might be due to a reduction

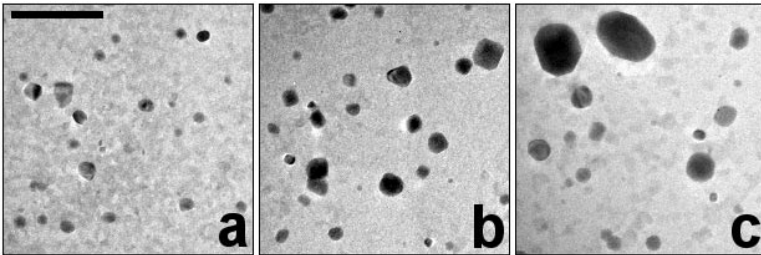


Figure 3.4: TEM images of iron clusters at (a) 663°C, (b) 747°C, and (c) 893°C. The crystal facets are clearly visible. The scale bar in the upper left corner of image (a) indicates 200 nm.

of  $\text{Fe}_2\text{O}_3$  by the SiO support ( $6\text{SiO} + 2\text{Fe}_2\text{O}_3 \rightarrow 6\text{SiO}_2 + 4\text{Fe}$ ) or organic components in the vacuum of the TEM. The used TEM grid are furnished as "silicon monoxide support films" by Plano (Wetzlar, Germany). But it cannot be excluded that they oxidize in air (at least partly) to  $\text{SiO}_2$  [49] which would indeed exclude the possibility of reduction by the substrate. In situ XPS measurements could provide more detailed information about the nature of the catalyst under the respective conditions. But for the later nanotube growth, anyway, it is assumed that the iron oxide  $\text{Fe}_2\text{O}_3$  is first reduced to pure iron ( $\text{Fe}_2\text{O}_3 + 3\text{C}_2\text{H}_2 \rightarrow 2\text{Fe} + 6\text{C} + 3\text{H}_2\text{O}$ ) before the actual catalysis starts.

The electron diffraction suggests an increase of the amount of crystallized ink and an increase of the crystal size with temperature. This could be confirmed with real space images which were taken right after the diffraction at the same temperatures (Fig. 3.3). At 293°C the first dark spots indicate the beginning of a formation of nano-crystals. The average size is about 5 nm. At higher temperatures the average size and the size distribution are rising (Tab. 3.1). But at all temperatures one can always find also much smaller particles (e.g. 3 nm).

The particle formation (which was also videotaped) is due the oxidation of  $\text{Fe}(\text{NO}_3)_3$  to  $\text{Fe}_2\text{O}_3$  ( $4\text{Fe}(\text{NO}_3)_3 \rightarrow 2\text{Fe}_2\text{O}_3 + 12\text{NO}_2 + 3\text{O}_2$ ) [50] and a surface ripening at higher temperatures. The amorphous gel-like structure (iron nitrate + iron oxide + slightly bound ethanol) denatures, the rest of ethanol evaporates, the solid parts diffuse on the substrate SiO/SiO<sub>2</sub> and condensates at certain germs supported by the augmented mobility at higher temperatures. The created nano-crystals grow with higher temperatures.

Table 3.1: Table of the estimated size distribution of the nanocrystals during the annealing.

Temperature [°C]	Diameter [nm]
293	5
336	7
416	8 - 25
625	8 - 30
663	10 - 35
813	12 - 50
951	15 - 70



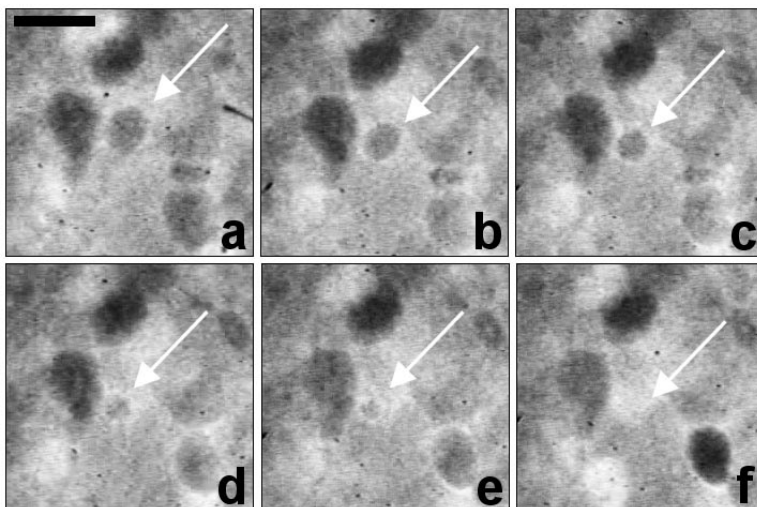


Figure 3.5: *Ostwald ripening at 85°C observed with a pristine catalyst film (100 mM iron nitrate solution). The elapsed time between two frames is about 4.4 s and the scale bar in the upper left corner of image (a) indicates 200 nm.*

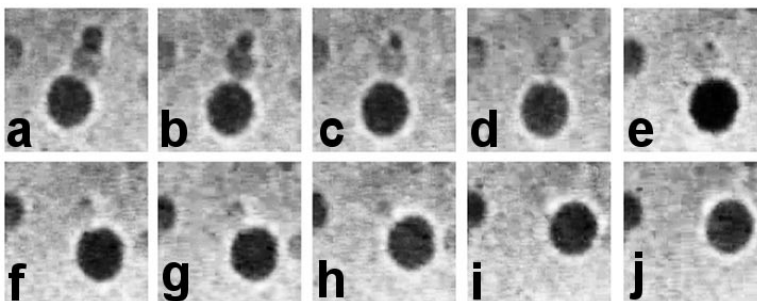


Figure 3.6: *Double Ostwald ripening at 98°C: A small cluster is absorbed by a medium one (a-e) and the medium one in turn by a big one (f-j). The elapsed time between two frames is about 0.8 s and one image is about 200×200 nm<sup>2</sup>.*

The crystallites are solid at least up to temperatures of about 1000°C. This is proven not only by the electron diffraction but also in the real-space images in Fig. 3.3, and even more

clearly in Fig. 3.4: defined facets are visible on the crystallites. At temperatures of more than about 600°C a high mobility of material was observed and video-taped. This mobility led to a visible ripening of the catalyst particles. Crystals grew by absorbing material from the vicinity (amorphous catalyst film) and larger crystallites continued growing at the expense of smaller ones nearby, known as Ostwald ripening [51]. In Fig. 3.5 a cut-out of the video-taped sequences is shown which demonstrates the growth of a cluster at the expense of a smaller one (white arrows). Another cut-out is shown in Fig. 3.6. One can nicely see the three clusters. The smallest one, at the top of the three, is quickly getting smaller and vanishes first (a-e). The middle one seems to get smaller after the small cluster disappeared (f-j), but undergoes a reduction probably already before, or the mass flow from the small particle to the biggest one keeps the medium one stable during the first period. Finally just the biggest one remains on the surface. Here, it was observed a double Ostwald ripening. The images are taken at 987°C and have a size of about  $200 \times 200 \text{ nm}^2$ . The elapsed time between two frames is about 0.8 s. This Ostwald ripening takes presumably place at lower temperatures as well, but is much slower and is thus harder to observe due to drift problems.

It is assumed that the printed catalysts nickel and cobalt show similar properties like demonstrated here for the iron ink.

### 3.3 Morphology

In further experiments the influence of (a) the catalyst solutions containing iron, nickel or cobalt ions, (b) the deposition temperature, (c) the concentration of the catalyst and (d) the deposition time on the nanotube growth has been studied systematically. Concentrations of 50 mM and 100 mM of the three catalysts were used at temperatures between 580°C and 1000°C in 70°C steps. For the catalyst iron, which produced the highest amount of nanotubes, samples with a concentration of 150 mM and 200 mM at 650°C were also examined.

#### 3.3.1 Printing homogeneity

After the catalytic growth of the structures, the observation by SEM showed a homogeneous growth over the whole sample surface ( $>1 \text{ cm}^2$ , Fig. 3.7). The nanotubes grow only where the catalyst has been printed, and the bare substrate seems to be free of any carbon form for growth temperatures below 800°C. This implies that the used methods produce samples which are very suitable for the production of flat panel displays using field emission, because of the simplicity of the method and the low costs.

#### 3.3.2 Influence of the used catalyst

As displayed in Fig. 3.8, it was found that the use of the iron catalyst resulted in the highest fidelity of replication of the square pattern, whereas the use of a pure nickel or cobalt solution resulted in inferior patterning. Because of the wetting behavior on the

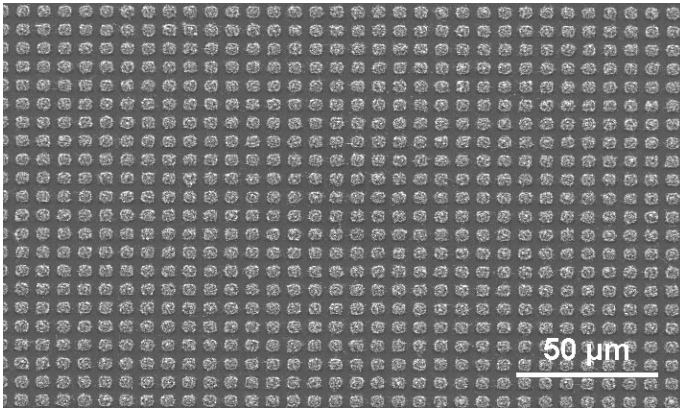


Figure 3.7: SEM micrograph demonstrating the homogeneity of the patterning on a  $\text{Si}/\text{SiO}_2$  sample (Nanotubes generated by 100 mM iron nitrate solution at  $720^\circ\text{C}$ ).

stamp [27], the nickel and the cobalt solution produced one drop on each square structure of the stamp, which was transferred to the substrate. As a result, the patterns obtained with cobalt and nickel are small and of irregular, circle-like shape. At concentrations higher than 100 mM the printing of the iron solution became also more difficult.

The comparison of the three catalysts shows that iron produced the highest density of carbon structures at any considered temperature, as seen in Fig. 3.8. Nickel and cobalt turned out to be not as good catalysts as iron, as only few nanotubes were found at  $720^\circ\text{C}$  with 100 mM nickel and cobalt solutions. At  $1000^\circ\text{C}$ , the printed nickel and the cobalt solution initiated the growth of spherical carbon structures, and iron caused the growth of thick worm-like structures.

### 3.3.3 Deposition temperature

Using the iron containing solution the carbon nanotubes and carbon structures grow with random orientation from the inked squares on the silicon surface. In Fig. 3.9 one can nicely see the increase of the diameter from thin nanotubes at  $650^\circ\text{C}$  to thick "carbon worms" at  $1000^\circ\text{C}$ . The diameter varies between 20 nm for the structures at  $650^\circ\text{C}$  and about  $1\ \mu\text{m}$  for the structures at  $1000^\circ\text{C}$ .

The catalytic growth of nanotubes started at a temperature of  $620^\circ\text{C}$ , but only a few nanotubes were observed at this temperature. A uniform coverage of each printed square was obtained at temperatures of  $650^\circ\text{C}$  and higher. The thinnest nanotubes were found at  $650^\circ\text{C}$  with iron as catalyst. The highest density of nanotubes was observed at  $720^\circ\text{C}$ . Using catalyst concentrations of 100 mM relatively thick worm-like structures were found at temperatures exceeding  $930^\circ\text{C}$  ("carbon worms"). Furthermore, the acetylene starts to

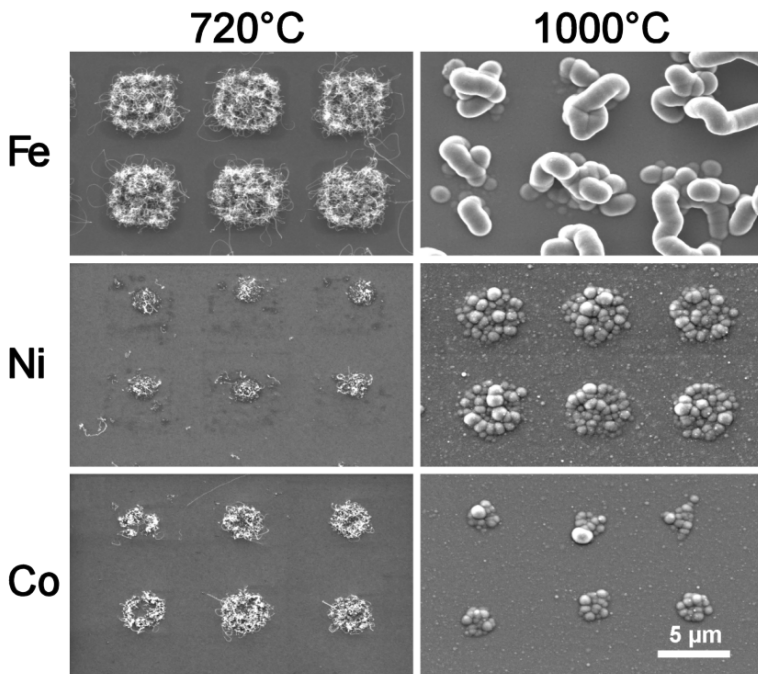


Figure 3.8: SEM micrographs demonstrating the effect of the catalyst on the nanotube growth: 100 mM solution of iron, nickel and cobalt nitrate at 720°C and 1000°C.

dissociate in the gas phase at temperatures above 800°C and the resultant carbon forms an amorphous continuous layer on the silicon surface of all samples. This layer gets also thicker with temperature.

### 3.3.4 Catalyst concentration

Fig. 3.10 shows clearly that the use of higher catalyst concentrations results in an increase of the nanotube density. But at concentrations higher than 100 mM the density leads to a kind of agglutination of the nanotubes. They do not grow anymore as individual tubes but in larger clusters. This is surely not the ideal configuration for the study of the nanotubes properties. In the following, the discussion is thus often focused on the catalyst inks with a concentration of 100 mM. Using catalyst ink of this concentration delivers the highest nanotube density without a clustering of the tubes.

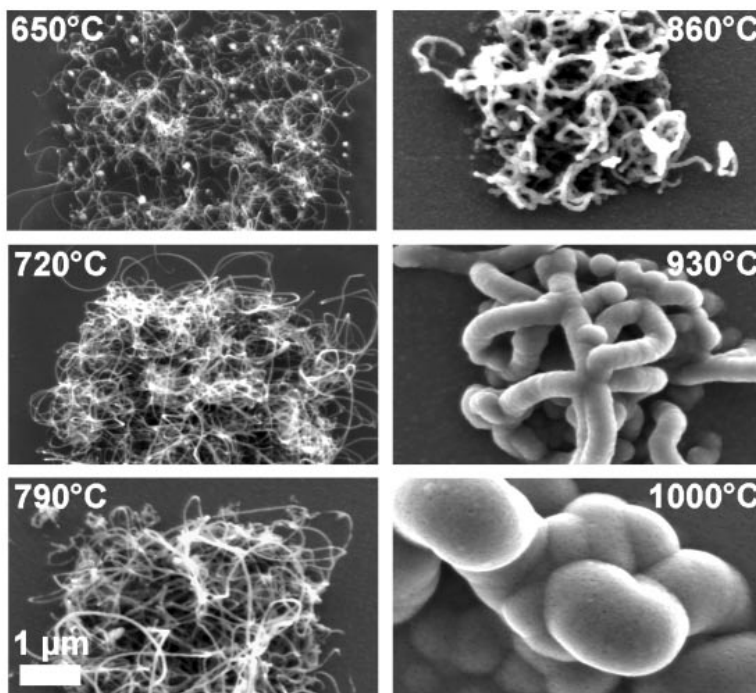


Figure 3.9: SEM micrographs of carbon structures obtained with 100 mM solution of iron nitrate at deposition temperatures from 650°C up to 1000°C (deposition time: 30 min).

### 3.3.5 Structure of the nanotubes

The nanotubes reached lengths of several  $\mu\text{m}$  with a diameter up to 30 nm. Transmission electron microscopy (TEM) of the samples obtained at 650°C using the 50 mM iron catalyst confirmed that the hollow structures are well-graphitized and well-separated multi-wall nanotubes (Fig. 3.11). The nanotubes have an inner diameter of about 15 nm and an outer diameter of about 30 nm. Most of them have open ends and some nanotubes contain encapsulated catalyst particles. In about ten percent of the nanotubes these particles were found at the top of the tube. In this case, the particles are of prolate shape and are aligned in the growth direction. They have diameters of about 8 nm and lengths of about 16 nm. The carbon structures grown at higher temperatures consist of a "nanotube core" and an additional layer of amorphous or polycrystalline carbon. Fig. 3.12a shows again a nanotube grown at 650°C. Alongside, Fig. 3.12b and c show a TEM image

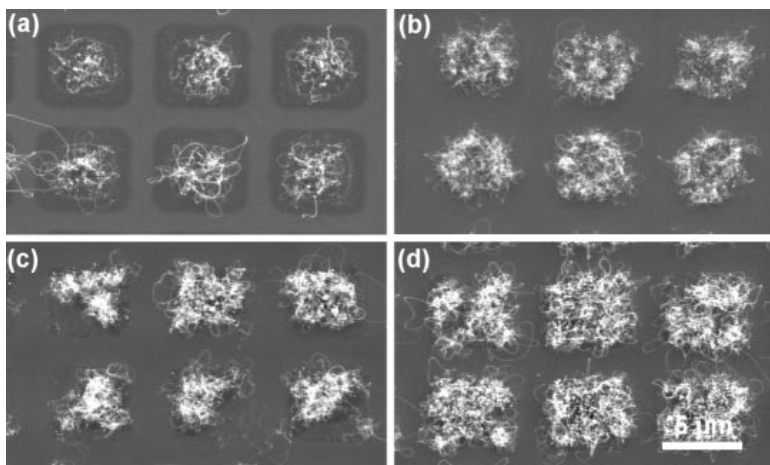


Figure 3.10: SEM micrographs demonstrating the effect of the concentration on the nanotube growth: a (a) 50 mM (b) 100 mM (c) 150 mM (d) 200 mM solution of iron nitrate at 650°C.

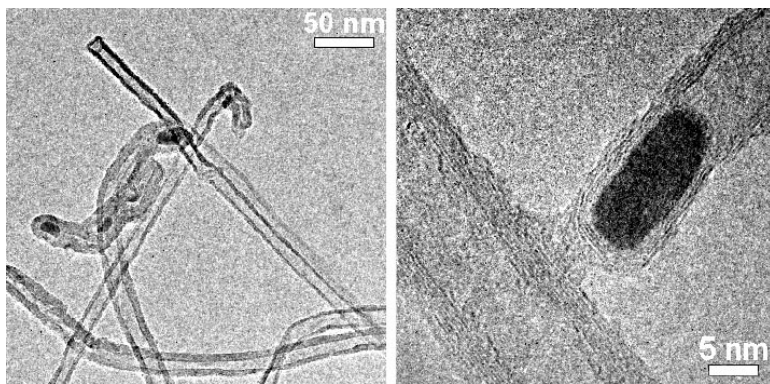


Figure 3.11: TEM micrograph of individual nanotubes grown at 650°C with a 50 mM iron solution.

of the structures obtained at 790°C resp. 930°C where a core structure is surrounded by flake-like carbon (indicated by arrows). The structures at 1000°C are too thick to be imaged by TEM.

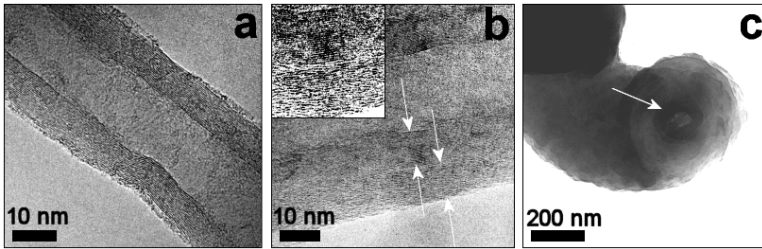


Figure 3.12: (a) TEM micrograph of a section of a carbon nanotube grown at  $650^{\circ}\text{C}$ . The graphitic layers of the hollow multi-wall nanotube are well visible. (b) TEM micrograph of a carbon structure grown at  $790^{\circ}\text{C}$  with a crystalline core and a polycrystalline outer shell. The core and the shell are delimited by arrows. The region of interest is enlarged in the inset. (c) TEM micrograph of a carbon structure grown at  $930^{\circ}\text{C}$  with an arrow indicating the nanotube core.

### 3.3.6 Deposition time

It was also found that the growth of the nanotubes is a very fast process: under the prevailing conditions the growth takes already place during the first 5 min. Fig. 3.13 shows the evolution of the nanotube growth with time at  $720^{\circ}\text{C}$ . After the annealing without CVD process only the printed catalyst patterns are visible. The observable surface has shrunken due to surface diffusion and the catalyst spots seems to have an halo which is the original size of the printed square. After 2 min of deposition some dots of carbonized catalyst appear in the center of the printed spots. Only 1 min later, nanotubes of up to  $10\ \mu\text{m}$  length are detected, which implies that the growth rate is of at least  $160\ \text{nm/s}$ . In the following time the density of the nanotubes increases but a significant increase in length could not be detected. The maximum length remains at about  $10\ \mu\text{m}$ .

### 3.3.7 Effect of the pattern

Using a pattern with printed  $5\ \mu\text{m}$  catalyst squares usually a random oriented growth of the nanotubes was observed. Just when the printing "failed" and the catalyst bridged two or more adjacent squares a dense self-aligned growth was observed. The nanotubes formed wall-like super-structures. This behavior was also observed when a  $10\ \mu\text{m}$  line pattern was used for the microcontact printing. It seems that a certain density and amount of nanotubes in the environment is necessary to build up those structures stabilized by van-der-Waals forces. But a high catalyst concentration only does not necessarily lead to such a structure as one can see by comparing Fig. 3.14 with Fig. 3.10. The pattern has an essential influence. A minimum lateral structure size is required. Just with a certain pattern width a self-stabilization of the structures is possible. Under the conditions considered here this threshold width seems to be between  $5$  and  $10\ \mu\text{m}$ .

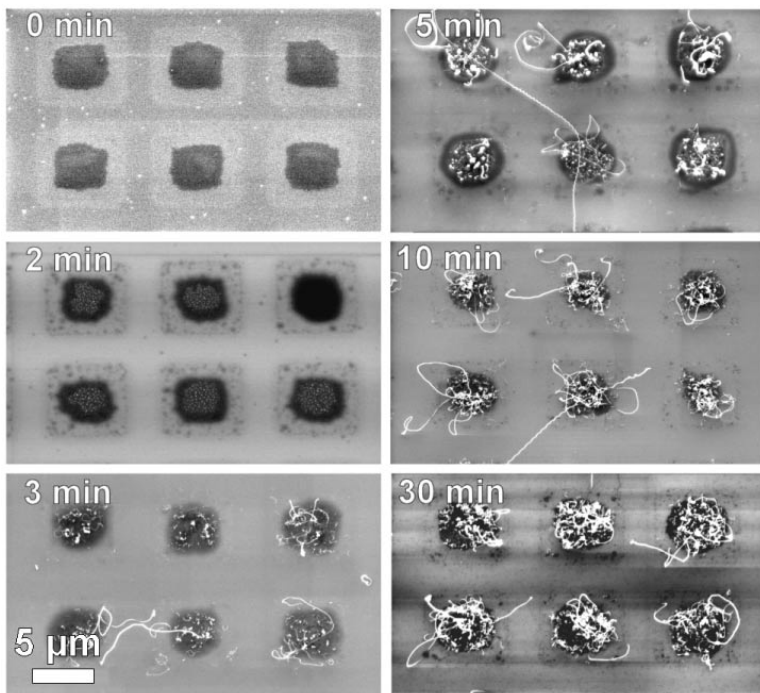


Figure 3.13: SEM micrographs demonstrating the time dependence of the growth of the carbon nanotubes by chemical vapor deposition (deposition temperature:  $720^{\circ}\text{C}$ ).

In contrast to the results in Chapter 3.3.6 where it was not possible to obtain nanotubes longer than  $10\ \mu\text{m}$ , an extended nanotube growth, i.e. a prolongation of the nanotube length was observed by adding a certain amount of hydrogen to the acetylene flow. Fig. 3.15 shows a  $100\ \text{mM}$  iron solution at a deposition temperature of  $720^{\circ}\text{C}$  with  $20\ \text{mbar}$   $\text{C}_2\text{H}_2$  and  $40\ \text{mbar}$   $\text{H}_2$ . Under these conditions an alignment of nanotubes in bundles was observed as well. The bundle growth starts at the printed catalyst squares. Even the separated bundles with a base of about  $5\times 5\ \mu\text{m}$  stabilize each other mutually. Their length is about  $100\ \mu\text{m}$ ,  $10 - 20\times$  longer than under the same conditions without hydrogen. It turned out that the amount of hydrogen is essential and hard to adjust. A minimal amount is needed (here e.g.  $40\ \text{mbar}$ ). A smaller concentration has no effect, while a slightly higher concentration etches away all of the nanotubes.



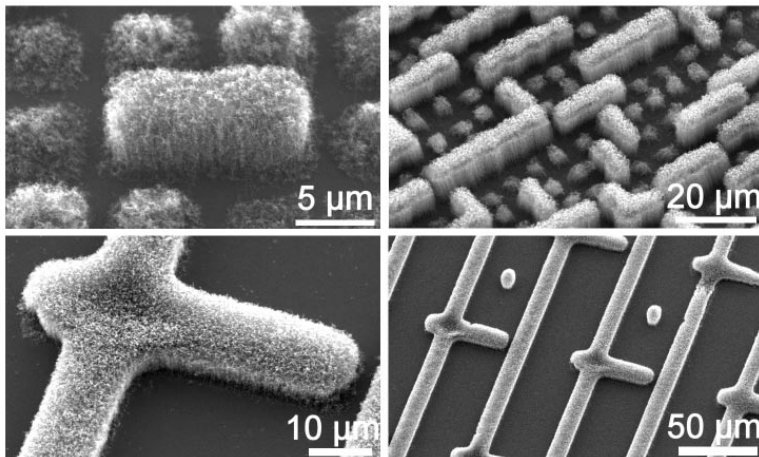


Figure 3.14: *SEM micrographs demonstrating the effect of the pattern (produced by  $\mu$ CP). First row: 5  $\mu\text{m}$  printed catalyst squares with random oriented and aligned nanotube growth. Second row: 10  $\mu\text{m}$  line structures with exclusively well aligned growth.*

### 3.4 Raman spectroscopy

Micro-Raman spectroscopy was performed in order to investigate the vibrational properties of the synthesized carbon structures, which allows also to draw further conclusions about their crystallography or morphology. Fig. 3.16 compares the Raman spectra measured from carbon nanotubes grown at temperatures between 650 and 1000°C. All spectra show at least the two significant peaks at 1580  $\text{cm}^{-1}$  and at 1347  $\text{cm}^{-1}$ , which become broader at higher temperatures and overlap.

Crystalline graphite leads to a sharp vibration mode at 1580  $\text{cm}^{-1}$  [52] which is due to the presence of  $sp^2$  hybridized carbon domains and is named the first-order G band. The peak at approximately 1350  $\text{cm}^{-1}$  is considered to represent a more disordered structure and is labeled as the D (disordered) band [53]. Note that in a perfect graphite crystal the first-order vibrational mode of the D band is forbidden due to the selection rules. Decreasing particle size or bending of the lattice fringes may activate this band. As seen in Fig. 3.16,

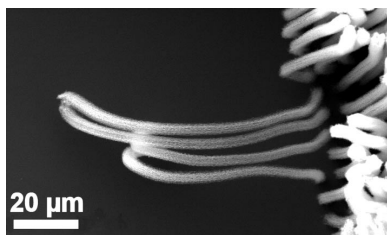


Figure 3.15: *SEM image showing the extended growth of nanotubes by addition of hydrogen to the CVD process: Bundles of multi-wall carbon nanotubes starting at printed catalyst squares.*

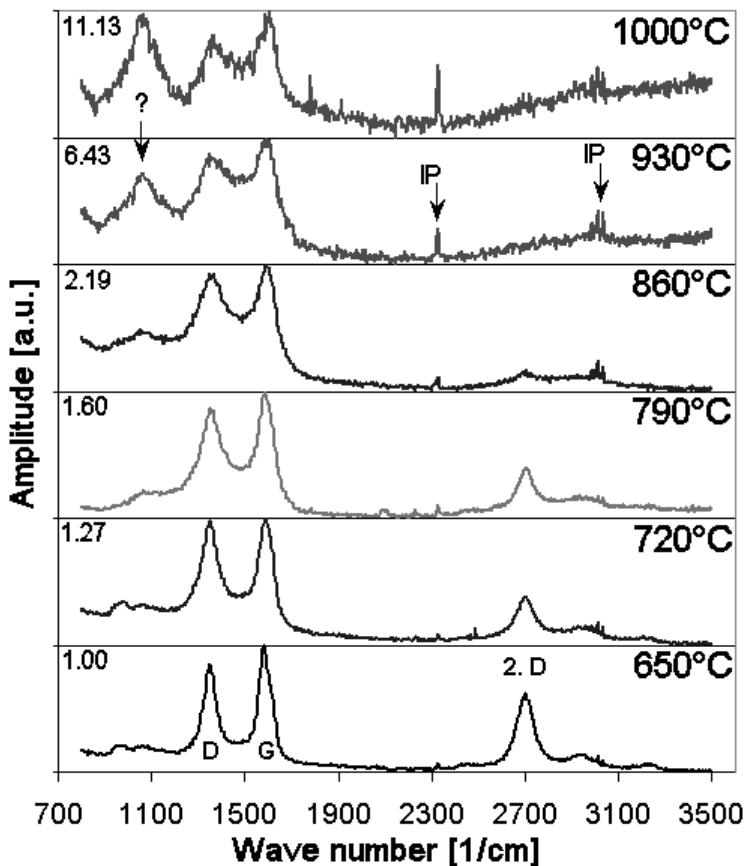


Figure 3.16: Micro-Raman spectroscopy of carbon nanotubes obtained at temperatures between  $650^{\circ}\text{C}$  and  $1000^{\circ}\text{C}$ . The peaks for the disordered (D) and the graphitic (G) carbon, the second order D-peak (2.D) and impurity peaks (IP) are visible. On the left side of the spectra the scaling factors are mentioned (relative to the spectrum at  $650^{\circ}\text{C}$ ). The spectra are normalized to the highest peak (G-peak) in each spectrum.

the second-order D peak (2.D) appears at approximately  $2700\text{ cm}^{-1}$  for nanotubes grown at lower temperatures. However, with increasing deposition temperature this peak disappears. The spectra are normalized to the highest peak in each spectrum (the G-peak). The

signal strength gets weaker for the structures deposited at higher temperatures, therefore the noise level becomes more and more visible in the spectra.

It is known (e.g. [54, 55]) that smaller particles as well as structural imperfections will broaden the first-order peaks from graphite. Therefore one can estimate the order of crystallinity in the material from the corresponding half-width (FWHM). An amorphous structure leads typically to a half-width (FWHM) of approximately  $200\text{ cm}^{-1}$  [55] as observed in the case of deposition at  $1000^\circ\text{C}$ . In the case of nanotubes deposited at  $650^\circ\text{C}$  sharp peaks (FWHM  $\sim 90\text{ cm}^{-1}$ ) reveal a much higher degree of crystalline perfection.

The catalytically grown carbon nanotubes can be characterized as a nano-crystalline but disordered graphite-like system where the disorder increases with the preparation temperature. This confirms qualitatively the results obtained by TEM. Unfortunately, Raman measurements could not clearly confirm that the high-temperature carbon structures consist of an amorphous and of a crystalline part as suggested by TEM.

Interestingly, the relative height of the peak at about  $1047\text{ cm}^{-1}$  increases with temperature. This peak could not yet be identified, but its broad shape indicates that it could probably originate from solid state phonons. This peak was detected already in earlier experiments on nitrogenated carbon nanotubes [56]. Some other peaks as indicated by arrows in Fig. 3.16 might be due to impurities. Stretch vibrations of  $\text{N}_2$  in the ambient air might cause the sharp peak at about  $2325\text{ cm}^{-1}$  [57].

### 3.5 Nanotube growth on glass

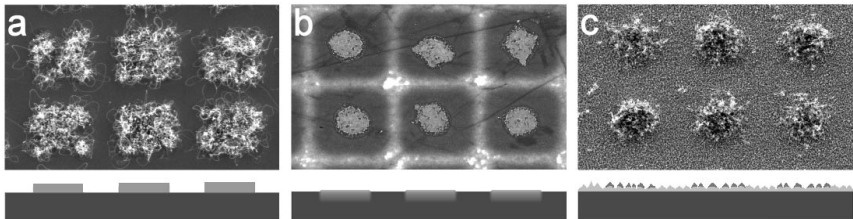


Figure 3.17: SEM images of CVD grown nanotubes on (a) silicon, (b) plain borosilicate glass and (c)  $\text{SnO}_2\text{:F}$ -covered borosilicate glass using a  $200\text{ mM}$  iron nitrate solution. Underneath each with a sketch of the assumed catalyst location: (a) on the silicon substrate, (b) diffused into the glass sample, and (c) on top of the  $\text{SnO}_2\text{:F}$  peaks.

For the sake of profitability the application of carbon nanotube films in field emission displays requires glass as substrate instead of silicon, but the borosilicate glass used for this purpose melts around  $660^\circ\text{C}$ . Most studies carried out on catalytic nanotube growth use however temperatures above  $700^\circ\text{C}$  [58, 59], which are too high to this end. Choi et al. report a plasma-enhanced CVD process at a temperature of  $550^\circ\text{C}$  [60], but the diameter of these nanotubes seems quite large and lacks uniformity. It could be demonstrated that

the growth of thin carbon nanotubes with just a few layers of carbon starts around 620°C, and that high quality films are obtained at 650°C. These nanotubes have uniform diameter and well-graphitized walls which is an indicator for good field emission properties. The temperature may even be further lowered by using other gas mixtures, by using other metallic or heterogeneous catalysts [61].

Up-to-now, nanotubes were deposited by CVD on glass only with the assistance of a plasma or a hot filament [62]. In Fig. 3.17 it is demonstrated that nanotubes can be grown on glass at temperatures below 650°C by simple thermal CVD. Borosilicate glass, both as received and coated with a conductive SnO<sub>2</sub>:F layer, were used as substrates.

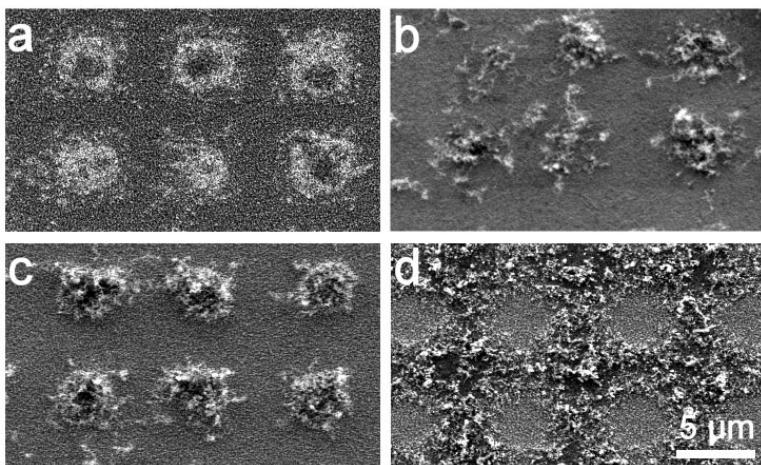


Figure 3.18: SEM images of the nanotube growth on SnO<sub>2</sub>:F-covered borosilicate glass using (a) 100 mM, (b) 150 mM, (c) 200 mM and (d) 300 mM iron nitrate solutions.

The growth was carried out at 630°C. Fig. 3.17a shows a standard sample obtained with a 200 mM Fe ink on silicon like described in Chapter 3.3.4. Fig. 3.17b shows the result of the CVD process using a glass sample printed with a 200 mM iron ink. The pattern is readily visible, but very little growth is observed (some amorphous or graphitic carbon material can be discerned). The results obtained on the SnO<sub>2</sub>:F-coated substrates are far more convincing (Fig. 3.17c): carbon nanotube "bunches" are present within the patterned areas and the growth is homogeneous over the whole surface. Note that as nanotube growth is not obtained below 630°C with our technique, the useful temperature range is quite limited. The conductive SnO<sub>2</sub>:F layer is thus not only useful to contact the nanotubes electrically, it seems also mandatory to obtain carbon nanotubes.

It is suspected that at the temperatures needed for the growth the metal diffuses rapidly into the glass substrate, which greatly diminishes its catalytic activity and active surface

(see the sketches under the SEM micrographs in Fig. 3.17). The  $\text{SnO}_2\text{:F}$  layer acts thus as both, support and diffusion barrier. The catalyst remains on the surface like in the case of silicon. The silicon substrate is protected against diffusion by its native oxide layer of some few nanometers.

As already described earlier in Chapter 3.3.4, an increase of the concentration leads to higher nanotube densities inside the patterns. The concentrations needed to obtain a comparable density are, however, higher by a factor of 2 in the case of glass. This makes the realization of high density films problematic, as concentrated inks are more difficult to print than diluted ones. As Fig. 3.18d shows for higher concentrations the growth on glass is not confined to the patterns, and there is a significant proportion of other forms of carbon in the deposit. A concentration of 200 mM seems therefore to be an optimum for the substrate and catalyst used.

### 3.6 Ferritin as catalyst for the nanotube growth

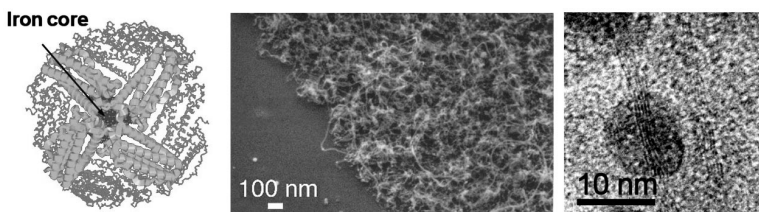


Figure 3.19: *Model of the ferritin complex, an SEM image of an area of the surface patterned by  $\mu\text{CP}$  using an aqueous ferritin/ $\text{Al}(\text{NO}_3)_3$  solution as catalyst and a TEM micrograph of a such a nanotube film on a  $\text{SiO}/\text{Cu}$  grid.*

As noted already by researchers studying carbon filaments in the 1970s, the diameter of CVD-grown structures is controlled to a large extent by the catalyst particle [63]. In order to obtain monodisperse nanotubes, one therefore needs to assemble or deliver well-defined catalyst particles onto a surface.

The mean size of the multi-wall nanotubes is difficult to control with the standard ink used before and the size distribution is relatively broad. This is due primarily to the fact that the catalyst particles are formed from a thin film or from ions in solution during annealing to the growth temperature (see Chapter 3.2), which makes the provision of small (under 10 nm) and monodisperse particles problematic. Here, a new approach is demonstrated which allows to obtain multi-wall carbon nanotubes of well-defined diameter by using the iron-containing cores of ferritin as catalyst.

Ferritin is a protein used by a variety of living organisms (among them humans) to assimilate nonhemoglobinian iron [64]. Mammalian ferritins are composed of 24 polypeptide chains that form a hollow shell and encapsulate a crystalline core of ferrihydrite

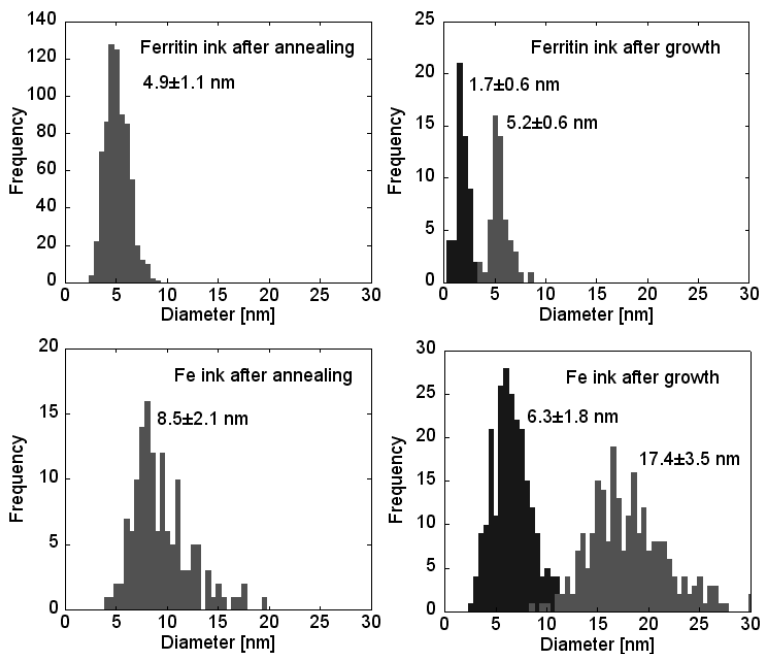


Figure 3.20: Diameter distribution as determined from TEM micrographs. On the left-hand side of the catalyst particles after annealing and on the right-hand side of the corresponding nanotubes after the CVD growth. The first row shows the results for a pristine solution of  $10 \mu\text{g/mL}$  ferritin and  $50 \text{ mM Al}(\text{NO}_3)_3 \cdot 9\text{H}_2\text{O}$  in  $\text{H}_2\text{O}$ , and the second row for a solution of  $15 \text{ mM Fe}(\text{NO}_3)_3 \cdot 9\text{H}_2\text{O}$  in ethanol.

$\text{FeOOH}$  (Fig. 3.19(left)). The ferritin used in the experiments (ferritin from horse spleen,  $0.15 \text{ mg/ml}$  in  $0.15 \text{ M NaCl}$ , Sigma) shows cores of  $5 \text{ nm}$  diameter that contain typically 3000 iron atoms. The idea is to use the sharp size distribution of natural ferritin to produce thin and monodisperse nanotubes, and to use  $\mu\text{CP}$  to deliver selectively the catalyst onto a silicon substrate.

The iron-containing cores of ferritin were used as catalyst for the growth of multi-wall carbon nanotubes by CVD at  $720^\circ\text{C}$ . The adjunction of  $\text{Al}(\text{NO}_3)_3 \cdot 9\text{H}_2\text{O}$  to ferritin has proven to be essential to prevent diffusion and coalescence of the catalyst particles and allows to produce monodisperse nanotubes with an outer diameter of  $5.2 \pm 0.6 \text{ nm}$ , which represents a significant improvement compared to conventional solutions. During the CVD process  $\text{Al}(\text{NO}_3)_3$  oxidizes to  $\text{Al}_2\text{O}_3$  which forms a stable matrix in which the iron

particles are embedded.

The size distributions of the catalyst particles and of the resulting nanotubes was examined for ferritin in Fig. 3.20(first row) and for a standard ethanolic solutions with  $\text{Fe}(\text{NO}_3)_3 \cdot 9\text{H}_2\text{O}$  in Fig. 3.20(second row). The ferritin cores show a mean diameter of 4.9 nm with a spread of 1.1 nm. The particles produced from the two inks based on  $\text{Fe}(\text{NO}_3)_3 \cdot 9\text{H}_2\text{O}$  show larger diameters and, more importantly, a significant proportion of large particles.

Maybe the most remarkable property of the ferritin catalyst is that the outer nanotube diameter matches closely the particle diameter. The ratio between outer nanotube diameter and particle size is close to 1, while it amounts to 2 for the  $\text{Fe}(\text{NO}_3)_3 \cdot 9\text{H}_2\text{O}$  catalysts. Note also that the spread in the diameters is far narrower for ferritin: even taking into account the fact that the mean nanotube diameter is smaller for ferritin as compared to the other catalysts, it is observed that the diameter dispersion is lower by a factor of 2. It was detected that the first nanotubes already appeared after 10 s, including the activation and growth time. This means that the activation time is much shorter than in the previous experiments, which may be due to the thinner layer of catalyst particles and the smaller size of those particles. With longer deposition periods also in these experiments more and more nanotubes appeared. At shorter deposition periods the diameter of the particles and the nanotubes was more homogeneous. The reduction of deposition time might limit the coalescence of the particles. The length of the obtained nanotubes was at least 1  $\mu\text{m}$  which then implies a growth rate of at least 100 nm/s.





# Chapter 4

## Growth mechanism

Based and inspired by the results in the preceding chapter a new model for the growth of carbon nanotubes is proposed. For this model the possibility is demonstrated to calculate the growth of carbon nanotubes by simple thermodynamics equations leading e.g. to the prediction of the growth velocity. Additionally, the heat generation and distribution and the carbon migration in the nanotubes was simulated by means of the finite element method. Furthermore, a mechanism for the cessation of the growth is discussed.

### 4.1 Supposed growth mechanism

In the following the results are discussed in the light of the most probable growth mechanism for carbon nanotubes under the applied experimental conditions. It is supposed that the mechanism of the catalytic growth of carbon nanotubes is similar to the one described by Kanzow et al. [65]. Acetylene is thermally stable at temperatures below 800°C and can be dissociated only catalytically, in the case discussed here, on the small metal (oxide) particles delivered to the substrate by microcontact printing (Fig. 4.1). In a first period the acetylene reduces the metal oxide grains to pure metal:  $\text{Fe}_2\text{O}_3 + 3\text{C}_2\text{H}_2 \rightarrow 2\text{Fe} + 6\text{C} + 3\text{H}_2\text{O}$ , whereas the iron remains on the substrate surface as grain, the carbon diffuses into the metal and the water evaporates. The further catalytic dissociation of acetylene takes presumably place at facets of well-defined crystallographic orientation [66], the resulting hydrogen  $\text{H}_2$  is removed by the gas flow whereas the carbon is dissolved in and diffuses into the particle. For unsaturated hydrocarbons this process is highly exothermic. When the particle is saturated with carbon, the carbon leaves the particle at another, less reactive surface of the particle, which is an endothermic process. The resulting density gradient of carbon dissolved in the particle supports the diffusion of carbon through the particle. In order to avoid dangling bonds, the carbon atoms assemble in an  $sp^2$  structure at a less reactive facet of the particle, which leads to the formation of a nanotube.

The simple model presented in Fig. 4.1 describes the growth with a particle at the top of the nanotube or at the bottom. In principle both cases work in the same way, but in the second one the particle adheres more to the substrate surface than in the first case. There must be free particle surfaces that are exposed to the gas for the growth to proceed. In the second case the acetylene diffuses from the sides into the particle and the nanotube is

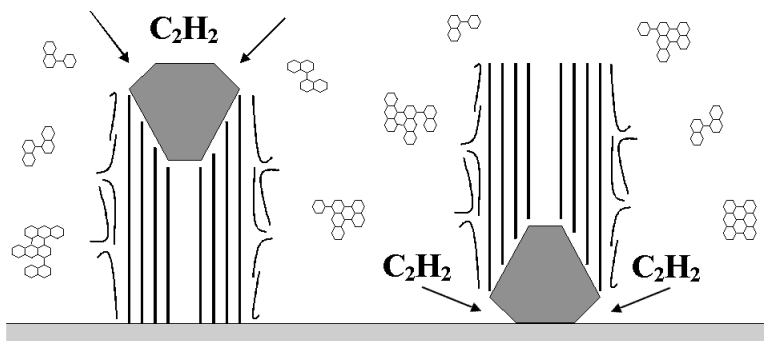


Figure 4.1: *Model for the suggested growth mechanism of catalytically grown carbon nanotubes (based on considerations by Kanzow et al. [65]).*

constructed from the bottom up, whereas in the first case the gas diffuses from the sides and from the top into the particle. The second case seems to be the favored mechanism in the accomplished experiments as typically 90 % of the tubes have closed tips without a catalytic particle at the top.

At first glance it is difficult to understand in the frame of the above model why the diameter of the structures increases with temperatures above 800°C. At around 800°C, acetylene starts to dissociate spontaneously, and the reaction gas contains therefore a significant fraction of free carbon, which will form larger aggregates in order to avoid dangling bonds. These carbon flakes, once formed, are carried with the gas flow and may be deposited on the substrate as well as on the surface of the structures (see Ref. [67]). At temperatures above 800°C the following scenario is therefore probable: as is the case at lower temperatures, carbon nanotubes of small diameter are formed over the catalyst-patterned areas after an activation period, and the growth itself takes place very rapidly. In addition, the flakes formed in the gas phase condensate on the substrate and on the formed nanotubes, adding a polycrystalline outer shell over the graphitic inner core. The structures get thicker with temperature because the proportion between dissociated and molecular acetylene in the gas phase increases.

This explanation is supported by the TEM images and the Raman spectroscopy, which confirmed the polycrystalline character of these structures (Chapter 3). In fact, while SEM suggests an amorphous carbon structure on the surface of the grown tubes, TEM reveals a crystalline core structure that is surrounded by a polycrystalline shell (Fig. 3.12b and c). Raman spectroscopy showed that there is a continuous increase of the polycrystalline fraction in the structures with increasing temperature which corroborates the findings. The outer shell becomes thicker with higher temperature starting from the thinnest structures at a temperature of 650°C.

It was noted in Fig. 3.13 that the nanotube growth did not begin immediately after the

introduction of the hydrocarbon gas in the reactor, but that some carborized spots appear before the rapid nanotube growth. This suggests that a certain quantity of carbon must be dissolved in and diffuse through the particle before the nanotube growth can start. Also the reduction of the metal oxide grains to pure metal takes some time.

Only few nanotubes were found using nickel and cobalt as catalysts, whereas other groups successfully used nickel [60,62], nickel-cobalt [59] or cobalt [58]. This may be due to several facts. First, the catalyst is usually deposited by thermal evaporation or sputtering from a pure metal source. Furthermore, the catalyst is often reduced before the growth or the growth itself is carried out in a reducing atmosphere to ensure that the catalyst remains metallic [68]. In the experiments considered here however, the catalyst is dissolved in a solution. The printed metal catalyst consists of a gel-like material that forms a metal nitrate/oxide film after annealing (Chapter 3.2) and no explicit step is taken to reduce the catalyst. Further on, the used iron salt contains Fe(III) ions whereas the ions in the nickel and the cobalt salt are just divalent. This may significantly change the behavior of the catalyst. And here, thermal CVD is used, in contrast to the Hot Filament or Plasma Enhanced CVD used in other studies. The hot filament and the plasma provides an additional possibility for the dissociation of the hydrocarbon and may decisively influence the reaction kinetics.

## 4.2 Calculations and simulations for the growth mechanism

The experimental progress in carbon nanotube research makes it necessary to understand the growth (mechanism) also theoretically. Here, the possibility to calculate and simulate the CVD growth of carbon nanotubes by means of classical methods is demonstrated. Mainly thermodynamic equations and considerations and a free software [69] to solve differential equations by the finite element method (FEM) are used. It was found that the growth is mainly concentration driven and not thermally. Whereas the deposition temperature indeed plays role in terms of diffusion. One can also conclude some values of the catalytic reactions of acetylene on iron facets. Additionally some equations are gained which describe the growth and the catalytic reactions on the facets of the involved catalyst particle. Thus one can draw some conclusions and provide predictions for the growth. The calculations and simulations are demonstrated here exemplarily for the nanotube growth at 650°C using the iron ink but may easily be adapted to different conditions.

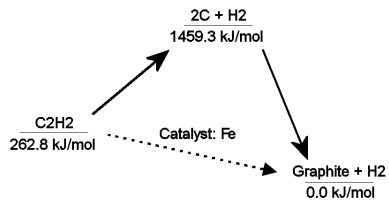


Figure 4.2: *Enthalpies of the decomposition of acetylene at 650°C:  $C_2H_2 \rightarrow 2C_{gas} + H_2 \rightarrow 2C_{graphite} + H_2$  and catalysis by iron.*

## 4.2.1 Calculations

### Preconditions

The catalytic reaction  $C_2H_2 \xrightarrow{Fe} 2C_{\text{graphitic}} + H_2$  is highly exothermic and enthalpy driven. Fig. 4.2 shows that this reaction frees at  $650^\circ\text{C}$  an energy of about  $262.8 \text{ kJ/mol}$  ( $226.7 \text{ kJ/mol}$  at  $25^\circ\text{C}$ ) [70]. The two carbon atoms diffuse at a reactive facet into the catalyst particle and the hydrogen is taken away by the gas flow. The carbon will diffuse through the particle to another less reactive facet where the carbon concentration is smaller and the temperature is lower. Similar models were suggested by different authors [65, 71, 72]. In an extensive study on catalytic particles on top of carbon nanotubes prepared by CO decomposition Audier et al. [66] found that there are relations between the crystallographic structure of the catalyst particles and the attached nanotubes. In the case of a bcc structure of the catalyst particle, the particle is a single crystal with a  $[100]$  axis parallel to the axis of the nanotube, and the basal facets of the truncated cone, which appeared free of carbon, are  $(100)$  facets. Anderson et al. [73] determined theoretically different activities of decomposition of acetylene on iron facets. And Hung et al. [74] mention that with Fe(bcc) a complete decomposition of acetylene takes place at the Fe(100) facets, whereas at the Fe(110) and Fe(111) facets molecular desorption was observed. This may be due to the different surface roughnesses.

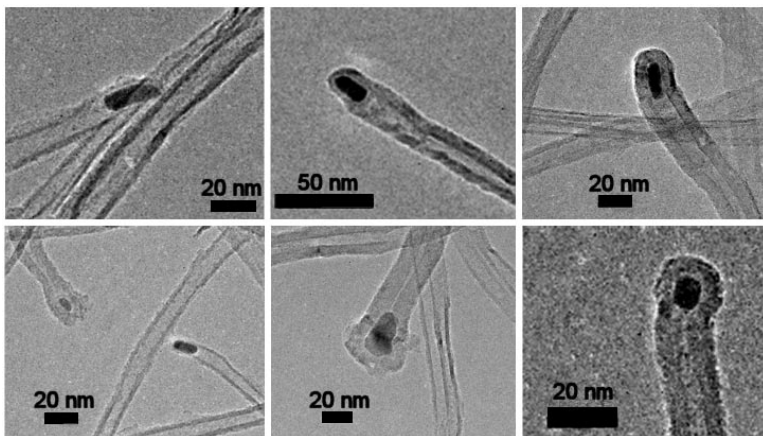


Figure 4.3: *Examples for catalyst particles at the top of carbon nanotubes (TEM micrographs).*

The crystalline character of the catalyst particles used for the synthesis of nanotubes in the frame of this work was demonstrated in Chapter 3.2 by electron diffraction measurements and TEM real-space images. At temperatures up to  $1000^\circ\text{C}$  the catalyst particles are

solid but a high material mobility and migration was observed and video taped by TEM imaging during in situ heating of the catalyst.

In order to support the presented assumptions for the mechanism and the geometries of the growth model in Fig. 4.3 are shown some particles which were found at the top of the nanotubes. That the diameter is determined by the size of the catalyst particle as suggested by Fig. 4.3 was already proven in Chapter 3.6.

### Heat diffusion

In order to calculate the heat and the particle diffusion through a catalyst grain we start with Fourier's law

$$j_q = -\lambda \nabla T \quad (4.1)$$

including it into the Equation of Continuity

$$c_q \rho \frac{\partial T}{\partial t} + \nabla j_q = 0 \quad (4.2)$$

we get the Heat Equation:

$$\hookrightarrow c_q \rho \frac{\partial T}{\partial t} - \lambda \Delta T = 0 \quad (4.3)$$

As boundary condition for constant heat flow through a facet we have

$$\nabla T = -j_q / \lambda \big|_{\text{facet}} \quad (4.4)$$

and for a constant temperature at a facet

$$T = T_b \big|_{\text{facet}} \quad (4.5)$$

We can rewrite Eq. 4.3 as:

$$\frac{\partial T}{\partial t} - \frac{\lambda}{c_q \rho} \Delta T = 0 \quad (4.6)$$

and abbreviate as:

$$\frac{\partial T}{\partial t} - \kappa \Delta T = 0 \quad \text{with} \quad \kappa = \frac{\lambda}{c_q \rho} \quad (4.7)$$

The constants are:

$\lambda$  - heat conductivity / here (from [75]):  $\lambda[\text{Fe}] = 38.0 \frac{\text{W}}{\text{m}\cdot\text{K}}$  at 900 K

$c_q$  - heat capacity / here (from [70]):  $c_q[\text{Fe}] = 760.1 \frac{\text{J}}{\text{kg}\cdot\text{K}}$  at 923 K

$\rho$  - density / here (from [70]):  $\rho[\text{Fe}] = 7860.0 \frac{\text{kg}}{\text{m}^3}$  at 293 K

$$\hookrightarrow \kappa[\text{Fe}] = 6.360 \cdot 10^{-6} \frac{\text{m}^2}{\text{s}} \quad (4.8)$$

### Dimensionless calculation

In order to improve the precision and to simplify the simulations with the FEM software [69] the equations and the involved constants are converted to a dimensionless system.

$$\text{With Eq. 4.7 and: } t^* = \frac{t}{t_o}, \quad \vec{x}^* = \frac{\vec{x}}{\vec{x}_o} \Rightarrow d^2 \vec{x}^* = \frac{d^2 \vec{x}}{\vec{x}_o^2}, \quad T^* = \frac{T}{T_o} \quad (4.9)$$

$$\hookrightarrow \frac{T_o}{t_o} \cdot \frac{\partial T^*}{\partial t^*} - \kappa \frac{T_o}{\vec{x}_o^2} \Delta T^* = 0 \quad (4.10)$$

$$\hookrightarrow \frac{\partial T^*}{\partial t^*} - \kappa \frac{t_o}{\vec{x}_o^2} \Delta T^* = 0 \quad (4.11)$$

$$\hookrightarrow \frac{\partial T^*}{\partial t^*} - \kappa^* \Delta T^* = 0 \quad \text{with} \quad \kappa^* = \kappa \cdot \frac{t_o}{\vec{x}_o^2} \quad (4.12)$$

Defining  $\kappa^* \stackrel{!}{=} 1$  let us calculate the *time parameter*  $t_o = \frac{\vec{x}_o^2}{\kappa}$

$$\text{here: } x_o = 1 \text{ nm} = 10^{-9} \text{ m}, \quad \kappa[\text{Fe}] = 6.360 \cdot 10^{-6} \frac{\text{m}^2}{\text{s}} \quad (4.13)$$

$$\hookrightarrow t_o = 1.572 \cdot 10^{-13} \text{ s} \quad (4.14)$$

From Eq. 4.4 we get the heat flow normal to a facet

$$\frac{\partial T}{\partial \vec{n}} = -\frac{1}{\lambda} \cdot j_q \quad (4.15)$$

$$\frac{T_o}{x_o} \cdot \frac{\partial T^*}{\partial \vec{n}^*} = -\frac{1}{\lambda} \cdot j_q \quad (4.16)$$

$$\hookrightarrow \frac{\partial T^*}{\partial \vec{n}^*} = -\frac{x_o}{T_o \cdot \lambda} \cdot j_q = -j_q^* \quad (4.17)$$

Defining  $j_q^* = \frac{x_o}{T_o \cdot \lambda} j_q \stackrel{!}{=} 1$  let us calculate the *temperature parameter*

$$T_o = \frac{x_o}{\lambda} \cdot j_q \stackrel{\text{here}}{=} 2.632 \cdot 10^{-11} \frac{\text{m}^2 \cdot \text{s} \cdot \text{K}}{\text{J}} \cdot j_q \quad (4.18)$$

### Particle diffusion

The heat flow will be calculated with the particle flow:

$$j_p = -D \nabla c \quad \text{Fick's First Law} \quad (4.19)$$

where  $D$  - diffusion constant,  $c$  - concentration and  $D$  is given by

$$D = D_o \cdot \exp[-E_a/kT] \quad \text{Arrhenius equation} \quad (4.20)$$

where  $E_a$  - activation energy,  $D_o$  - diffusion factor

Here (from [75]): C in Fe(bcc)

$$D_o = 2.2 \frac{\text{cm}^2}{\text{s}} = 2.2 \cdot 10^{-4} \frac{\text{m}^2}{\text{s}}, E_a = 2.035 \cdot 10^{-19} \text{ J} \quad (4.21)$$

$$\hookrightarrow D = 2.53 \cdot 10^{-11} \frac{\text{m}^2}{\text{s}} \text{ at } 923 \text{ K} \stackrel{\Delta}{=} 650^\circ\text{C} \text{ (experiment)}$$

respectively (from [75]): C in Fe(fcc)

$$D_o = 0.15 \frac{\text{cm}^2}{\text{s}} = 1.5 \cdot 10^{-5} \frac{\text{m}^2}{\text{s}}, E_a = 2.362 \cdot 10^{-19} \text{ J} \quad (4.22)$$

$$\hookrightarrow D = 1.33 \cdot 10^{-13} \frac{\text{m}^2}{\text{s}} \text{ at } 923 \text{ K} \stackrel{\Delta}{=} 650^\circ\text{C}$$

Following the iron-carbon-diagram the saturation of carbon in iron without forming any chemical bonds (e.g. iron carbide  $\text{Fe}_3\text{C}$ ) is 65 ppm(weight) at  $650^\circ\text{C}$  [76]. This determines the concentration gradient  $\nabla c$ .

$$\text{With Eq. 4.19 and: } |\nabla c| = \frac{65 \text{ ppm}}{d_{\text{diff}}} \cdot \frac{\text{molweight}[\text{Fe}]}{\text{molweight}[\text{C}]} \cdot \frac{1}{\text{molvolume}[\text{Fe}]} \quad (4.23)$$

diffusion distance  $d_{\text{diff}}$  (e.g.  $d_{\text{diff}} \simeq \frac{1}{2}d_{\text{particle}}$ )

$\text{molweight}[\text{Fe}] = 55.8 \text{ g/mol}$ ,  $\text{molweight}[\text{C}] = 12.0 \text{ g/mol}$

$\text{molvolume}[\text{Fe}] = 7.09 \text{ cm}^3/\text{mol} = 7.09 \cdot 10^{-6} \text{ m}^3/\text{mol}$

$$\hookrightarrow |\nabla c| = 42.63 \frac{\text{mol}}{\text{m}^3} \cdot \frac{1}{d_{\text{diff}}} \quad (4.24)$$

With Eq. 4.19 and 4.21:

$$j_{\text{p,mol}}(\text{bcc}) = 1.079 \cdot 10^{-9} \frac{\text{mol}}{\text{m} \cdot \text{s}} \cdot \frac{1}{d_{\text{diff}}} \quad (4.25)$$

$$j_{\text{p,mol}}(\text{fcc}) = 5.67 \cdot 10^{-12} \frac{\text{mol}}{\text{m} \cdot \text{s}} \cdot \frac{1}{d_{\text{diff}}}$$

$$\hookrightarrow j_{\text{p,N}}(\text{bcc}) = 6.499 \cdot 10^{14} \frac{\text{particle}}{\text{m} \cdot \text{s}} \cdot \frac{1}{d_{\text{diff}}}$$

$$\hookrightarrow j_{\text{p,N}}(\text{fcc}) = 3.415 \cdot 10^{12} \frac{\text{particle}}{\text{m} \cdot \text{s}} \cdot \frac{1}{d_{\text{diff}}}$$

Since  $C_2H_2 \Rightarrow \underline{2C} + H_2$ :

$$j_q = j_p \cdot 262.8 \frac{\text{kJ}}{\text{mol}} \cdot \frac{1}{\underline{2}} \quad (4.26)$$

$$j_q(\text{bcc}) = 1.418 \cdot 10^{-4} \frac{\text{J}}{\text{m} \cdot \text{s}} \cdot \frac{1}{d_{\text{diff}}}$$

$$j_q(\text{fcc}) = 7.45 \cdot 10^{-7} \frac{\text{J}}{\text{m} \cdot \text{s}} \cdot \frac{1}{d_{\text{diff}}}$$

With (4.18) and (4.26):

$$\underline{\underline{T_o(\text{bcc}) = 3.732 \cdot 10^{-15} \text{ m} \cdot \text{K} \cdot \frac{1}{d_{\text{diff}}}}} \quad (4.27)$$

$$\underline{\underline{T_o(\text{fcc}) = 1.961 \cdot 10^{-17} \text{ m} \cdot \text{K} \cdot \frac{1}{d_{\text{diff}}}}}$$

$T_o$  is the correction factor for the temperature (Eq. 4.18). The obtained simulation values must be multiplied by this factor to get the actual temperature increase.

From the experiments we can define a standard nanotube: a hollow cylinder with a length of  $l_{\text{nt}} = 5 \mu\text{m}$ , an inner diameter of  $d_{\text{in}} = 10 \text{ nm}$  and an outer diameter of  $d_{\text{out}} = 20 \text{ nm} = d_{\text{particle}}$  (compare with Fig. 3.11, 3.12a and 4.3). It has the volume of

$$V_{\text{nt}} = \frac{\pi \cdot l_{\text{nt}}}{4} (d_{\text{out}}^2 - d_{\text{in}}^2) = 1.178 \cdot 10^{-21} \text{ m}^3 \quad (4.28)$$

$$\hat{=} 2.572 \cdot 10^{-16} \text{ mol} \hat{=} 3.087 \cdot 10^{-18} \text{ kg}$$

$$\text{with } V_{\text{mol}}[\text{C}] = 4.58 \frac{\text{cm}^3}{\text{mol}} = 4.58 \cdot 10^{-6} \frac{\text{m}^3}{\text{mol}} \quad (4.29)$$

$$\text{and } m_{\text{mol}}[\text{C}] = 12.0 \text{ g} = 0.012 \text{ kg}$$

Then the totally transformed thermal energy would be

$$\hookrightarrow \Delta Q_{\text{total}} = 262.8 \frac{\text{kJ}}{\text{mol}} \cdot 2.572 \cdot 10^{-16} \text{ mol} \cdot \frac{1}{2} = 3.38 \cdot 10^{-11} \text{ J} \quad (4.30)$$

And if all the heat was accumulated just in the catalyst particle and the nanotube, without a transfer to another reservoir, the nanotube would be heated up by

$$\Delta T = \frac{\Delta Q_{\text{total}}}{c_q[\text{Fe}] \cdot m[\text{Fe}] + c_q[\text{C}] \cdot m[\text{C}]} = 6834.17 \text{ K} \quad (4.31)$$



$$\begin{aligned}
c_q[\text{Fe}] &= 449,0 \frac{\text{J}}{\text{kg}\cdot\text{K}} \\
m[\text{Fe}] &= \frac{\pi}{6} \cdot (20 \text{ nm})^3 \cdot \rho[\text{Fe}] = 3.292 \cdot 10^{-20} \text{ kg} \\
&\text{(e.g. sphere as catalyst particle, diameter: 20 nm)} \\
c_q[\text{C}] &= 710,0 \frac{\text{J}}{\text{kg}\cdot\text{K}} \\
m[\text{C}] &= 6,945 \cdot 10^{-18} \text{ kg}
\end{aligned}$$

This temperature rise seems to be very much. But one have to bear in mind that here an isolated nanotube is considered, without any contact to the environment. The actual temperature rise will be much lower due to an energy transfer to the substrate as discussed later.

### Further calculations

It is possible to calculate the growth time for this nanotube. With Eq. 4.25 and the number of mol of the nanotube ( $2.572 \cdot 10^{-16}$  mol):

$$t_{\text{growth}} = \frac{2.572 \cdot 10^{-16} \text{ mol}}{j_p \cdot \frac{1}{2} A_{\text{particle}}} \quad (4.32)$$

$$\underline{\underline{t_{\text{growth}}(\text{bcc}) = 3.794 \text{ s}}}$$

$$t_{\text{growth}}(\text{fcc}) = 721.97 \text{ s} = 12.03 \text{ min}$$

$$\hookrightarrow v_{\text{growth}} = \frac{l_{\text{nt}}}{t_{\text{growth}}}$$

$$\hookrightarrow \underline{\underline{v_{\text{growth}}(\text{bcc}) = 1.318 \frac{\mu\text{m}}{\text{s}}}}$$

$$\hookrightarrow v_{\text{growth}}(\text{fcc}) = 6.925 \frac{\text{nm}}{\text{s}}$$

With the lower surface of the particle (nanotube creation)  $A_{\text{creation}} \simeq \frac{1}{2} A_{\text{particle}} = \frac{1}{2} \cdot \pi \cdot d_{\text{particle}}^2 = 6.283 \cdot 10^{-16} \text{ m}^2$  (sphere) and due to Eq. 4.25 with  $d_{\text{diff}} = 10 \text{ nm}$  :

$$j_p(\text{bcc}) = 0.1079 \frac{\text{mol}}{\text{m}^2 \cdot \text{s}} = 6.498 \cdot 10^{22} \frac{\text{particle}}{\text{m}^2 \cdot \text{s}} \quad (4.33)$$

$$j_p(\text{fcc}) = 5.67 \cdot 10^{-4} \frac{\text{mol}}{\text{m}^2 \cdot \text{s}} = 3.415 \cdot 10^{20} \frac{\text{particle}}{\text{m}^2 \cdot \text{s}}$$

But the nanotube creation surface  $A_{\text{creation}}$  may differ from the one considered here.

In the following we regard just Fe(bcc) because a growth time of some few seconds seems to be more realistic. Then the time for one carbon atom to cross the iron particle is about

$$t_{\text{cross}}(\text{bcc}) = \frac{d_{\text{diff}}^2}{3 \cdot D} = 1.318 \cdot 10^{-6} \text{ s} \quad (4.34)$$

with the crossed distance of about 10 nm and  $D(\text{bcc}) = 2.53 \cdot 10^{-11} \text{ m}^2/\text{s}$ .  $t_{\text{cross}}$  is negligible compared with  $t_{\text{growth}}$ .

With Eq. 4.19, 4.28 and 4.29 Eq. 4.32 can also be written as

$$t_{\text{growth}} = \frac{\pi \cdot l_{\text{nt}}}{4} (d_{\text{out}}^2 - d_{\text{in}}^2) \cdot \frac{1}{V_{\text{mol}}[\text{C}]} \cdot \frac{1}{D \cdot |\nabla c|} \cdot \frac{1}{\frac{1}{2} \cdot \pi \cdot d_{\text{particle}}^2} \quad (4.35)$$

$$= \frac{l_{\text{nt}} \cdot (d_{\text{out}}^2 - d_{\text{in}}^2)}{2 \cdot V_{\text{mol}}[\text{C}] \cdot d_{\text{particle}}^2 \cdot D \cdot |\nabla c|} \quad (4.36)$$

$$\stackrel{(4.20)}{=} \frac{l_{\text{nt}} \cdot (d_{\text{out}}^2 - d_{\text{in}}^2)}{2 \cdot V_{\text{mol}}[\text{C}] \cdot d_{\text{particle}}^2 \cdot D_o \cdot |\nabla c|} \cdot \exp[E_a/kT] \quad (4.37)$$

Since all values but the diffusion coefficient  $D$  are constant with temperature  $t_{\text{growth}}$  is proportional to  $\exp[E_a/kT]$  which is a strong decay with temperature.

With Eq. 4.24, the constant  $V_{\text{mol}}[\text{C}]$  and  $d_{\text{diff}} \simeq \frac{1}{2} d_{\text{particle}}$ :

$$t_{\text{growth}} = 1280.44 \cdot \frac{l_{\text{nt}} \cdot (d_{\text{out}}^2 - d_{\text{in}}^2)}{d_{\text{particle}} \cdot D} \quad (4.38)$$

And with  $D(\text{bcc})$ :

$$t_{\text{growth}} = 5.061 \cdot 10^{13} \frac{\text{s}}{\text{m}^2} \cdot \frac{l_{\text{nt}} \cdot (d_{\text{out}}^2 - d_{\text{in}}^2)}{d_{\text{particle}}} \quad (4.39)$$

The growth velocity  $v_{\text{growth}} = l_{\text{nt}}/t_{\text{growth}}$  turns then out to be:

$$v_{\text{growth}} = \frac{2 \cdot V_{\text{mol}}[\text{C}] \cdot d_{\text{particle}}^2 \cdot D_o \cdot |\nabla c|}{(d_{\text{out}}^2 - d_{\text{in}}^2)} \cdot \exp[-E_a/kT] \quad (4.40)$$

With  $d_{\text{nt}} = d_{\text{particle}} = d_{\text{out}} = 2 \cdot d_{\text{in}} = 2 \cdot d_{\text{diff}}$ :

$$v_{\text{growth}} = 2.291 \cdot 10^{-7} \frac{\text{m}^2}{\text{s}} \cdot \frac{1}{d_{\text{nt}}} \cdot \exp[-E_a/kT] \quad (4.41)$$

The growth velocity is proportional to  $\exp[-E_a/kT]$  (which is a strong increasing temperature dependence) and to  $1/d_{\text{nt}}$ . This behavior is demonstrated in Fig. 4.4.

As the particle size is correlated with the tube diameter like  $d_{\text{particle}} \simeq d_{\text{out}}$ ,  $d_{\text{particle}} \simeq 2 \cdot d_{\text{in}}$ , and  $d_{\text{particle}} \simeq 2 \cdot d_{\text{diff}}$ ,  $v_{\text{growth}}$  is proportional to  $1/d_{\text{particle}}$ . This is similar to the result

Baker [71] found experimentally for carbon filaments  $v_{\text{growth}} \propto 1/\sqrt{d_{\text{particle}}}$ .

In order to estimate some values of the catalytic reactions, we start with:

$$v_{\text{growth,N}} = j_{\text{p,N}} \cdot A_{\text{creation}} = j_{\text{p,N}} \cdot \frac{1}{2} A_{\text{particle}} = \quad (4.42)$$

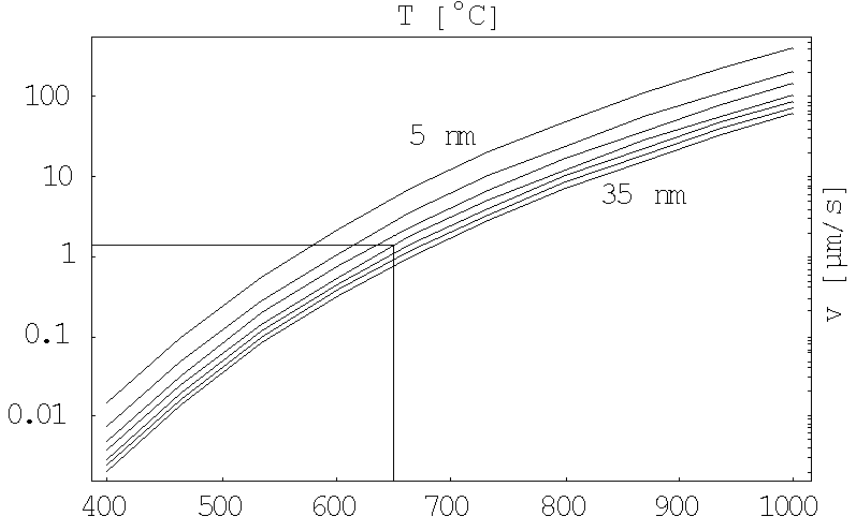


Figure 4.4: Calculated growth velocity  $v_{\text{growth}}$  as function of deposition temperature (400-1000°C) and nanotube diameter (5-35 nm). The marker indicates the explicitly calculated value for the standard tube ( $v_{\text{growth}}(d_{\text{nt}} = 20 \text{ nm}) = 1.318 \mu\text{m/s}$  at 650°C).

$$(4.25) \quad 6.499 \cdot 10^{14} \frac{\text{particle}}{\text{m} \cdot \text{s}} \cdot \frac{1}{d_{\text{diff}}} \cdot \frac{1}{2} A_{\text{particle}}$$

$A_{\text{creation}}$  - Surface of nanotube generation

For the standard nanotube this is  $v_{\text{growth,N}} = 4.083 \cdot 10^7$  particle/s. This may also be the rate of at the facets converted carbon atoms. Thus the reaction rate is  $v_{\text{reaction}} = \frac{1}{2} \cdot v_{\text{growth,N}} = 2.042 \cdot 10^7$  reaction/s ( $C_2H_2 \Rightarrow \underline{\underline{2C}} + H_2$ ). The reaction flow is then  $j_{\text{reaction}} = v_{\text{reaction}} / (\frac{1}{2} A_{\text{particle}}) = \frac{1}{2} \cdot j_{\text{p,N}} = 3.25 \cdot 10^{22}$  reaction/(m<sup>2</sup> · s).

The number of reaction centers RC on the surface (the decomposition of one molecule takes place at several surface atoms) is

$$N_{\text{rc}} = \frac{A_{\text{reaction}}}{A_{\text{rc}}} \quad (4.43)$$

$A_{\text{reaction}}$  - complete surface where catalytic reactions take place

$A_{\text{rc}}$  - surface of one reaction center

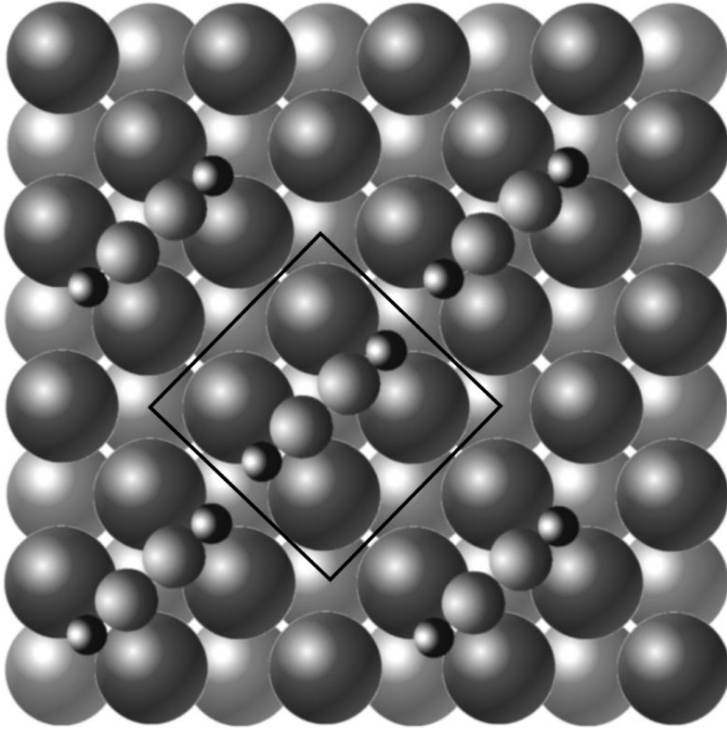


Figure 4.5: Assumed adsorption of acetylene on bcc iron Fe(100) (top view, according to [74]).

According to [74] the decomposition of acetylene takes place at four iron atoms on the (bcc) surface (Fig. 4.5). The lattice constant for Fe(bcc) is  $a = 2.866 \text{ \AA}$  [75]. Thus, in our case (bcc), the reaction center has a surface of  $A_{\text{rc}} = (2a_{\text{bcc}})^2 = 3.286 \cdot 10^{-19} \text{ m}^2$  (square on the surface, Fig. 4.5). With the reaction surface  $A_{\text{reaction}} = \frac{1}{2}A_{\text{particle}} = 6.283 \cdot 10^{-16} \text{ m}^2$ , the number of reaction centers on the surface is then  $N_{\text{rc}} = 1912$ . And with  $\nu_{\text{reaction}} = 2.042 \cdot 10^7 \text{ reaction/s}$  we can calculate the reaction rate  $\nu_{\text{reaction}}$ :

$$\nu_{\text{reaction}} = \frac{\nu_{\text{reaction}}}{N_{\text{rc}}} = 10680 \frac{\text{reaction}}{\text{RC} \cdot \text{s}} \quad (4.44)$$

$$\hookrightarrow \tau = \frac{1}{\nu_{\text{reaction}}} = 93.6 \mu\text{s} \quad (4.45)$$

Every 93.6  $\mu\text{s}$  a reaction takes place. I.e. the reaction center RC is occupied for about 93.6  $\mu\text{s}$  per reaction. But the actual reaction time will be much shorter (pico-seconds). The relative long time may be due to carbon atoms which do not diffuse immediately into the bulk and rest on the surface for awhile or a relative low sticking coefficient of acetylene on iron.

The impact rate of gas particles on a surface is

$$j_{\text{impact}} = \frac{p}{\sqrt{2\pi mkT}} \quad (4.46)$$

whereas  $m$  is the mass of the gas molecule (here:  $m[\text{C}_2\text{H}_2] = 4.324 \cdot 10^{-26}$  kg,  $T = 923$  K) and  $p$  the pressure. At e.g. 20 mbar = 2000 Pa (standard experiment) we have then a impact rate of  $j_{\text{impact}} = 3.4 \cdot 10^{25}$  hits/( $\text{m}^2 \cdot \text{s}$ ). Compared with the reaction rate  $j_{\text{reaction}} = 3.25 \cdot 10^{22}$  reaction/( $\text{m}^2 \cdot \text{s}$ ) this means that the surface is always saturated. A reduction of the growth velocity should then occur at pressures under  $p = j_{\text{reaction}} \cdot \sqrt{2\pi mkT} = 1.913$  Pa =  $1.913 \cdot 10^{-2}$  mbar. If there are such effects already at higher pressures, then this is due to the fact that not all of the on the surface appearing molecules also really adsorbe (sticking coefficient  $\gamma$ ). The reduction of the growth velocity could be used to control the length of the nanotubes by reducing the pressure and stopping the CVD process before they reach the final length.

## 4.2.2 Simulations

In order to simulate the distribution of temperature and carbon concentration in the catalyst particle, two-dimensional finite element method simulations (FEM) have been employed. Furthermore, the heat transfer in the whole system (catalyst particle - carbon nanotube - silicon substrate) is studied. For this purpose the free available FEM software FreeFEM+ [69] was used.

For the simulation of the heat transfer resp. the temperature distribution  $\frac{\partial T}{\partial t} - \kappa \Delta T = 0$  was used in the time dependent case and  $-\kappa \Delta T = 0$  in the stationary case. The boundary conditions are  $\nabla T = -j_q/\lambda|_{\text{facet}}$  for a constant flow into the facet and  $T = T_b|_{\text{facet}}$  for a constant temperature at the facet. For the boundary conditions a heat penetration of  $j_q$  at the horizontal and vertical facets of a model catalyst particle (bcc(100)-like facets, see Chapter 4.2.1) and constant temperature of  $T_b = 0$  K at the three outer sides of the silicon substrate (Fig. 4.6 and 4.7) was assumed. A distribution of temperature rise is then obtained in the defined geometry. The shape of the model particle is inspired by the particles found at the top of nanotubes (e.g. Fig. 3.11 and 4.3). The catalyst particle is supposed to be a cube-like particle and twice as long as in diameter. It can be on top of the nanotube (pushed up by the nanotube) or sticking to the substrate surface (while pushing up the nanotube). The silicon substrate is 10  $\mu\text{m}$  long and 5  $\mu\text{m}$  high, which seemed to be sufficient (a further enlargement did not cause a change in temperature).

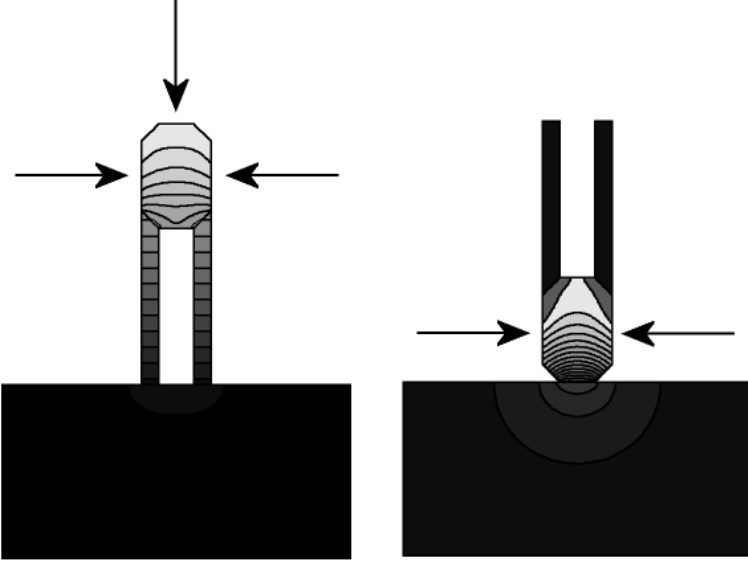


Figure 4.6: *FEM simulation: Penetration of heat at certain facets of the iron particle (due to the decomposition of acetylene) assuming a constant temperature at the silicon sample. Left: particle-on-top, right: particle-on-bottom setting. Arbitrary units for all dimensions (light: high temperature, dark: low temperature).*

In the regions of the nanotube and the silicon substrate in (4.12)  $\kappa^*$  is replaced by  $\kappa_{\text{nt}}^*$  and  $\kappa_{\text{Si}}^*$ . E.g.  $\kappa_{\text{nt}}^* = \frac{\kappa_{\text{nt}}}{\kappa_{\text{Fe}}} \cdot \kappa^*$ . Using:

$$\begin{aligned} \lambda_{\text{Fe}} &= 72.0 \frac{\text{W}}{\text{m}\cdot\text{K}}, c_{\text{q,Fe}} = 760.1 \frac{\text{J}}{\text{kg}\cdot\text{K}}, \rho_{\text{Fe}} = 7860.0, 0 \frac{\text{kg}}{\text{m}^3} \Rightarrow \kappa_{\text{Fe}} = 1.205 \cdot 10^{-5} \frac{\text{m}^2}{\text{s}} \\ \lambda_{\text{nt}} &= 150.0 \frac{\text{W}}{\text{m}\cdot\text{K}}, c_{\text{q,nt}} = 675.2 \frac{\text{J}}{\text{kg}\cdot\text{K}}, \rho_{\text{nt}} = 2510.0 \frac{\text{kg}}{\text{m}^3} \Rightarrow \kappa_{\text{nt}} = 8.851 \cdot 10^{-5} \frac{\text{m}^2}{\text{s}} \\ \lambda_{\text{Si}} &= 108.0 \frac{\text{W}}{\text{m}\cdot\text{K}}, c_{\text{q,Si}} = 924.4 \frac{\text{J}}{\text{kg}\cdot\text{K}}, \rho_{\text{Si}} = 2328.3 \frac{\text{kg}}{\text{m}^3} \Rightarrow \kappa_{\text{Si}} = 5.018 \cdot 10^{-5} \frac{\text{m}^2}{\text{s}} \end{aligned}$$

( $\lambda$  at 373 K [75],  $c_{\text{q}}$  at 923 K [70],  $\rho$  at 293 K [75])

For the heat conductivity of the nanotube the one for graphite in the direction parallel to the graphitic layers is taken and not the much higher one for perfect single-wall nanotubes ( $\lambda = 2980.0 \frac{\text{W}}{\text{m}\cdot\text{K}}$  [77]), as we consider multi-wall nanotube grown by CVD which might have much more imperfections. Otherwise the temperature rise would be smaller. For iron  $\lambda$  is taken at the same temperature as the value for silicon and graphite (373.2 K) although a value at 900 K was found (just for iron). This might keep better the ratio

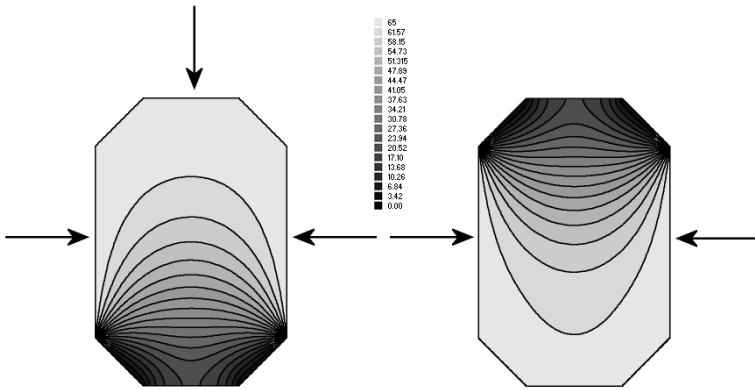


Figure 4.7: FEM simulation: Carbon diffusion through the particle. Left: particle-on-top, right: particle-on-bottom setting (light: high concentration, dark: low concentration).

between the components.

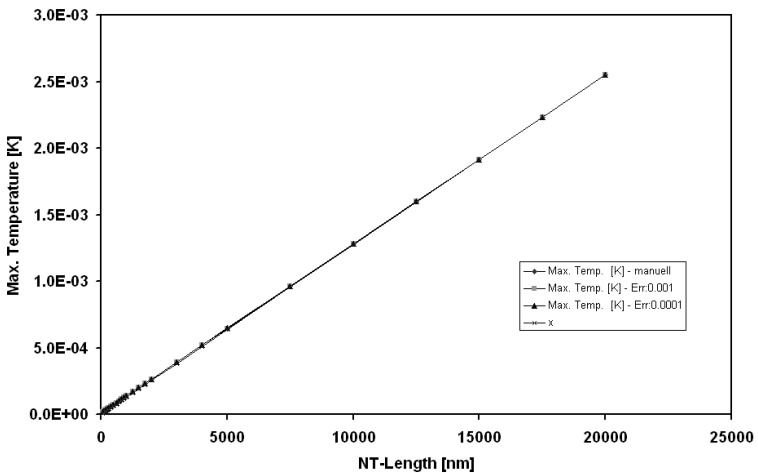


Figure 4.8: Dependence of the maximal temperature rise on the nanotube length using the particle-on-top setting. It fits well with a linear behavior.

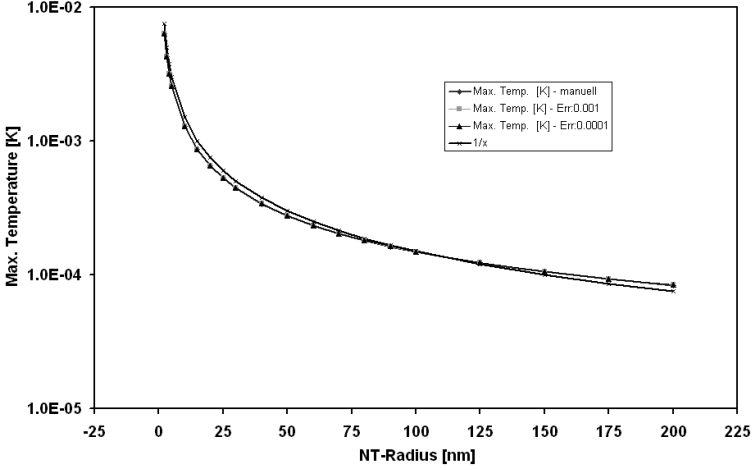


Figure 4.9: *Dependence of the maximal temperature rise on the particle radius using the particle-on-top setting. It fits well with a  $1/x$  behavior.*

The particle-on-top setting is highly parameter dependent. The dependence of the maximal temperature rise in the particle with the nanotube length can be fitted linearly  $T_{\max} \sim l_{\text{nt}}$  (Fig. 4.8) and with the nanotube radius with a  $1/x$  fitting  $T_{\max} \sim \frac{1}{r_{\text{nt}}}$  (Fig. 4.9). The last is mainly due to the fact that the correction factor  $T_o$  depends on the diffusion distance  $d_{\text{diff}}$  like  $1/x$ . A standard setting (NT-Length:  $5 \mu\text{m}$ , NT-Radius:  $10 \text{ nm}$ ,  $d_{\text{diff}} = 20 \text{ nm} \Rightarrow T_o(\text{bcc}) = 1.866 \cdot 10^{-7} \text{ K}$ ) reaches a temperature rise of  $\Delta T_{\text{top}} = 6.474 \cdot 10^{-4} \text{ K}$  with the particle on top (Fig. 4.6). For the standard tube already after  $1.65 \mu\text{s}$  90 % of the final temperature rise is reached (Fig. 4.10). Whereas the particle-on-bottom configuration is almost parameter independent. In this configuration the standard setting reaches a temperature rise of  $\Delta T_{\text{bottom}} = 1.165 \cdot 10^{-5} \text{ K}$ .

As the maximal temperature rise in the particle is very low the diffusion of carbon through the particle can be considered just as driven by the concentration gradient. It is assumed that the concentration of carbon is 65 ppm(weight) on the facets where the catalytic decomposition takes place and 0 ppm where the nanotube is constructed. Thus the diffusion through the particle is determined by Eq. (4.19). Fig. 4.7 shows the distribution of the carbon concentration in the catalyst particle in the stationary case (differential equation:  $-D\Delta T = 0$ ).



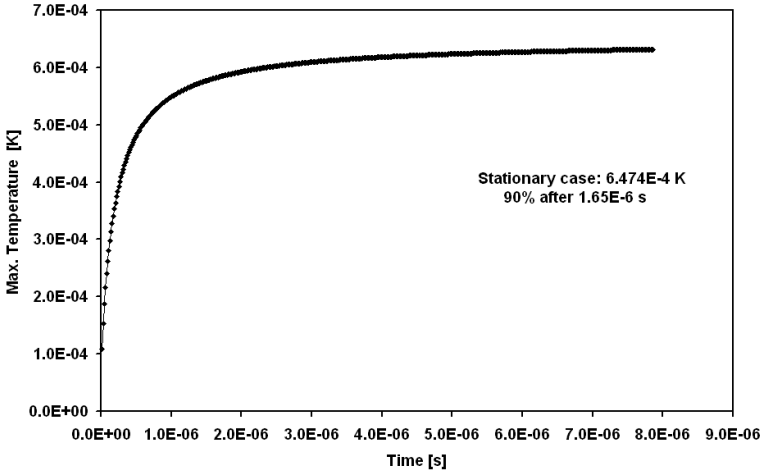


Figure 4.10: Heating of the particle with time (particle-on-top setting). 90% of the final temperature rise is reached already after  $1.65 \mu\text{s}$ .

### 4.3 Discussion

After supposing a new mechanism for the growth of carbon nanotubes it has been calculated with basic thermodynamic equations and simulated with an FEM software. For that purpose the catalyst particle was assumed to be symmetric, at least in growth direction. Thereby it turned out that the temperature rise is negligible. Thus thermal radiation is also negligible and the carbon diffusion through the particle is not thermally driven but determined by the concentration gradient.

At first glance there seems to be no reason why the nanotubes should grow in one particular direction. But the silicon surface breaks the symmetry. The diffusion and the catalytic decomposition is favored at the top facets and the catalyst particle is pushed up by the growing nanotube. Only if the particle is bonded too strongly to the silicon surface the nanotube grows in direction up while the particle rests on the surface.

Under the considered conditions a growth by surface diffusion is unlikely (relative high pressure, complete surface coverage) and it can not explain the growth of multi-wall nanotubes (growth of several walls with the same velocity, diffusion of carbon through the already created walls). Hung et al. [74] report a carbon diffusion into the bulk at temperatures  $T > 773 \text{ K}$  ( $500^\circ\text{C}$ ). This means that multi-wall carbon nanotubes can not be created below this temperature. The mobility of carbon in iron will increase with the temperature since the diffusion coefficient  $D$  is highly dependent on the temperature. This explains why the nanotube growth is a thermal process. A certain mobility of the

carbon atoms in the catalyst particle is essential for the growth. According to Hung et al. [74]  $C_2H_2$  decomposes catalytically to pure C at temperatures  $T > 400$  K ( $127^\circ C$ ). Thus there is a small window for the growth of pure nanotubes. The lower boundary is  $500^\circ C$  and the upper boundary is about  $750^\circ C$ . At still higher temperature polycrystalline carbon adsorbes on the nanotube surface as mentioned earlier (Chapter 3.3). In the frame of the experiments discussed here the lowest growth temperature was  $620^\circ C$ . For plasma-enhanced CVD lower deposition temperatures are reported: e.g. Choi et al. reported the experimental growth of nanotubes at  $550^\circ C$  [60].

The cessation of the catalytic growth may be caused by amorphous carbon on the catalyst particle. This can be generated catalytically or by condensation of in the atmosphere cracked carbon [26]. Acetylene can be cracked already at relative low temperatures due to the Boltzmann distribution of the thermal energy of the gas. There are always some gas molecules with enough energy for the cracking. Of course, the proportion increases with higher temperatures and thus finally there will be more amorphous carbon. Hung et al. [74] report a blocking of the reaction sites in case of carbon coverage. Additionally an oversupply of carbon (more then 65 ppm(weight) on the reaction surface) can cause the formation of iron carbide  $Fe_3C$ . The diffusion of carbon through  $Fe_3C$  is very low ( $D = 6 \cdot 10^{-16} m^2/s$  at  $650^\circ C$  [78]). If now  $Fe_3C$  is generated on the reaction surfaces, this could stop the growth of the nanotubes.  $H_2$  in the gas flow can etch the oversupply of amorphous carbon [79] and extend the growth time and thus the nanotube length. Indeed, this prolongation of the nanotubes was really observed (Chapter 3.3.7). But it turned out that the right amount of hydrogen is essential and hard to adjust. A reduction of pressure may help as well. But this would also slow down the creation of nanotubes.

The calculations allow to estimate the growth time, growth velocity and catalytic reactions. It is questionable if all the equations are exactly valid on the nanometer scale. But the calculated results correlate well with the experimental data. In Tab. 4.1 some experimental data of the nanotube growth are listed and compared with the calculated values. The calculated growth rate falls exactly in the range of the experimental data, and the calculated growth time is at the lower limit of the experimental data. It has to be considered that the calculated values are just for a standard tube with a diameter of 20 nm and a length of 5  $\mu m$ . And the diameter of the tubes in the experiments vary usually between 5 and 50 nm and the length between 2 and 10  $\mu m$ . According to the calculations the growth rate is not influenced by a varying length but just by the diameter of the nanotube like  $v_{\text{growth}} \propto 1/d_{\text{nt}}$ . But the growth time is influenced by both of them (Chapter 4.2.1). Baker et al. [72] found experimentally a dependence of  $v_{\text{growth}} \propto 1/\sqrt{d_{\text{nt}}}$  for carbon filaments. The difference between the  $1/\sqrt{d_{\text{nt}}}$  dependence for filaments and the calculated dependence  $1/d_{\text{nt}}$  for nanotubes for the growth velocity  $v_{\text{growth}}$  may lie in the fact that carbon nanotubes are hollow graphite-like structures and the carbon filaments consist of monolithic amorphous carbon, which may result in a slower growth.

The discussed activation time (time when the catalyst is already exposed to acetylene but the nanotube growth has not yet started) was observed as well. This period might be due to the reduction of  $Fe_2O_3$  to pure iron and a certain time of saturation of the catalyst grains with carbon.

In order to really compare the experimental data with the calculations the growth needs

to be observed directly in situ in a TEM/SEM to determine the growth time of one individual nanotubes and to determine at the same time the length of this tube and its diameter. For carbon filaments this has been performed already in 1972 by Baker et al. [72]. But detailed studies for carbon nanotubes are still missing because an in situ growth and the corresponding measurements on such a scale are difficult to perform.

It was also calculated and discussed that the growth rate is a function of the applied partial pressure and that effects should be visible below a pressure of about  $2 \cdot 10^{-2}$ . In [80] and [81] the influence of the partial pressure on the growth velocity is addressed, e.g. in [80] for pressures of  $10^{-4}$ ,  $10^{-3}$  and  $10^{-2}$  mbar growth rates of 1.5, 3.7 and  $4.7 \mu\text{m/s}$  are measured, respectively.

Even if the reported values apply not exactly, they give an impression and the equations means to calculate and estimate the nanotube generation process. A different geometry, than considered in the calculations and simulations, can also cause a difference in  $v_{\text{growth}}$ ,  $t_{\text{growth}}$ ,  $v_{\text{reaction}}$  and  $\tau_{\text{reaction}}$ .

Table 4.1: Comparison of the calculated values for growth time, growth rate and activation time with the experimental data.

Source	Growth time [s]	Growth rate [ $\mu\text{m/s}$ ]	Activation time [s]
Calculated	3.8	1.3	-
Chapter 3.3.3	< 60	> 0.16	$\sim 120$
Chapter 3.6	< 10	> 0.1	< 10
Ref. [80]	10	0.9 - 5.1	6 - 45
Ref. [81]	10 - 15	0.9 - 8.0	10 - 50

The difference between the calculated temperature rise  $\Delta T = 6834.17 \text{ K}$  if all the produced heat is stocked in the particle and the nanotube (Eq. 4.31) and the simulated  $\Delta T = 6.474 \cdot 10^{-4} \text{ K}$  is due to the thermal coupling to the substrate in the latter case and the high thermal conductivities of iron, graphite and silicon. The produced heat is distributed in the material very rapidly (diffusive flux through the iron particle, the nanotube, the silicon substrate and out of the considered volume). In the particle-on-bottom setting this flux is led away even more rapidly and the temperature rise smaller (diffusion direct into silicon substrate).

The calculations can easily be repeated with other material parameters (e.g. for  $\text{CH}_4$  as carbon source gas and nickel as catalyst particle).



# Chapter 5

## Field emission of carbon nanotube films

One of the most promising properties that can be exploited for applications is the very good field emission of the nanotubes [29]. The electronic properties, the very small curvature radius at the top and the enormous length-diameter ratio of the carbon nanotubes offers this possibility [7]. Thereby, in earlier investigations it turned out that the non-aligned arrangement of the carbon nanotubes is even more efficient in field emission than an aligned one [82]. The emission from aligned nanotube films is lower because of screening effects between densely packed neighboring tubes and the small height of the few protruding tubes. In contrast, the non-aligned films offer well separated nanotubes which do not show these effects [83]. In this chapter the field emission properties of the carbon structures discussed in Chapter 3 are measured. Also simulations have been performed to estimate the influence of the geometrical circumstances on the actually emerging electric field. Finally, a scanning probe microscope is introduced which exploits the field emission of carbon nanotubes.

### 5.1 Field emission of nanotube films obtained at different deposition temperatures

Since the usually good field emission properties of carbon nanotubes should be exploited the nanostructures discussed in Chapter 3.3.3 were examined in more detail. The field emission properties of carbon nanotube films can significantly differ from the ones of individual nanotubes due to geometrical effects. In Fig. 5.1 the results of the field emission measurements of those carbon films are presented. A decrease of the absolute current density at a given applied field with increasing deposition temperature was noted. The turn-on field  $E_{to}$  (field to obtain a current density of  $10^{-5}$  A/cm<sup>2</sup>, first illumination of a screen pixel) and the threshold field  $E_{thr}$  (field at a current density of  $10^{-2}$  A/cm<sup>2</sup>, saturation of a screen pixel) both increase with increasing deposition temperature (Tab. 5.1). For the carbon structures deposited at temperatures of 790°C and above the current density for the threshold field of  $10^{-2}$  A/cm<sup>2</sup> was not reached below the maximal applied

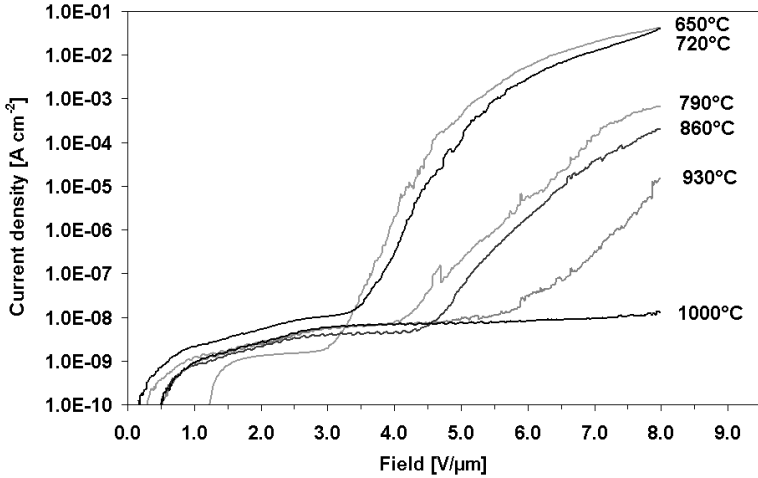


Figure 5.1: *Field emission I-V curves of the carbon nanotube films deposited at different temperatures: Nanotubes obtained at 650°C provide the best field emission field values.*

voltage of 1000 V at a 125  $\mu\text{m}$  interelectrode distance.

The field amplification factor was calculated with the Fowler-Nordheim equation. The model describes the electron emission from a flat surface by tunneling through the triangular surface potential barrier. The emitted current  $I$  is proportional to  $F^2 \exp(B\phi^{3/2}/F)$ , where  $F$  is the applied field just above the emitting surface,  $\phi$  is the work function and  $B$  is a constant ( $B = 6.83 \cdot 10^{-9} \text{ eV}^{3/2} \text{ m}^{-1}$ ) [84]. Generally,  $F$  is not known exactly and is therefore taken here as  $F = \gamma E = \gamma V/d$ , with the applied voltage  $V$ , the interelectrode distance  $d$ , the field amplification factor  $\gamma$  and the macroscopic applied field  $E = V/d$ . The work function was assumed to be equal to 5 eV, which is a reasonable assumption for carbon-based field emitters [85].

The field amplification values do not follow a simple trend with temperature, as can be extracted from Tab. 5.1. It is well-known that for a single tube, a larger diameter will lower the field amplification factor for a given length. The increase of the diameter found in Fig. 3.9 should thus result in a monotonically decreasing field amplification factor (see Chapter 5.3.1). Earlier experimental results suggest that this trend is masked (at least in part) by varying nanotube lengths and nanotube densities on the samples, which leads to more or less pronounced screening effects [83]. The comparison with the SEM images suggest that the field emission corresponds to the geometry of the structures and that the structures with a smaller diameter emit better. This behavior was also observed earlier for nitrogenated carbon structures [86].

Table 5.1: Table of the field emission values: The turn-on field  $E_{to}$  (field at a current density of  $10^{-5}$  A/cm<sup>2</sup>, first illumination of a screen pixel), the threshold field  $E_{thr}$  (field at a current density of  $10^{-2}$  A/cm<sup>2</sup>, saturation of a pixel) and the field amplification  $\gamma$  (obtained by calculations based on the Fowler-Nordheim theory) as function of the deposition temperature.

Temperature T [°C]	Turn-on field $E_{to}$ [V/ $\mu$ m]	Threshold field $E_{thr}$ [V/ $\mu$ m]	Field amplification $\gamma$
650	4.2	6.4	696
720	4.5	6.8	688
790	6.3	-	958
860	6.5	-	751
930	7.9	-	410
1000	-	-	-

## 5.2 Field emission of nanotubes on glass substrate

The field emission performance of carbon nanotube films on glass substrate which have been described in Chapter 3.5 was characterized. The films obtained on silicon typically reach turn-on current densities of  $10 \mu\text{A}\cdot\text{cm}^{-2}$  at  $4.2 \text{ V}/\mu\text{m}$  (see Table 5.1), as compared to  $5.1 \text{ V}/\mu\text{m}$  for the film shown in Fig. 3.17c. In fact, the obtained films on glass were systematically less efficient emitters than those deposited on silicon (Fig. 5.2). It is supposed that most of the observed shortcomings (difficulty of growing films with a density comparable with those obtained on silicon with the same catalyst, higher emission fields) are due to the nature of the conductive film. While it appears that the  $\text{SnO}_2:\text{F}$  prevents diffusion of the catalyst into the glass, its roughness decreases the effective area that is in contact with the stamp during printing, leading to a smaller amount of transferred catalyst as compared to a flat surface (Fig. 3.17c). This in turn results in a lower emitter density and the lower emitter density might give rise to a higher noise level. Changes in the emission characteristics of individual emitters, as they might be caused by adsorptions, annealing or straightening of the tube, are more pronounced. The use of Indium Tin Oxide (ITO) or of amorphous Silicon (a:Si) could probably lead to a significant enhancement of both growth and field emission properties.

## 5.3 Simulations for the field emission of carbon nanotubes

The field emission current is relatively well predictable using the formula of Fowler-Nordheim. But it contains the applied field just above the emitting surface  $F$  which is expressed by the macroscopic field  $E$  which is enhanced by a factor  $\gamma$ :  $F = \gamma E = \gamma V/d$ . For this field values there are just rough approximative formulas. E.g. a simple model

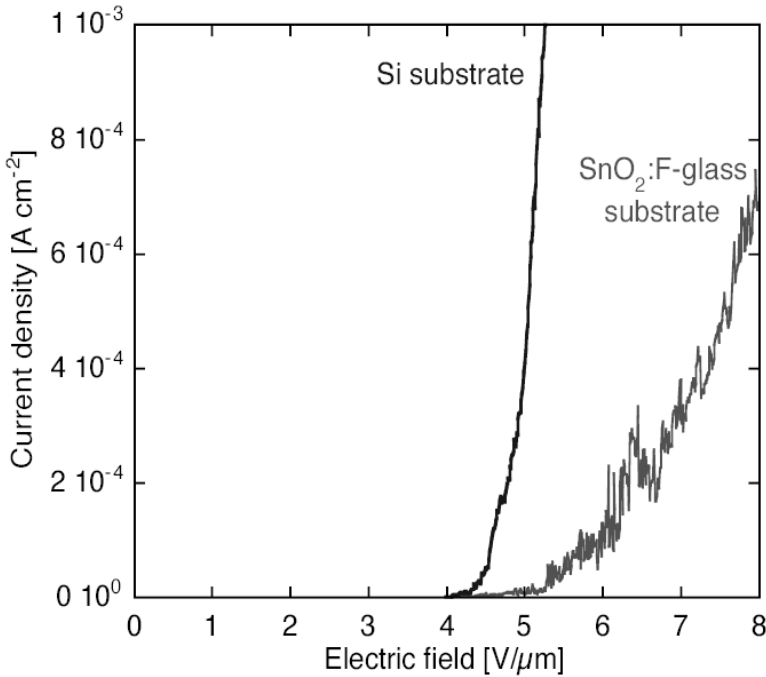


Figure 5.2: *Field emission I-V curves for patterned carbon nanotube films deposited on Si and SnO<sub>2</sub>:F-coated borosilicate glass.*

by Vibrans [87], a recent suggestion by Edgcombe and Valdre [88] which is based on vast simulations, and a model by Bonard et al. [89] which expands the model of Edgcombe and Valdre. In order to gain more insight into the field emission of carbon nanotubes simulations have been performed to evaluate the field enhancement. To this end the software EStat 4.0 by Field Precision [90] was used which is specialized in solving electrostatic problems in 2D and cylindrical configurations. The results of those simulations are then compared with the models mentioned above.

### 5.3.1 Effect of the geometry on the field emission

#### Tip configuration

In the frame of investigations on the field emission properties of individual nanotubes examined in an SEM [89] the influence of geometrical variations of the nanotubes tip



on the maximal emerging electric field was studied. One prominent example of those examined nanotubes has a length of  $1.4 \mu\text{m}$ , a diameter of  $15 \text{ nm}$  and a distance from the substrate to the counterelectrode of  $2.65 \mu\text{m}$ . Those values are estimations of the geometrical circumstances obtained by the SEM images. Fig. 5.3 shows this nanotube in an SEM and the field obtained by FEM simulations in the complete simulation volume and at the top of the nanotube tip represented by equipotential lines. The simulations were performed in cylinder-symmetrical geometry.

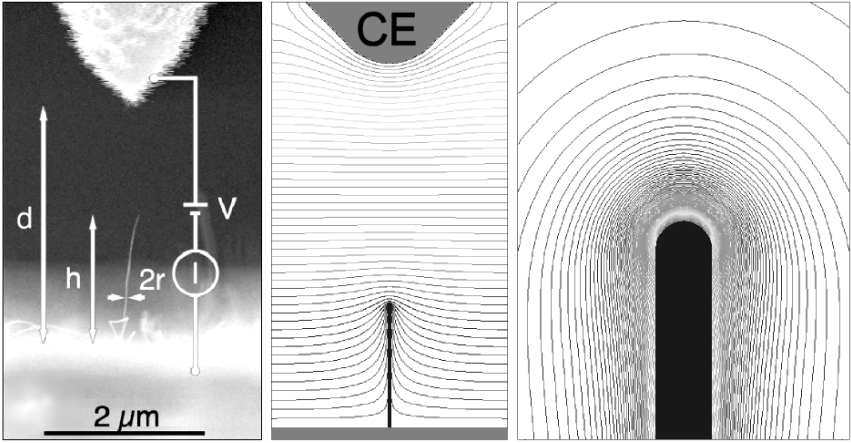


Figure 5.3: *Geometrical configuration in an SEM (left) and for the simulations of the field enhancement (middle/right). Left: SEM micrograph of an individual nanotube of length  $h = 1.4 \mu\text{m}$  and radius  $r = 7.5 \text{ nm}$  with the sharp anode positioned at a distance  $d = 2.65 \mu\text{m}$  [89]. Middle: Complete simulation volume. Right: Magnification of the tip area (region of interest).*

In Fig. 5.4a the electric field is shown for a nanotube terminated by a smooth hemisphere with the properties of the exemplary nanotube. With an applied voltage of  $10 \text{ V}$  a field of  $472 \text{ V}/\mu\text{m}$  is reached for such a tube, which corresponds to a field enhancement of  $\gamma = 125$ . For a cylinder of height  $h$  terminated by a half-sphere of radius  $r$ , Edgcombe and Valdre have shown from detailed simulations that  $\gamma = 1.2 \cdot (2.15 + \frac{h}{r})^{0.9}$  and that the usually used approximation  $\gamma \approx (2 + \frac{h}{r})$  overestimates the field enhancement by a factor  $0.7$  [88]. Bonard et al. [89] expanded the model of Edgcombe and Valdre to  $\gamma = 1.2 \cdot (2.15 + \frac{h}{r})^{0.9} \cdot [1 + 0.013(d/(d-h)) - 0.033((d-h)/d)]$ . This model considers additionally the distance between the substrate and the counterelectrode  $d$ . In the here considered case the formula of Edgcombe and Valdre results in  $\gamma = 134$ , the formula of Bonard  $\gamma = 141$  and the experiment published in [89] shows  $\gamma = 90$ .

Fig. 5.4b shows a nanotube with an adsorbate at the top of the tube. The adsorbate,

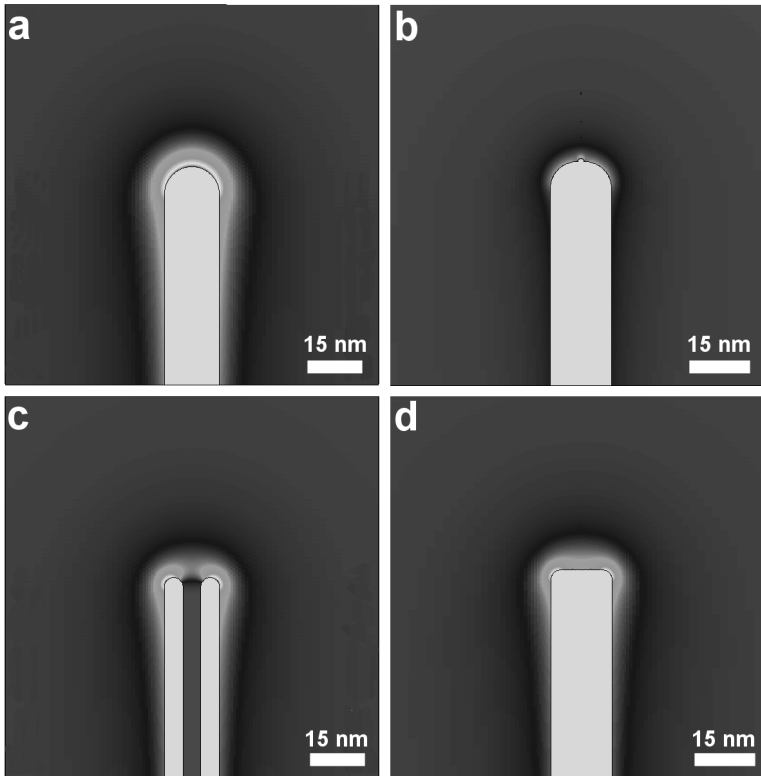


Figure 5.4: Geometrical variations of the nanotubes tip: (a) plain nanotube with a hemisphere as tip, (b) nanotube with adsorption, (c) open nanotube and (d) nanotube with a flat tip.

here represented by a hemisphere with a diameter of 10% of the tube diameter, results in a field of  $997 \text{ V}/\mu\text{m}$  which is an increase in electric field of 211% to the plain nanotube ( $\gamma = 264$ ). Other configurations are an open tube ( $E_{\text{max}} = 556 \text{ V}/\mu\text{m}$ ,  $\gamma = 147$ ) and a tube with a flat tip ( $E_{\text{max}} = 550 \text{ V}/\mu\text{m}$ ,  $\gamma = 145$ ). They both yield an increase in the electric field as well. It seems that a nanotube with a smooth hemisphere as shown in Fig. 5.4a is the configuration with the lowest field enhancement. Every change yields an increase of the electric field. I.e. least perturbations in the geometry of the tubes can cause large changes in field emission. This implies that the calculations and simulations treating ideal nanotubes often underestimated the field enhancement of real

configurations. Dean et al. performed extensive studies on the influence of adsorbates on the field emission properties of single-wall nanotubes [91]. They report a by far higher field emission current with adsorbates on the tubes which is in accordance with the here presented simulated results. But the field emission current with adsorbates exhibits also a higher noise level. The adsorbates can be removed by heating the nanotubes with an external source or by an intrinsic heating due to a high field emission current [92].

### Influence of emerging geometrical lengths

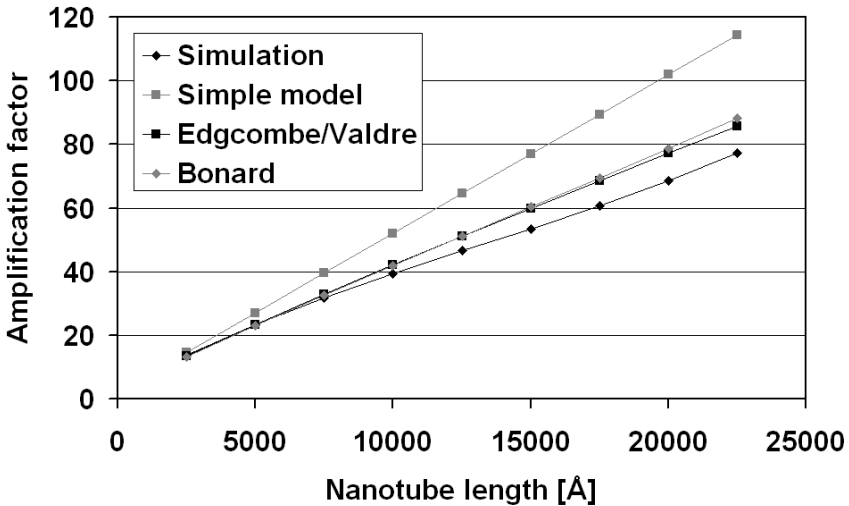


Figure 5.5: *Simulations on the field enhancement: Variation of the nanotube length with fix distance substrate - counterelectrode.*

In order to estimate the influence of different lengths emerging in the problem of a emitting nanotube against a counterelectrode, further FEM simulations have been performed. In Fig. 5.3 the configuration of the field emission set-up for the simulations with the distribution of the electric field is shown. A nanotube is mounted on a substrate (cathode) and a voltage is applied against a counterelectrode (anode). In the following the impact of the geometrical lengths is studied, such as the nanotube length with fixed distance substrate - counterelectrode  $d$  (Fig. 5.5), the nanotube length with fixed distance nanotube-tip - counterelectrode  $x$  (Fig. 5.6), the nanotube radius  $r$  (Fig. 5.7), the distance nanotube - counterelectrode (Fig. 5.8), and finally the aperture angle of the counterelectrode (Fig. 5.9).

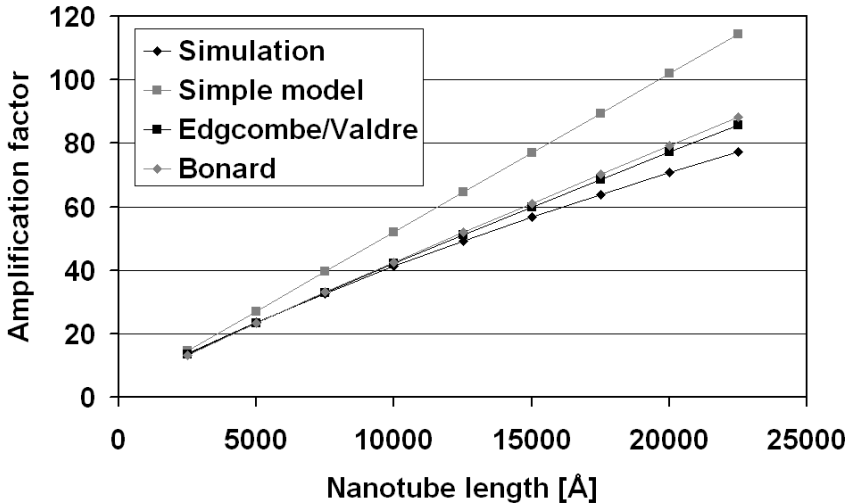


Figure 5.6: *Simulations on the field enhancement: Variation of the nanotube length with fix distance nanotube-tip - counterelectrode.*

In Fig. 5.5 the field amplification factor in such a configuration is shown as function of the nanotube length while the distance between substrate (S) and counterelectrode (CE) is kept constant. The electric field is increasing almost linearly. This in accordance with the simple approximative formula  $\gamma \approx (2+h/r)$  with the nanotube length  $h$  and the nanotube radius  $r$  [87]. The more sophisticated formulas of Edgcombe [88] and Bonard [89] reflect the simulated behavior even better.

The field enhancement with increasing nanotube length when the distance between nanotube-tip and counterelectrode is kept constant shows a similar behavior (Fig. 5.6). The increase is quite linear but for larger nanotube lengths it seems to flatten out a little bit. This behavior is reflected in the formula of Edgcombe and Valdre where  $\gamma \propto h^{0.9}$ .

If all parameters are kept fixed and just the radius of the tube is varied the field amplification factor is strongly decreasing with larger nanotube radii (Fig. 5.7). The formula  $\gamma = 1.2 \cdot (2.15 + \frac{h}{r})^{0.9}$  by Edgcombe and Valdre, as well as the one of Bonard et al. fit quite well to the simulated characteristic, whereas the simple model overestimates again the values of the field enhancement.

And finally, Fig. 5.8 shows that the amplification factor is decreasing with augmenting distances  $x$  between nanotube and counterelectrode. The simple formula and the model of Edgcombe/Valdre do not follow this behavior. Just the improved model by Bonard et al. follows the simulated values due to the second term  $\gamma \propto [1 + 0.013(d/(d-h)) - 0.033((d-h)/d)]$ .

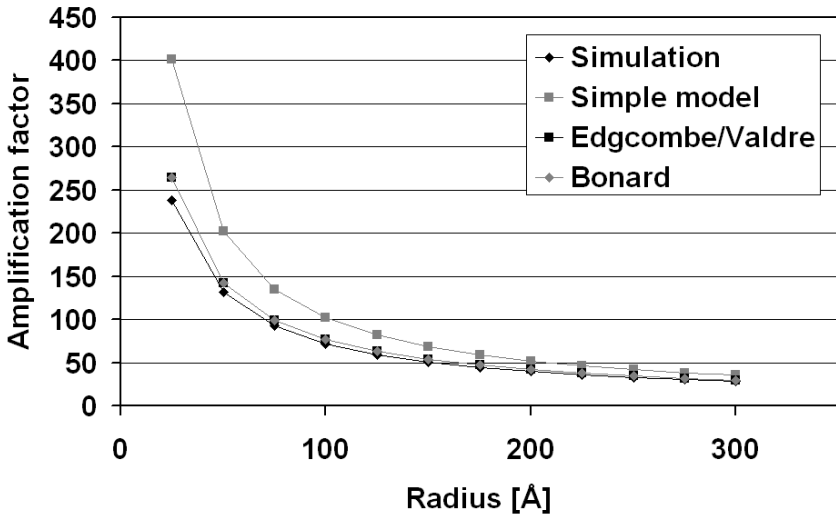


Figure 5.7: *Simulations on the field enhancement: Variation of the nanotube radius.*

The simulations and the corresponding model values show that there is still room for further improvement of the models.

### Influence of the geometry of the counterelectrode

In the following the influence of the shape of the counterelectrode is investigated. To this end a sphere-terminated cone was used as counterelectrode with an aperture angle reaching from a hemisphere with  $0^\circ$  to a flat counterelectrode with  $90^\circ$ . The maximal electric field is increasing with increasing aperture angle (Fig. 5.9). The total difference between a flat and a hemispheric counterelectrode is just in the range of some percent (here: 12%). Since the distance is kept constant this applies also for the field enhancement. The shape of the anode can be neglected in the field emission measurements since the simulations indicate that the shape of the anode does not have a significant influence on the obtained value of  $\gamma$ . The reason is that the radius of curvature of the nanotube is (in general) much smaller than that of the anode.

### 5.3.2 Heating of nanotubes during field emission

Individual nanotubes can carry currents of several microamperes [93]. At a certain level they start to fail due to an internal heating. In a system of emitting nanotube films mounted on a substrate the failure is not necessarily due to the heat generation in the

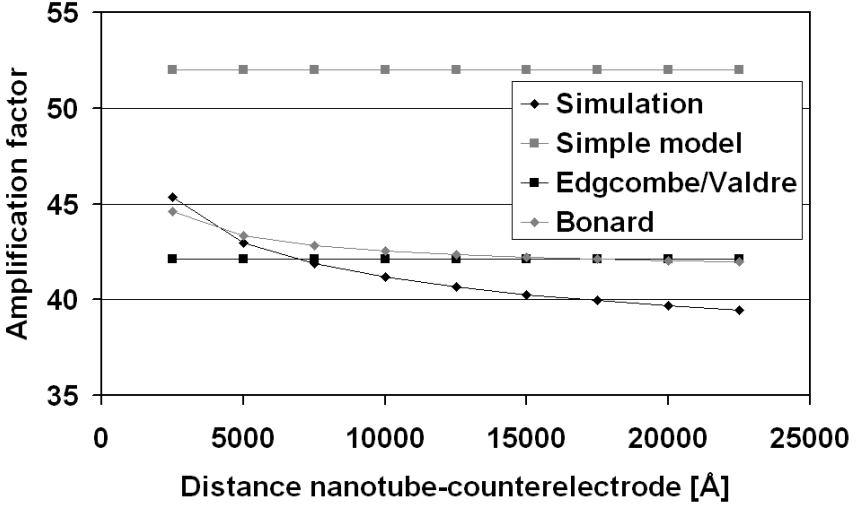


Figure 5.8: *Simulations on the field enhancement: Variation of the distance nanotube - counterelectrode.*

nanotube since they are very good thermal conductor. Another origins can be the heating in the contact to the substrate or the tip of the nanotube where the electrons are extracted. In order to estimate the heat generation in such a system during field emission numerical simulations have been performed using the same program like in Chapter 4.2.2: FreeFEM+ [69]. It solves partial differential equations (such as the heat diffusion equation) by the finite element method. Two heat sources are considered, namely the nanotube itself with a average resistivity of  $50 \text{ k}\Omega/\mu\text{m}$  [94], and the contact with a variable resistance dissipating heat in a volume equivalent to the size of the catalyst particle  $\frac{4}{3}\pi r^3$ , whereas  $r$  is the radius of the nanotube. Tabulated values were taken for the density and thermal conductivity of Si and Fe [75] and  $\lambda = 25 \text{ W}/(\text{m}\cdot\text{K})$  [95] for the nanotube. It was also assumed that the nanotube has an internal cavity of radius  $r/3$ .

The temperature can be estimated analytically when only the emitter dissipates power. Dolan et al. have shown for a cylindrical emitter that the temperature increases with increasing distance to the contact  $x$  and cylinder height  $h$  as  $h^2 - (x - h)^2$  [96]. The highest temperature is reached at the emitting end and amounts to

$$\Delta T_{\max} = \frac{\rho h^2 I^2}{2\pi^2 r^4 \lambda} = \frac{RhI^2}{2\pi r^2 \lambda} \quad (5.1)$$

where  $\Delta T_{\max} = T - T_0$ .  $T_0$  is the substrate temperature,  $\rho$  and  $\lambda$  are the electrical and thermal conductivities of the emitter, and  $I$  the current.  $R$  is the resistance  $R = \rho h/\pi r^2$ .

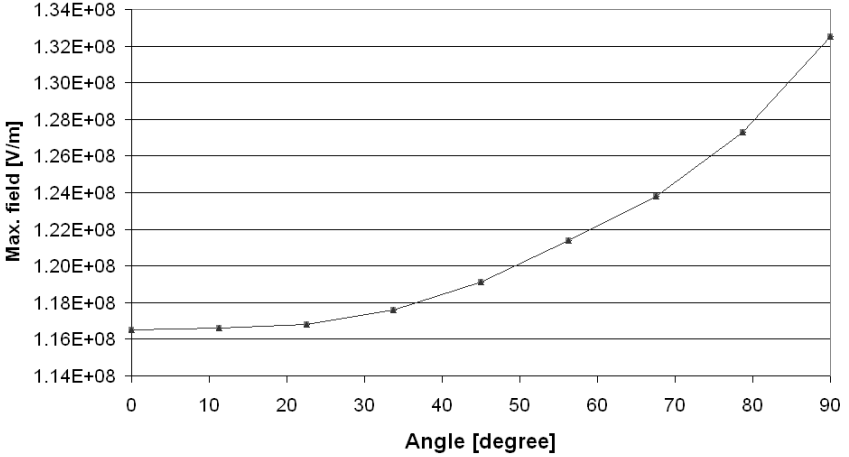


Figure 5.9: Variation of the aperture angle of the counterelectrode.

The main problem in estimating  $\Delta T_{\max}$  is to find reliable values for  $\lambda$  and  $R$  (or  $\rho$ ) and for their dependence in temperature.  $R$  has been lately measured for CVD-grown nanotubes and has been shown to vary from one tube to the next by as much as a factor 3 [97]. As for  $\lambda$ , values of 3000 W/(m·K) and 25 W/(m·K) [95] have been reported for a single arc-discharge multi-wall nanotube and for a CVD-grown nanotube film, respectively.

FreeFEM+ performs simulations in 2D, which means that it does not simulate a single nanotube on a surface, but a dense wall of nanotubes. In a first step, the consistency of the simulations was checked by neglecting the contact resistance. The profile of the temperature along the nanotube reproduces well the behavior of Eq. 5.1 as the temperature increases along the tube with  $h^2 - (x - h)^2$ , where  $x$  is the distance to the contact.  $\Delta T_{\max}$  is also proportional to  $R$  and to  $r^{-2}$ . The only difference due to the 2D character of the simulations as compared to the 3D situation considered here (and in Eq. 5.1) is that they give a dependence of  $\Delta T_{\max}$  that is proportional to  $h$  instead of  $h^2$ . This implies also that the absolute value of  $\Delta T_{\max}$  differs from the prediction of Eq. 5.1 by typically one order of magnitude. This fact is taken into account by calibrating in the following the values obtained by FreeFEM+ for a given nanotube length with Eq. 5.1.

In the frame of a study on the degradation and failure of carbon nanotube field emitters a nanotube has been studied exemplarily [93]. Fig. 5.10a gives the temperature profile along the nanotube ( $h = 2.35 \mu\text{m}$ ,  $r = 7 \text{ nm}$ ,  $I = 2 \mu\text{A}$ ) and the underlying substrate for different contact resistances. The lowermost profile corresponds to a negligible contact resistance as predicted by Eq. 5.1. This increase in temperature along the nanotube does not change as the contact resistance increases. For contact resistance  $\geq 500 \text{ k}\Omega$ , however,

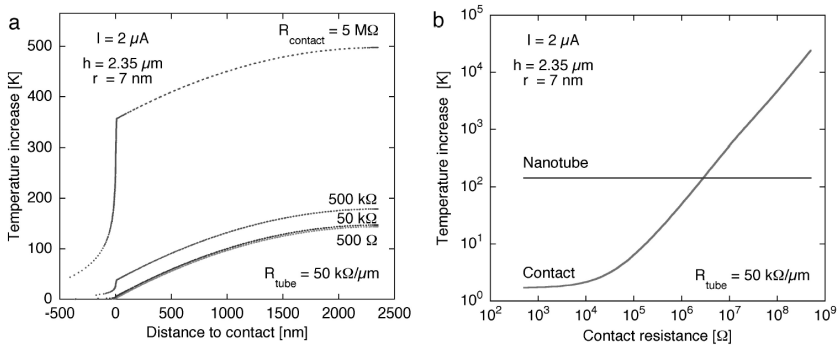


Figure 5.10: (a) Temperature profile along a nanotube of  $h = 2.35 \mu\text{m}$ ,  $r = 7 \text{ nm}$  with a resistivity of  $50 \text{ k}\Omega/\mu\text{m}$  at  $2 \mu\text{A}$  emitted current for varying values of the contact resistance. (b) Temperature increase at the contact and at the tip of the nanotube as a function of the contact resistance.

heating at the contact becomes significant and the absolute value of the temperature increases with the dissipated power. This fact is illustrated in Fig. 5.10b. While the relative increase at the nanotube apex is constant, the temperature rise at the contact increases linearly beyond  $R_c = 500 \text{ k}\Omega$ .

Fig. 5.10 underlines clearly that a Si substrate is not a perfect heat sink as is usually assumed (which will also be the case for glass). The temperature increase can easily reach values that lead to damages of the substrate, catalyst particle and/or nanotube: it amounts to  $1000 \text{ K}$  at  $100 \text{ M}\Omega$  for  $I = 2 \mu\text{A}$  and will increase with  $I^2$ .

### 5.3.3 Nanotubes as field emitter tips in a scanning probe microscope

The ongoing exploration of physical and chemical systems on a nanometer scale still requires new instruments to probe the properties in these regimes. A special kind of scanning probe microscope (SPM) allows the surface characterization by scanning field emission using a nanotube as emission source.

Carbon nanotubes can be grown by chemical vapor deposition (CVD) on a variety of surfaces including AFM and STM tips. Since nanotubes possess an extreme length-diameter ratio and a very small curvature radius at the tip they can act as efficient field emission sources by applying a voltage between nanotube and a counter electrode.

Scanning with such a nanotube tip over a surface in a certain distance range ( $5 - 200 \text{ nm}$ ) while locking on a certain field emission current with an appropriate feedback loop could be used to image the surface in a similar way like it is done in AFM/STM imaging. The



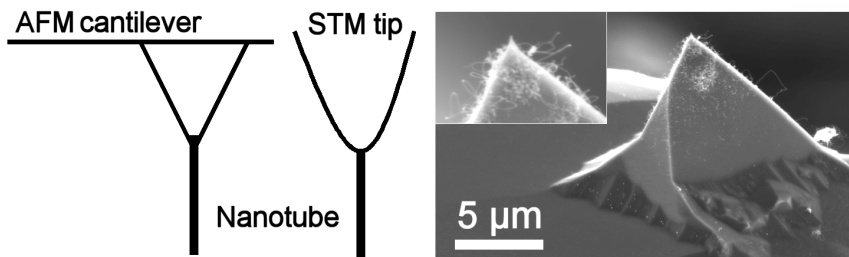


Figure 5.11: Possible configuration of mounted nanotubes on a tip and an SEM image of a first effort to mount nanotubes on an AFM tip (inset: magnification of the tip).

current can be chosen freely in wide range by scanning in a certain distance or applying an appropriate voltage. A field emission device whose dimensions are less than the elastic mean free path of electrons in air (of order 250 nm) and whose operating voltage is less than the first ionization potential of molecules present in air (15.6 and 12.7 eV for nitrogen and water, respectively) may even operate at atmospheric pressure [98,99]. Since the distance between nanotube tip and surface lies usually in the nanometer range the microscope should be able to work in air. For more safety against arc discharge or for longer distances a UHV chamber can be used, but operating in air would simplify the setup and the measurements.

Furthermore, the nanotube tip can be used in STM or AFM mode when mounted on a conducting AFM cantilever. Fig. 5.11 shows the two possibilities and a first attempt to mount nanotubes on a AFM tip. In this case by depositing cobalt as catalyst right on the top of the AFM tip by focused electron beam deposition [100] (performed by Ivo Utke of the Laboratoire d'optique appliquée at the EPFL) and subsequent CVD at 650°C as introduced in Chapter 3. The nanotubes which grow just on the AFM tip are clearly visible. But for an application in a SPM based on field emission they must be oriented in direction perpendicular to the scanned surface. This could be reached by polarizing the nanotubes in a strong electric field before the measurement. For a permanent orientation this polarization could be done by applying an electric field during the CVD process. An AFM with mounted nanotube tip could work in tunnel-mode, force-mode and field-emission-mode. Whereas an STM could just work in tunnel-mode and field-emission-mode. But with the STM the overall conductance would probably be better. The combination of the different modes would allow an extensive characterization of the samples. The field-emission-mode complements the present methods and would provide

- a probing of the geometry by locking on a certain emission current while adjusting the height over the sample,
- higher currents and voltages than in the tunnelling-mode, and thus excite more physical effects,

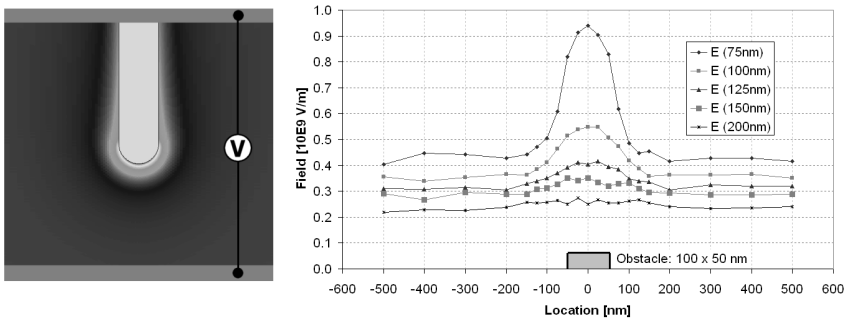


Figure 5.12: *Electric field of a nanotube scanning over a surface and simulated field emission properties of such a device with obstacle.*

- voltages widely independent of the nature of the substrate material (in contrast to STM),
- the possibility of low energy electron microscopy (no electron lenses are necessary, thus it would be more simple than SEM), and
- the possibility of cathodoluminescence (no lenses are necessary, as well).

The main advantage may be that by choosing the right potential difference the electrons which hit the surface can stimulate light emission of the substrate by exciting band-gap electrons in the sample surface (or other electronic effects). The corresponding current can be chosen by controlling the height of the nanotube over the surface. Thus the quantity of light emission can be determined and saturation effects could be studied. This *light emission stimulated by a field emitted electron beam from a scanning nanotubes* is the transition between conventional cathodoluminescence and STM light emission.

Another effect which can be used to image the surface is the emission of secondary electrons from the sample surface. The emission of those electrons is stimulated by the electrons emitted by the nanotube hitting the sample surface. The secondary electrons can be collected by a positively charged detector as it is the case in a scanning electron microscope (SEM). The advantage of the here described microscope over an SEM is that no electron lenses are necessary. The position information is gained by the scanning piezo mechanism.

A similar microscope was proposed by Young et al. in 1972 as "Topografiner" [101], a forerunner of the scanning tunneling microscope [102]. The advancement of the here presented microscope is mainly the use of carbon nanotubes as field emitters, which are very stable and provide a very small tip radius which leads to a relatively good lateral resolution. In field emission mode the resolution should be around the diameter of the used nanotube and in STM mode atomic resolution should be reachable. In Fig. 5.12 are

shown simulations of a nanotube scanning over a surface with obstacle. It is demonstrated that the resolution improves with smaller tip-surface distances. As already mentioned in the publication of Young et al. [101] the transition between tunneling and field emission mode takes place around a distance of 20 Å. Thus in field emission mode resolutions of some nanometers should be possible by using tip-sample distances of some nanometers.

## 5.4 Discussion

Field emitters have several advantages over thermoelectronic emitters. First, the emitter does not have to be heated, which eliminates the need for a heat source or a heating loop. The energy spread of the emitted electrons is also far smaller. Such emitters are easy to realize in microscopic dimensions and to incorporate in emitter arrays, and, finally, the emitted current can be controlled with the applied voltage. It is therefore not surprising that researchers are aiming at replacing thermoelectronic with field emitters in various applications. Displays (with one or several electron sources for each pixel) and microwave tubes are two examples. Nanotubes are good candidates for such device. Their physical properties allow the easy extraction of electrons. And their chemical properties makes them very stable which usually leads to long lifetimes.

Here various properties of multi-wall carbon nanotubes which are related to the field emission of nanotubes were analyzed. The results of the field emission experiments on the carbon structures described in Chapter 3.3 show that the thinnest nanotubes are more efficient field emitters. The field emission properties (emission fields, field amplification factor) follow loosely the morphology of the individual tubes, as the emission fields decrease with increasing temperature. It seems however that the overall structure of the nanotube film, such as nanotube density and height, plays a role that is more important than the diameter of the structures because of screening effects.

The crystallinity of the nanotubes may also influence the field emission properties. As the work function of polycrystalline and graphitic carbon are very similar, the main difference between the two forms is their electrical resistivity, which is lower in the case of well-graphitized carbon. A higher resistivity will lead to higher emission fields as a voltage drop will appear along the tube, reducing the effective applied field. However, this effect will play a role only at high current densities, and it will have little influence on the low current part of the I-V curve. Therefore significant differences in the turn-on field and field enhancement factor between well-graphitized and polycrystalline nanotubes of equivalent dimensions are not expected. The major factor that determines the field emission properties is the nanotube diameter, length and spacing.

In further experiments nanotubes were grown on glass substrates and it turned out that the problem with glass is that the catalyst diffuses into the material and thus is not anymore available to accomplish the growth of carbon nanotubes. The solution is to apply a diffusion barrier between the substrate and the catalyst material. In the here discussed case an ITO-like layer SnO<sub>2</sub>:F served the purpose. Additionally it provided the advantage to be conductive as well, which is useful in field emission devices. Those samples provided a less efficient field emission due to a smaller emitter density which is

caused by the very rough crystalline surface. This surface allows just inferior transfer of catalyst from the stamp to the sample surface by  $\mu$ CP. Nevertheless are the results promising and demonstrate that glass substrates can be used for field emission devices as flat panel displays.

The theoretical investigations on the field emission properties of individual carbon nanotubes support the experimental observations and help to interpret them. E.g. the study on the shape of the nanotube tip showed that small changes in shape can cause big variations in the field emission. Since nanotube tips are rarely perfect hemispheres but deformed in shape or covered with adsorbates the field emission of an individual tube might change a lot. Theoretical estimations are often not comparable with the experiments since they assume ideal nanotubes. One has to bear this in mind doing corresponding investigations. The study of the dependence of the maximal emerging electric field respectively the field enhancement factor on the different geometrical distances allows to evaluate the field emission properties of according devices and applications. The study shows further on that the shape of the counterelectrode has in general no significant influence on the field emission.

The degradation and the failure of carbon nanotube field emitters has been studied extensively by Bonard et al. directly in an SEM [93]. One reason for the failure is the heating of the tube during emission. With the simulations presented here it could be shown that nanotubes can easily heat up several 1000 K depending on the contact resistance between nanotube and substrate. This could lead to a degradation or evaporation of the tubes. During field emission the hottest spot is the tip of the tube but mechanical stress and local defects in the crystalline structure of the tubes can cause a failure at unpredictable sites.

The experience with the catalytic growth and the field emission of carbon nanotubes inspired the introduction of a new kind of scanning probe microscope based on the field emission of an individual nanotube mounted on an AFM or STM tip. This microscope would allow to scan the surface geometry and to excite at the same time electronic effects on the surface. The excitation energy can thereby be chosen in a wider range than this is possible with STM. Also imaginable is the generation of defects on the surface by electron bombardment. By this means one could structure e.g. surface resists like they are used in electron beam lithography.

## Chapter 6

# Conclusions and perspectives

Carbon nanostructures have been grown by thermal CVD with different catalysts which were delivered to a silicon substrate by microcontact printing. The experimental investigations presented allowed to get a comprehensive impression of the catalytic growth of carbon nanotubes. The development of the used catalyst ink was characterized as function of time and applied temperature. In the subsequent study on the morphology of the carbon structures grown by CVD a significant influence of the temperature and the catalyst material on the quality of the carbon nanostructures was observed. The diameter of the nanotubes and the density is adjustable by choosing the corresponding temperature and/or the concentration of the catalyst solution. Under the studied conditions iron is the best catalyst. A morphology transition with temperature from multi-wall nanotubes to "carbon worms" was observed. The thinnest and most crystalline nanotubes are obtained at temperatures between 650°C and 720°C. TEM imaging and Raman spectroscopy were used to investigate in more detail the character of these structures, and found that the increase in temperature above 800°C resulted in the formation of a polycrystalline outer shell over a nanotube core. Nanotubes obtained at temperatures below the melting temperature of borosilicate glass of 660°C are suitable as field emitters for flat panel displays. Using Ferritin as catalyst allowed to produce nanotubes which are very thin (5 nm) and monodisperse in diameter. With this experiment it could also be shown that the diameter of the nanotubes is strongly related to the diameter of the catalyst particles.

A mechanism for the growth of carbon nanotubes was suggested for nanotubes as they were obtained in the here presented experiments. Acetylene is dissociated catalytically on the small catalyst particles spread on the substrate surface. In a first stage the acetylene reduces the metal oxide grains to pure metal. The further catalytic dissociation of acetylene takes presumably place at facets of well-defined crystallographic orientation and the carbon diffuses into the particle. The resulting density gradient of carbon dissolved in the particle drives the diffusion of carbon through the particle. In order to avoid dangling bonds, the carbon atoms assemble at a less reactive facet of the particle, which leads to the formation of a nanotube. Thicker nanotubes at higher temperatures are generated due to the dissociation of acetylene in the gas phase, which leads to the formation of carbon flakes that condense at the catalytically grown structures. In order to support the growth model simple classic calculations and simulations were introduced to explain the

CVD nanotube growth. Thereby some formulas could be gained to estimate nanotube growth properties like the growth velocity which corresponds well to the experimental results. Furthermore a mechanism for the stop of the nanotube growth was proposed.

The field emission properties of the discussed carbon structures were measured. It turned out that (not surprisingly) the thinnest nanotubes emit the best. Furthermore, in regard to applications nanotubes have been grown on glass substrates and the field emission properties of such samples have been characterized. In order to gain more insight into the field emission of carbon nanotubes simulations have been performed to evaluate the maximal emerging field and the field enhancement. The results of those simulations have then been compared with commonly used models. This showed that there is still room for improvements for those models describing the field enhancement of such geometries. Finally, a new type of microscope is introduced which exploits the field emission of carbon nanotubes. It offers new possibilities to characterize samples on a nanometer scale.

The extraordinary properties of carbon nanotubes potentiate their application in commercial devices for the near future. The metallic and semiconducting nanotubes are shown to be capable to work as diodes, transistors and even logic inverters. And thus they can be implemented in integrated circuits. This was already done on an experimental scale by computer chip manufacturer like IBM and Infineon.

The very interesting field emission properties of carbon nanotubes led to first devices based on field emission. E.g. they act as electron source in x-ray analyzers, SEMs, lamps and flat panel displays.

Due to their very small tip radius they can be used as fine probes on AFM und STM tips and thus reach higher resolutions in the measured images.

They can be utilized also as electric sensors because their conductance depends on the electronic structure on their surface. Thus if, e.g., oxygen molecules bond to the nanotube surface the conductance changes and the change in current can be detected. This change is a function of the oxygen content in the environment.

Their mechanical stability and stiffness allows to use them in new carbon fibers. The French tennis-racket manufacturer Babolat already incorporates nanotubes into its "Nanotube VS" rackets [103]. But nanotubes could also be used to strengthen and lighten all kinds of materials, including synthetic bone implants and artificial joints.

The results presented in this thesis can serve as base for future research on the field of carbon nanotubes. E.g. one big challenge would be to follow the growth of carbon nanotubes in a TEM or SEM in order to determine the growth mechanism and the growth velocity experimentally. Another task would be to generate single-wall nanotubes by a similar method as used for the production of multi-wall nanotubes by ferritin (monodisperse iron clusters). The problem is to find 1 nm iron cluster (systems) which are stable in the CVD process and do not coalesce. This might be achieved by using suitable (bio-)molecules. Another challenge would be the realization of the SPM based on the field emission of a nanotube mounted on a STM/AFM tip which was introduced in this thesis. Also more detailed calculations of the thermodynamic of the catalytic growth and dynamic simulations of the complete growth would be expedient.

The results presented in this thesis can contribute to a more efficient application of carbon nanotubes in industrial devices as there are nano-probes for AFMs and STMs, field emitter

devices like nanotube lamps, flat panel displays, TEM electron sources or nanotubes as gas sensors. But they can also contribute to a better understanding of the catalytic growth of carbon nanotubes.





# Bibliography

- [1] H. W. Kroto, J. R. Heath, S. C. O'Brian, R. F. Curl, R. E. Smalley, *C-60 - Buckminsterfullerene*, Nature 381 (1985) 162.
- [2] S. Iijima, *Helical microtubules of graphitic carbon*, Nature 354 (1991) 56.
- [3] D. Ugarte, *Curling and closure of graphitic networks under electron-beam irradiation*, Nature 359 (1992) 707.
- [4] S. Iijima, M. Yudasaka, R. Yamada, S. Bandow, K. Suenaga, F. Kokai, K. Takahashi, *Nano-aggregates of single-walled graphitic carbon nano-horns*, Chem. Phys. Lett. 309 (1999) 165.
- [5] J. P. Salvetat, A. J. Kulik, J. M. Bonard, D. Briggs, T. Stöckli, K. Metenier, S. Bonnamy, F. Beguin, N. A. Burnham, L. Forro, *Elastic modulus of ordered and disordered multiwalled carbon nanotubes*, Adv. Mater. 11 (1999) 161.
- [6] T. W. Odom, J. L. Huang, P. Kim, C. M. Lieber, *Atomic structure and electronic properties of single-walled carbon nanotubes*, Nature 391 (1998) 62.
- [7] J. M. Bonard, J. P. Salvetat, T. Stöckli, L. Forro, A. Chatelain, *Field emission from carbon nanotubes: perspectives for applications and clues to the emission mechanism*, Appl. Phys. A 69 (1999) 245.
- [8] B. Vigolo, A. Penicaud, C. Coulon, C. Sauder, R. Paillet, C. Journet, P. Bernier, P. Poulin, *Macroscopic fibers and ribbons of oriented carbon nanotubes*, Science 290 (2000) 1331.
- [9] T. Guo, P. Nikolaev, A. G. Rinzler, D. Tomanek, D. T. Colbert, R. E. Smalley, *Self-assembly of tubular fullerenes*, J. Phys. Chem. 99 (1995) 10694.
- [10] V. Ivanov, A. Fonseca, J. B. Nagy, A. Lucas, P. Lambin, D. Bernaerts, X. B. Zhang, *Catalytic production and purification of nanotubules having fullerene-scale diameters*, Carbon 33 (1995) 1727.
- [11] M. S. Dresselhaus, P. Avouris, *Introduction to Carbon Material Research*, in: M. S. Dresselhaus et al. (Eds.), Carbon Nanotubes (Springer, 2001).
- [12] S. Iijima, T. Ichihashi, *Single-shell carbon nanotubes of 1-nm diameter*, Nature 363 (1993) 603.

- [13] D. S. Bethune, C. H. Kiang, M. S. de Vries, G. Gorman, R. Savoy, J. Vazquez, R. Beyers, *Cobalt-catalyzed growth of carbon nanotubes with single-atomic-layerwalls*, Nature 363 (1993) 605.
- [14] K. Tanaka, M. Okada, Y. Huang, *Electronic structure of single-walled carbon nanotubes*, in: K. Tanaka et al. (Eds.), *The Science and Technology of Carbon Nanotubes* (Elsevier, 1999).
- [15] P. Avouris, *Carbon nanotube electronics*, Chem. Phys. 281 (2002) 429.
- [16] W. B. Choi, D. S. Chung, J. H. Kang, H. Y. Kim, Y. W. Jin, I. T. Han, Y. H. Lee, J. E. Jung, N. S. Lee, G. S. Park, J. M. Kim, *Fully sealed, high-brightness carbon-nanotube field-emission display*, Appl. Phys. Lett. 75 (1999) 3129.
- [17] M. Croci, J. M. Bonard, O. Noury, T. Stöckli, A. Chatelain, *Cold Atmosphere CVD: A Simple Method for the Growth of Carbon Nanotubes*, Chem. Vap. Deposition 8 (2002) 89.
- [18] S. T. Tans, A. R. M. Verschueren, C. Dekker, *Room-temperature transistor based on a single carbon nanotube*, Nature 393 (1998) 49.
- [19] J. B. Cui, M. Burghard, K. Kern, *Room temperature single electron transistor by local chemical modification of carbon nanotubes*, Nano Lett. 2 (2002) 117.
- [20] O. K. Varghese, P. D. Kichambre, D. Gong, K. G. Ong, E. C. Dickey, C. A. Grimes, *Gas sensing characteristics of multi-wall carbon nanotubes*, Sensors and Actuators B 81 (2001) 32.
- [21] N. de Jonge, Y. Lamy, K. Schoots, T. H. Oesterkamp, *High brightness electron beam from a multi-walled carbon nanotube*, Nature 420 (2002) 393.
- [22] H. Sugie, M. Tanemura, V. Filip, K. Iwata, K. Takahashi, F. Okuyamab, *Carbon nanotubes as electron source in an x-ray tube*, Appl. Phys. Lett. 78 (2001) 2578.
- [23] G. Z. Yue, Q. Qiu, B. Gao, Y. Cheng, J. Zhang, H. Shimoda, S. Chang, J. P. Lu, O. Zhou, *Generation of continuous and pulsed diagnostic imaging x-ray radiation using a carbon-nanotube-based field-emission cathode*, Appl. Phys. Lett. 81 (2002) 355.
- [24] T. W. Ebbesen, P. M. Ajayan, *Large-scale synthesis of carbon nanotubes*, Nature 358 (1992) 220.
- [25] A. Thess, R. Lee, P. Nikolaev, H. Dai, P. Petit, J. Robert, C. Xu, Y. H. Lee, S. G. Kim, A. G. Rinzler, D. T. Colbert, G. E. Scuseria, D. Tomanek, J. E. Fischer, R. E. Smalley, *Crystalline ropes of metallic carbon nanotubes*, Science 273 (1996) 483.
- [26] C. Klinke, J. M. Bonard, K. Kern, *Comparative study of the catalytic growth of patterned carbon nanotube films*, Surf. Sci. 492 (2001) 195.

- [27] H. Kind, J. M. Bonard, C. Emmenegger, L. O. Nilsson, K. Hernadi, E. Maillard-Schaller, L. Schlapbach, L. Forro, K. Kern, *Patterned films of nanotubes using microcontact printing of catalysts*, Adv. Mater. 11 (1999) 1285.
- [28] H. Dai, J. Kong, C. Zhou, N. Franklin, T. Tombler, A. Cassell, S. Fan, M. Chapline, *Controlled chemical routes to nanotube architectures, physics, and devices*, J. Phys. Chem. 103 (1999) 11246.
- [29] J. M. Bonard, M. Croci, C. Klinke, R. Kurt, O. Noury, N. Weiss, *Carbon nanotube films as electron field emitters*, Carbon 40 (2002) 1715.
- [30] J. Li, A. M. Cassell, H. J. Dai, *Carbon nanotubes as AFM tips: Measuring DNA molecules at the liquid/solid interface*, Surf. Interface Anal. 28 (1999) 8.
- [31] Y. Xia, G. M. Whitesides, *Soft lithography*, Angew. Chem. Int. Ed. 37 (1998) 550.
- [32] A. Bernard, J. P. Renault, B. Michel, H. R. Bosshard, E. Delamar, *Microcontact printing of proteins*, Adv. Mater. 12 (2000) 1067.
- [33] N. L. Jeon, I. S. Choi, G. M. Whitesides, N. Y. Kim, P. E. Laibinis, Y. Harada, K. R. Finnie, G. S. Girolami, R. G. Nuzzo, *Patterned polymer growth on silicon surfaces using microcontact printing and surface-initiated polymerization*, Appl. Phys. Lett. 75 (1999) 4201.
- [34] P. C. Hidber, W. Helbig, E. Kim, G. M. Whitesides, *Microcontact printing of palladium colloids: Micron-scale patterning by electroless deposition of copper*, Langmuir 12 (1996) 1375.
- [35] R. H. Fowler, L. Nordheim, *Electron Emission in Intense Electric Fields*, Proc. R. Soc. London, Vol. A 119 (1928) 173.
- [36] T. T. Basiev, R. C. Powell, *Introduction (Special issue on solid state Raman lasers)*, Opt. Mater. 11 (1999) 301.
- [37] H. Haken, H. C. Wolf, *Molekülphysik und Quantenchemie* (Springer, 2nd Edition, 1994).
- [38] H. Hiura, T.W. Ebbesen, K. Tanigaki, H. Takahashi, *Raman studies of carbon nanotubes*, Chem. Phys. Lett. 202 (1993) 509.
- [39] D. A. Skoog, F. J. Holler, T. A. Nieman, *Principles of Instrumental Analysis* (Harcourt Brace College Publishers, 5nd Edition, 1998).
- [40] I. M. Watt, *The principles and practice of electron microscopy* (Cambridge University Press, 1nd Edition, 1985).
- [41] *Interactive Nano-Visualization in Science and Engineering Education (INVSEE)*: <http://invsee.asu.edu/Invsee/invsee.htm>

- [42] J. M. Bonard, T. Stöckli, O. Noury, A. Chatelain, *Field emission from cylindrical carbon nanotube cathodes: Possibilities for luminescent tubes*, Appl. Phys. Lett. 78 (2001) 2775.
- [43] H. Murakami, M. Hirakawa, C. Tanaka, H. Yamakawa, *Field emission from well-aligned, patterned, carbon nanotube emitters*, Appl. Phys. Lett. 76 (2000) 1778.
- [44] Z. Yao, H. W. C. Postma, L. Balents, C. Dekker, *Carbon nanotube intramolecular junctions*, Nature 402 (1999) 273.
- [45] M. Hirakawa, S. Sonoda, C. Tanaka, H. Murakami, H. Yamakawa, *Electron emission properties of carbon nanotubes*, Appl. Surf. Sci. 169 (2001) 662.
- [46] J. C. Charlier, S. Iijima, *Growth Mechanisms of Carbon Nanotubes*, in: M. S. Dresselhaus et al. (Eds.), Carbon Nanotubes (Springer, 2001).
- [47] A. Kumar, G. M. Whitesides, *Features of gold having micrometer to centimeter dimensions can be formed through a combination of stamping with an elastic stamp and an alkanethiol ink followed by chemical etching*, Appl. Phys. Lett. 63 (1993) 2002.
- [48] H. Kind, PhD thesis, EPFL No. 2123 (2000).
- [49] Telephone communication by Plano (29.11.2002, Wetzlar, Germany)
- [50] Ph. Mauron, Ch. Emmenegger, A. Züttel, Ch. Nützenadel, P. Sudan, L. Schlapbach, *Synthesis of oriented nanotube films by chemical vapor deposition*, Carbon 40 (2002) 1339.
- [51] W. Ostwald, *Über die vermeintliche Isometrie des roten und gelben Quecksilberoxids und die Oberflächenspannung fester Körper*, Z. Phys. Chem. 34 (1900) 495.
- [52] F. Tuinstra, J. L. Koenig, *Raman spectrum of graphite*, J. Chem. Phys. 53 (1970) 1126.
- [53] R. O. Dillon, J. A. Woollam, V. Katkanant, *Use of Raman-scattering to investigate disorder and crystallite formation in as-deposited and annealed carbon-films*, Phys. Rev. B 29 (1984) 3482.
- [54] D. S. Knight, W. B. White, *Characterization of diamond films by Raman spectroscopy*, J. Mater. Res. 4 (1989) 385.
- [55] D. Beeman, J. Silverman, R. Lynds, M. R. Anderson, *Modeling studies of amorphous-carbon*, Phys. Rev. B 30 (1984) 870.
- [56] R. Kurt, C. Klinke, J. M. Bonard, K. Kern, A. Karimi, *Tayloring the diameter of decorated C-N nanotubes by temperature variations using HF-CVD*, Carbon 39 (2001) 2163.

- [57] T. Doerk, J. Ehlbeck, P. Jauernik, J. Stancot, J. Uhlenbusch, T. Wottka, *Diagnostics of a microwave CO<sub>2</sub>-Laser discharge by means of narrow-band boxcars*, J. Phys. D 26 (1993) 1015.
- [58] K. Hernadi, A. Fonseca, J. B. Nagy, D. Bernaerts, J. Riga, A. Lucas, *Catalytic synthesis and purification of carbon nanotubes*, Syn. Metals 77 (1996) 31.
- [59] C. J. Lee, D. W. Kim, T. J. Lee, Y. C. Choi, Y. S. Park, Y. H. Lee, W. B. Choi, N. S. Lee, G. S. Park, J. M. Kim, *Synthesis of aligned carbon nanotubes using thermal chemical vapor deposition*, Chem. Phys. Lett. 312 (1999) 461.
- [60] Y. C. Choi, D. J. Bae, Y. H. Lee, B. S. Lee, I. T. Han, W. B. Choi, N. S. Lee, J. M. Kim, *Low temperature synthesis of carbon nanotubes by microwave plasma-enhanced chemical vapor deposition*, Syn. Metals 108 (2000) 159.
- [61] A. M. Cassell, S. Verma, L. Delzeit, M. Meyyappan, J. Han, *Combinatorial optimization of heterogeneous catalysts used in the growth of carbon nanotubes*, Langmuir 17 (2001) 260.
- [62] Z. F. Ren, Z. P. Huang, J. W. Xu, J. H. Wang, P. Bush, M. P. Siegal, P. N. Provencio, *Synthesis of large arrays of well-aligned carbon nanotubes on glass*, Science 282 (1998) 1105.
- [63] R. T. K. Baker, P. S. Harris, R. B. Thomas, R. J. Waite, *Formation of filamentous carbon from iron, cobalt, chromium catalyzed decomposition of acetylene*, J. Catal. 30 (1973) 86.
- [64] S. Mann, J. M. Williams, A. Treffry, P. M. Harrison, *Reconstituted and native iron-cores of bacterioferritin and ferritin*, J. Mol. Biol. 198 (1987) 405.
- [65] H. Kanzow, A. Schmalz, A. Ding, *Laser-assisted production of multi-walled carbon nanotubes from acetylene*, Chem. Phys. Lett. 295 (1998) 525.
- [66] M. Audier, A. Oberlin, M. Coulon, *Crystallographic orientations of catalytic particles in filamentous carbon*, J. Cryst. Gr. 55 (1981) 549.
- [67] S. J. Townsend, T. J. Lenosky, D. A. Muller, C. S. Nichols, V. Elser, *Negatively curved graphitic sheet model of amorphous-carbon*, Phys. Rev. Lett. 69 (1992) 921.
- [68] M. Nath, B. C. Satishkumar, A. Govindaraj, C. P. Vinod, C. N. R. Rao, *Production of bundles of aligned carbon and carbon-nitrogen nanotubes by the pyrolysis of precursors on silica-supported iron and cobalt catalysts*, Chem. Phys. Lett. 322 (2000) 333.
- [69] FreeFEM+ (v1.2.10): <http://www.freefem.org>
- [70] NIST WebBook (October 21, 2002): <http://webbook.nist.gov>
- [71] R. T. K. Baker, *Catalytic growth of carbon filaments*, Carbon 27 (1989) 315.

- [72] R. T. K. Baker, M. A. Barber, P. S. Harris, F. S. Fetes, R. J. Waite, *Nucleation and Growth of carbon deposits from the nickel catalyzed decomposition of acetylene*, J. Catal. 26 (1972) 51.
- [73] A. B. Anderson, S. P. Mehandru, *Acetylene adsorption to Fe(100), (110), and (111) surfaces: Structures and reactions*, Surf. Sci. 136 (1984), 398.
- [74] W. H. Hung, S. L. Bernasek, *Adsorption and decomposition of ethylene and acetylene in Fe(100)*, Surf. Sci. 339 (1995), 272.
- [75] CRC Handbook of Chemistry and Physics, 62th Edition (1981).
- [76] T. B. Massalski, Binary Alloy Phase Diagrams Vol. 1 (1986).
- [77] J. Che, T. Cagin, W. A. Goddard III, *Thermal conductivity of carbon nanotubes*, Nanotech. 11 (2000) 65.
- [78] B. Ozturk, V. L. Fearing, J. A. Ruth, G. Simkovich, *Self-Diffusion Coefficient of Carbon in Fe<sub>3</sub>C at 723K via the Kinetics of Formation of this Compound*, Met. Trans. A, 13A (1982) 1871.
- [79] H. W. Zhu, C. L. Xu, D. H. Wu, B. Q. Wei, R. Vajtai, P. M. Ajayan, *Direct Synthesis of Long Single-Walled Carbon Nanotube Strands*, Science 296 (2002) 884.
- [80] J. M. Bonard, M. Croci, F. Conus, T. Stöckli, A. Chatelain, *Watching carbon nanotubes grow*, Appl. Phys. Lett. 81 (2002) 2836.
- [81] J. M. Bonard, M. Croci, C. Klinke, F. Conus, I. Arfaoui, T. Stöckli, A. Chatelain, *Growth of carbon nanotubes characterized by field emission measurements during chemical vapor deposition*, Phys. Rev. B 67 (2003) 085412.
- [82] L. Nilsson, O. Gröning, C. Emmenegger, O. Küttel, E. Schaller, L. Schlapbach, H. Kind, J. M. Bonard, K. Kern, *Scanning field emission from patterned carbon nanotube films*, Appl. Phys. Lett. 76 (2000) 2071.
- [83] J. M. Bonard, N. Weiss, H. Kind, T. Stöckli, L. Forro, K. Kern, A. Chatelain, *Tuning the field emission properties of patterned carbon nanotube films*, Adv. Mater. 13 (2001) 184.
- [84] J. W. Gadzuk, E. W. Plummer, *Field-emission energy-distribution (FEED)*, Rev. Mod. Phys. 45 (1973) 487.
- [85] O. M. Küttel, O. Gröning, C. Emmenegger, L. Nilsson, E. Maillard, L. Diederich, L. Schlapbach, *Field emission from diamond, diamond-like and nanostructured carbon films*, Carbon 37 (1999) 745.
- [86] J. M. Bonard, R. Kurt, C. Klinke, *Influence of the deposition conditions on the field emission properties of patterned nitrogenated carbon nanotube films*, Chem. Phys. Lett. 343 (2001) 21.

- [87] G. E. Vibrans, *Vacuum voltage breakdown as thermal instability of emitting protrusion*, J. Appl. Phys. 35 (1964) 2855.
- [88] C. J. Edgcombe and U. Valdre, *Microscopy and computational modelling to elucidate the enhancement factor for field electron emitters*, J. Micr. 203 (2001) 188.
- [89] J. M. Bonard, K. A. Dean, B. F. Coll, C. Klinke, *Field emission of individual carbon nanotubes in the Scanning Electron Microscope*, Phys. Rev. Lett. 89 (2002) 197602.
- [90] EStat 4.0 by Field Precision: <http://www.fieldp.com/tricomp/estat.html>
- [91] K. A. Dean, P. von Allmen, B. R. Chalamala, *Three behavioral states observed in field emission from single-walled carbon nanotubes*, J. Vac. Sci. Technol. B 17 (1999) 1959.
- [92] K. A. Dean, B. R. Chalamala, *Current saturation mechanism in carbon nanotube field emitters*, Appl. Phys. Lett. 76 (2000) 375.
- [93] J. M. Bonard, C. Klinke, K. A. Dean, B. F. Coll, *Degradation and failure of carbon nanotube field emitters*, Phys. Rev. B 67 (2003) 115406.
- [94] B. Wei, R. Spolenak, P. Kohler-Redlich, M. Rühle, E. Arzt, *Electrical transport in pure and boron-doped carbon nanotubes*, Appl. Phys. Lett. 74 (1999) 3149.
- [95] W. Yi, L. Lu, D. L. Zhang, Z. W. Pan, S. S. Xie, *Linear specific heat of carbon nanotubes*, Phys. Rev. B 59 (1999) R9015.
- [96] W. W. Dolan, W. P. Dyke, J. K. Trolan, *The field emission initiated vacuum arc: The resistively heated emitter*, Phys. Rev. 91 (1953) 1054.
- [97] M. Ahlskog, presented at the NT02 conference, Boston College, Boston MA, July 6-11, 2002 (see also <http://www.nanoten.com/NT02/>).
- [98] A. A. G. Driskill-Smith, D. G. Hasko, H. Ahmed, *Fabrication and behavior of nanoscale field emission structures*, J. Vac. Sci. Technol. B 15 (1997) 2773.
- [99] T. K. S. Wongtt, S. G. Ingram, *Observational of Fowler-Nordheim tunnelling at atmospheric pressure using Au/Ti lateral tunnel diodes*, J. Phys. D. 26 (1993) 979.
- [100] I. Utke, B. Dwir, K. Leifer, F. Cicoira, P. Doppelt, P. Hoffmann, E. Kapon, *Electron beam induced deposition of metallic tips and wires for microelectronics applications*, Microelectronic Engineering 53 (2000) 261.
- [101] R. Young, J. Ward, F. Scire, *The Topografiner: An Instrument for Measuring Surface Microtopography*, Rev. Sci. Inst. 43 (1972) 999.
- [102] G. Binnig, H. Rohrer, Ch. Gerber und E. Weibel, *Surface Studies by Scanning Tunneling Microscopy*, Phys. Rev. Lett. 49 (1982) 57.
- [103] Tennis racket manufacturer BOBOLAT: <http://www.babolat.com>





# List of Publications

1. Jean-Marc Bonard, Christian Klinke, Kenneth A. Dean, Bernard F. Coll: *Degradation and failure of carbon nanotube field emitters*, Phys. Rev. B 67 (2003) 115406.
2. Jean-Marc Bonard, Mirco Croci, Christian Klinke, Fabien Conus, Imad Arfaoui, Thomas Stöckli, Andre Chatelain: *Growth of carbon nanotubes characterized by field emission measurements during chemical vapor deposition*, Phys. Rev. B 67 (2003) 085412.
3. Klara Hernadi, Edina Couteau, Polona Umek, Csilla Miko, Jin Won Seo, Laszlo Forro, Mirco Croci, Christian Klinke, Pauline Chauvin, Jean-Marc Bonard: *Controlled Growth and Applications of Carbon Nanotubes*, Chimia 56 (2002) 547.
4. Christian Klinke, Ralph Kurt, Jean-Marc Bonard, Klaus Kern: *Raman spectroscopy and field emission measurements on catalytically grown carbon nanotubes*, J. Phys. Chem. B 106 (2002) 11191.
5. Jean-Marc Bonard, Kenneth A. Dean, Bernard F. Coll, Christian Klinke: *Field emission of individual carbon nanotubes in the Scanning Electron Microscope*, Phys. Rev. Lett. 89 (2002) 197602.
6. Jean-Marc Bonard, Pauline Chauvin, Christian Klinke: *Monodisperse Multiwall Carbon Nanotubes Obtained with Ferritin as Catalyst*, Nano Lett. 2 (2002) 665.
7. Jean-Marc Bonard, Mirco Croci, Christian Klinke, Ralph Kurt, Olivier Noury, Nicolas Weiss: *Carbon nanotube films as electron field emitters*, Carbon 40 (2002) 1715.
8. Christian Klinke, Christian Waizenegger, Thomas Stöckli, Olivier Noury, Jean-Marc Bonard: *Patterned growth of carbon nanotubes on borosilicate glass*, AIP Conf. Proc. 591 (2001) 243.
9. Christian Obermair, Matthias Müller, Christian Klinke, Thomas Schimmel: *Local Electrical Deposition of Metal Islands Mechanically Induced with the Tip of an Atomic Force Microscope*, Chinese Phys. 10 (2001) S151.
10. Christian Klinke, Jean-Marc Bonard, Klaus Kern: *Comparative study of the catalytic growth of patterned carbon nanotube films*, Surf. Sci. 492 (2001) 195.

11. Jean-Marc Bonard, Ralph Kurt, Christian Klinke: *Influence of the deposition conditions on the field emission properties of patterned nitrogenated carbon nanotube films*, Chem. Phys. Lett. 343 (2001) 21.
12. Ralph Kurt, Christian Klinke, Jean-Marc Bonard, Klaus Kern, Ayatollah Karimi: *Tayloring the diameter of decorated C-N nanotubes by temperature variations using HF-CVD*, Carbon 39 (2001) 2163.

# Curriculum Vitae

Name:	Christian Klinke
Date of Birth:	May 20, 1971
Nationality	German
1977–1982	Primary school in Ettlingen, Germany
1982–1991	Secondary school in Ettlingen, Germany
1991	Abitur
1991–1992	Civilian service
1992–1998	Studies in physics at the University of Karlsruhe, Germany
1999	Diploma thesis at the Institute of Applied Physics of the University of Karlsruhe: "Rasterkraftmikroskopie an der Phasengrenze fest/flüssig"
2000–2003	Research and teaching assistant in the group of Prof. K. Kern at the Institute for Experimental Physics of the Swiss Federal Institute of Technology in Lausanne, Switzerland



# Acknowledgements

A thesis is not conceivable without the support of a lot of people. I would like to express to everyone who contributed to this thesis my sincere gratitude.

First of all I like to thank Prof. Klaus Kern. It was a pleasure to work in his group. His enthusiasm for new ideas, new collaborations, and also the work I did, always helped me with my thesis. He also helped me a lot with his precise, very competent and professional advices. I appreciated very much the freedom which I could enjoy during the three years of work in his group.

I am especially grateful to Jean-Marc Bonard who taught me a lot about physics and the business of a physicist. His well organized and efficient work impressed me very much. We had a very interesting and fruitful collaboration.

Furthermore I like to thank Hannes Kind for the introduction into the catalytic growth of carbon nanotubes.

Then I like to thank Johannes Barth for all his help and all the coffee at the "banana", Erik Delvigne for the fun we had from "Bleu Lezard" to "Jaggers" and when snowboarding, and Sylvain Clair for the nice time in the office and the fruitful discussions.

I appreciated very much the internship of Christian Waizenegger which led to nice results (Chapter 3.5) and I want to thank him especially for teaching me snowboarding.

Moreover, I enjoyed the cooperation with Pauline Chauvin who did a very nice diploma thesis which has been of great benefit (Chapter 3.6).

For his help in chemical questions and other discussions I like to thank Alexander Bittner and further thanks go to Ivo Utke, Ralph Kurt and Heiko Seehofer.

Last but not least I like to thank my family very much for all their support.

